Radar and LiDAR Fusion for Scaled Vehicle Sensing

Gregory Beale

Thesis submitted to the faculty of the Virginia Polytechnic Institute and State University in partial fulfillment of the requirements for the degree of

Master of Science

In

Engineering Mechanics

February 23, 2021

Blacksburg, Virginia

Keywords: Sensor fusion, Kalman filter, Extended Kalman filter, Object tracking, Radar, LiDAR

Radar and LiDAR Fusion for Scaled Vehicle Sensing

Gregory Beale

ABSTRACT

Scaled test-beds (STBs) are popular tools to develop and physically test algorithms for advanced driving systems, but often lack automotive-grade radars in their sensor suites. To overcome resolution issues when using a radar at small scale, a high-level sensor fusion approach between the radar and automotive-grade LiDAR was proposed. The sensor fusion approach was expected to leverage the higher spatial resolution of the LiDAR effectively. First, multi object radar tracking software (RTS) was developed to track a maneuvering full-scale vehicle using an extended Kalman filter (EKF) and the joint probabilistic data association (JPDA). Second, a 1/5th scaled vehicle performed the same vehicle maneuvers but scaled to approximately 1/5th the distance and speed. When taking the scaling factor into consideration, the RTS' positional error at small scale was, on average, over 5 times higher than in the full-scale trials. Third, LiDAR object sensor tracks were generated for the small-scale trials using a Velodyne PUCK LiDAR, a simplified point cloud clustering algorithm, and a second EKF implementation. Lastly, the radar sensor tracks and LiDAR sensor tracks served as inputs to a high-level track-to-track fuser for the small-scale trials. The fusion software used a third EKF implementation to track fused objects between both sensors and demonstrated a 30% increase in positional accuracy for a majority of the small-scale trials when compared to using just the radar or just the LiDAR to track the vehicle. The proposed track fuser could be used to increase the accuracy of RTS algorithms when operating in small scale and allow STBs to better incorporate automotive radars into their sensor suites.

Radar and LiDAR Fusion for Scaled Vehicle Sensing

Gregory Beale

GENERAL AUDIENCE ABSTRACT

Research and development platforms, often supported by robust prototypes, are essential for the development, testing, and validation of automated driving functions. Thousands of hours of safety and performance benchmarks must be met before any advanced driver assistance system (ADAS) is considered production-ready. However, full-scale testbeds are expensive to build, labor-intensive to design, and present inherent safety risks while testing. Scaled prototypes, developed to model system design and vehicle behavior in targeted driving scenarios, can minimize these risks and expenses. Scaled testbeds, more specifically, can improve the ease of safety testing future ADAS systems and help visualize test results and system limitations, better than software simulations, to audiences with varying technical backgrounds. However, these testbeds are not without limitation. Although small-scale vehicles may accommodate similar on-board systems to its full-scale counterparts, as the vehicle scales down the resolution from perception sensors decreases, especially from on board radars. With many automated driving functions relying on radar object detection, the scaled vehicle must host radar sensors that function appropriately at scale to support accurate vehicle and system behavior. However, traditional radar technology is known to have limitations when operating in small-scale environments. Sensor fusion, which is the process of merging data from multiple sensors, may offer a potential solution to this issue. Consequently, a sensor fusion approach is presented that augments the angular resolution of radar data in a scaled environment with a commercially available Light Detection and Ranging (LiDAR) system. With this approach, object tracking software designed to operate in full-scaled vehicles with radars can operate more accurately when used in a scaled environment. Using this improvement, small-scale system tests could confidently and quickly be used to identify safety concerns in ADAS functions, leading to a faster and safer product development cycle.

Dedicated to my father. Role model and engineer.

Acknowledgements

First and foremost, I would like to thank my advisors, Dr. Perez, Dr. Doerzaph, and Dr. Berkemeier. Their help has been instrumental over the last two and half years, and their expertise and guidance have not only helped shape this work, but also shape me as an engineer and person. I would also like to thank all of the colleagues at Continental Automotive and the Virginia Tech Transportation Institute that have aided me in this project. The experiences I've gained working at Continental, for VTTI, and on this study with the help of those mentioned have truly been invaluable.

Additionally, I want to thank my family and friends. Without their support I would not have been able to overcome the challenges of the last three years, of which there were many. From my friends I have learned so much about not only engineering, but also life as a whole during our time together. My parents have always been the foundation on which I stand. I owe them everything and their love and support has kept me centered when times were hard. To that I emphatically say, "Thank you."

Table of Contents

CHAPTER 1 – INTRODUCTION

This study aims to generate a fusion technique that uses radar and Light Detection and Ranging (LiDAR) sensor inputs to improve radar tracking performance in a small-scaled vehicle testbed. Scaled testbeds (STBs) derive value from accurately modeling full-scale system behavior within existing physical constraints while requiring minimal changes in control software functionality. Currently, vehicular STBs largely lack the ability to accommodate radars due to sensor scaling issues. In a small-scaled environment, the incoming radar data cannot provide the same spatial resolution that would normally be found in full-scale tests, resulting in less radar returns per object, more sensor noise, and, thus, poorer object tracking over time.

One solution to this issue is to modify the underlying tracking algorithm to perform optimally in the scaled environment. However, this would gravely decrease the value of the small-scale tests as the algorithm would significantly change between small-scale testing and the implementation of its full-scale counterpart. This manipulation would make test results difficult, if not impossible, to compare.

The proposed solution is to augment the traditional radar data returns in the small-scale environment with LiDAR. These sensors, while expensive and susceptible to noise in some environments, have much higher spatial resolutions than typical automotive radar sensors can achieve. Therefore, the LiDAR point cloud information could theoretically be used, through a sensor fusion approach, to augment depleted radar returns from an object in a small-scaled environment. A track-to-track fusion technique could be used between the two sensors to help the radar better estimate the position and trajectory of the object or vehicle being tracked within the small-scale environment.

In this investigation, software techniques from four fields of study were assessed to accomplish this goal: 1) Kalman filtering for automotive radars, 2) point cloud filtering with LiDARs, 3) sensor fusion techniques, and 4) small-scaled vehicle implementations. Each of these fields has been the subject of much recent attention as automated driving functions have holistically improved, but there is a large gap in the research when it comes to utilizing software solutions developed at full-scale to function with STBs. This study seeks to offer a potential solution to bridge that gap.

The initial step undertaken was to review previous work in these fields, documented in the form of a literature review. The review contains four main sections: Radar sensors and Kalman filtering; LiDAR point cloud filtering; sensor fusion; and scaled testbeds. The knowledge obtained from this systematic review was used to develop an efficient and effective fusion approach and to guide the acquisition of empirical data. In turn, the empirical data was used to 1) quantify the extent to which a reduction in environment scale reduced the accuracy and resolution in radar returns and 2) verify and quantify the extent to which the proposed fusion approach could generate trajectory data that properly simulated full-scale vehicle returns within the scaled environment.

Chapter 2 – Literature Review

2.1 Radar Sensors and Kalman Filtering

Radar detects objects within its field of view (FOV) by transmitting and receiving electromagnetic waves. A radar can report each object's position, radial velocity relative to the sensor, and an estimated radar-cross sectional (RCS) area. Engineers began working on automotive-grade radar in the 1970s due to its potential crash prevention applications. An early application of vehicle-mounted radars occurred on Greyhound buses in 1992, aimed at alerting bus drivers to impending forward collisions [1]. A subsequent application by Bosch, circa 1998, provided adaptive cruise control (ACC) functionality for Mercedes S-class sedans, and resulted in the first commercially available automotive radar system [1]. Since then, radars have increasingly become the pivotal sensor used to attain advanced driver assistance system (ADAS) functionalities. ADAS functions such as ACC, blind spot detection, forward collision warning, rear cross traffic alert, and advanced emergency truck braking systems heavily depend on radar sensors.

Automotive radars operate in two frequency bands, 24 GHz and 77 GHz, corresponding to 12 mm and 4 mm wavelengths, respectively, and are highly compact while being energy and computationally efficient. Each radar cycle results in a list of detection points that the radar can consolidate into data return values (i.e., radar "clusters"). In automotive radar, each cluster has four associated characteristics: lateral and longitudinal distance from the sensor (although radars do not inherently report clusters in the typical x-y coordinate scheme, but instead do so in the polar coordinate system – a non-linear coordinate transformation is required to convert to Cartesian coordinates), velocity radial to the sensor, and RCS. A typical radar cycle can detect anywhere between 10 and 75 clusters depending on the radar's software limits and the complexity of the environment [47]. Modern long-range radar sensors, such as a Continental ARS408, split their FOV into a long-range scan and a near-range scan to support multi-purpose use. Reported statistics of the typical ARS408 can be found in Table 1 [2]. Operating at approximately 14 Hz (72 ms period), the ARS408 radar can report clusters at varying radial velocity, angle, and distance resolutions depending on their location in the near and far scans. The full spec sheet can be found in Appendix D.

Table 1:ARS408 Long Range Radar Sensor data sheet excerpt

Measuring Performance	Comment	To natural targets (non-reflector targets
Distance range		0.20 ...250 m far range, 0.20...70m/100m@0…±45° near range and 0.20…20m@±60° near range
Resolution distance measuring	point targets, not tracking	Up to 1.79 m far range, 0.39 m near range
Accuracy distance measuring	point targets, not tracking	±0.40 m far range, ±0.10 m near range
Azimuth angle augmentation	(field of view FoV)	-9.0°...+9.0° far range, -60°...+60° near range

Elevation angle augmentation	(field of view FoV)	14° far range, 20° near range
Azimuth beam width (3 dB)		2.2° far range, 4.4°@0° / 6.2°@±45° / 17°@±60° near range
Resolution azimuth angle	point targets, not tracking	31.6° far range, 3.2°@0° / 4.5°@±45° / 12.3°@±60° near range
Accuracy azimuth angle	point targets, not tracking	±0.1° far range, ±0.3°@0°/ ±1°@±45°/ ±5°@±60°near range
Velocity range		-400 km/h...+200 km/h (- leaving objects...+approximation)
Velocity resolution	target separation ability	0.37 km/h far field, 0.43 km/h near range
Velocity accuracy	point targets	±0.1 km/h
Cycle time		app. 72 ms near and far measurement
Antenna channels /-principle	microstripe	4TX/2x6RX = 24 channels = 2TX/6RX far - 2TX/6RX near / Digital Beam Forming

Several key signal processing and electrical engineering tools and techniques are needed in modern radars [3]. For example, radar chirps, frequency modulated continuous-wave (FMCW) transmitters, fast Fourier transforms (FFTs), and specialized antenna arrays allow radars to continuously transmit (Tx) and receive (Rx) signals and then convert the returns into the aforementioned four dimensions reported for return signal clusters. In fact, the resolution of the velocity, range, and angle measures are limited by the FFTs performed in the sensor, which are inherently discrete in nature. Algorithms exist to provide additional resolution in those fields. These algorithms, however, tend to be complex and computationally expensive, so they are rarely used in commercial radars [3].

There is substantial literature dedicated to signal processing techniques and their implementation in radars. That literature is not considered herein, given that this investigation will use a commercially available radar that already incorporates industry-standard practices. Instead, the investigation aims to consider only the reported clusters from the commercially available sensor and attempt to minimize the diminished tracking abilities of the radar when it is operated at small-scale. For the interested reader, Patole, et al. (2017) provide an excellent overview of these techniques and describe a number of radar-applicable signal processing resources [3].

Radars excel at collecting real-time data from a dynamic environment but need filtering and estimation techniques to translate radar clusters into object tracks over time. This is generally true for any active perception sensor. Optimal state estimation, which tracking filters generally attempt, is a classic control theory problem with abundant literature. Early research in this field combined statistics to address one of the most important problems of the time: accurately estimating the state of a process in the presence of random noise – ever more important as electrical sensors became increasingly popular. This is the problem area where, in 1960, R. E. Kalman published his seminal work "A New Approach to Linear Filtering and Prediction Problems" and first introduced the famous Kalman filter (KF) [4].

Originally a project for the Department of Defense, Kalman was attempting to estimate the state of a linear time discrete system under both control and observation and developed a recursive software solution that “minimized the mean squared error of that process” [4]. In this case, “control” specifically refers to the ability to provide input commands to the system, while recording measurements from the system falls under “observation.” Many systems are both controlled and observed, although, in the case of radar object tracking, the system (i.e., other vehicle) will be under observation but not control. The basis for the filter is a linear predict-update model able to recursively include all past data in the state estimation without the need to continually store it. This greatly simplified the mathematics and computational requirements for filtering problems – something particularly relevant for processing occurring within embedded systems. The literature surrounding KF implementations is vast. The subsequent discussion is therefore focused on a high-level overview of the KF process and the variations of the KF that are common in automotive radars, such as the extended Kalman filter (EKF) and data association models.

In a KF, the noise in the system is often modeled as a Gaussian (normal) distribution with a mean value of zero and some variance value, σ^2. Due to this noise, the accuracy of the underlying system cannot be fully trusted, and the reported measurement is considered a combination of the true value skewed by some amount of unknown random noise. Therefore, the true state value is modeled as Gaussian distribution over the state space with inherent standard deviation [4]. By modeling the noise, the system estimate provided by a KF can, given the known added biases of the sensor(s), seek the true state value instead of erratically jumping in a non-smoothed or “unfiltered” way between the reported values.

At the heart of the KF’s predict and update model are Bayesian statistics, specifically Bayes theorem. Summarized in this context, the theorem concludes that given some knowledge about the current state of a system or process (expressed as a probability or underlying variance), it is more accurate to first, predict the state of the system in the future based off the current estimate and then, second, update that predicted state based on incoming noisy measurements; than it is to only update the state based on the measurements alone [5]. In this sense, all probabilistic information about a system can be helpful and should be included. No matter how uncertain one can be about a measurement’s true accuracy, the information it provides still contributes to improve the overall tracking accuracy [6].

Consequently, there are two major sets of linear control equations included in a KF. One pertains to the prediction update (*a priori* estimate) and the other to the measurement update (*a posteriori* estimate) [5].

The prediction step requires three basic elements: 1) the magnitude of the time step used to predict the future state, 2) the process noise expressed in variances and covariances (i.e. uncertainty values in the model predictions), and 3) the current covariances of the system. Only two calculations are needed. One calculation predicts the state at the future time step (Eqn. 1), and one updates the covariances of the system given the process noise (Eqn. 2).

Similarly, the measurement update requires three elements: 1) a matrix to map the measurement to the state space, 2) the sensor noise expressed in variances and covariances, and 3) the measurement values themselves. Three equations are then computed to complete this step of the KF. First, the Kalman gain is computed with knowledge of the sensor noise and the previously updated covariance matrix from the predict step (Eqn. 3). The Kalman gain is used as a weighting factor in whether to trust the *a priori* estimate of the current state more or less than the incoming measurement values and, thus, introduces

Kalman's novel approach to the filtering problem [4]. Second, the *a posteriori* state estimate is calculated using the Kalman gain factor along with the difference between the predicted and measured (from the sensors) states (Eqn. 4). Third, the covariance matrix of the system is updated to express the filter probabilistic certainties (Eqn. 5). The filter can then recursively proceed to the next time step.

Predict:

$$\boldsymbol{x}_k^- = \boldsymbol{F}\boldsymbol{x}_{k-1} + \boldsymbol{B}\boldsymbol{u}_{k-1} \tag{1}$$

$$\boldsymbol{P}_k^- = \boldsymbol{F}\boldsymbol{P}_{k-1}\boldsymbol{F}^{\boldsymbol{T}} + \boldsymbol{Q}_k \tag{2}$$

Update:

$$\boldsymbol{K}_k = \boldsymbol{P}_k^-\boldsymbol{H}^T(\boldsymbol{H}\boldsymbol{P}_k^-\boldsymbol{H}^T + \boldsymbol{R})^{-1} \tag{3}$$

$$\boldsymbol{x}_k = \boldsymbol{x}_k^- + \boldsymbol{K}_k(\boldsymbol{z}_k - \boldsymbol{H}\boldsymbol{x}_k^-) \tag{4}$$

$$\boldsymbol{P}_k = \boldsymbol{P}_k^-(\boldsymbol{I} - \boldsymbol{K}_k\boldsymbol{H}) \tag{5}$$

Equations 1 through 5 employ the naming convention in Challa, et al. (2011) [7]. Here, **x** is a column vector that denotes the system state estimates, **F** is the projection of the state into the next time step, the product **Bu** incorporates control commands (which is not applicable in the case under investigation, i.e., tracking an unknown moving target with a static radar), **P** is the covariance matrix of the system, **Q** is the process covariance matrix, **H** is the mapping function from measurement space to state space, **R** is the sensor covariance matrix, **K** is the Kalman gain, **z** is a matrix of measurement values, **I** is the $n \times n$ identity matrix (where *n* is the state space size – trackers that only estimate position with two-dimensional Cartesian coordinates, x and y, will have *n* equal to two, while those that estimate position and velocity with respect to x and y will have *n* equal to 4)., and the difference $\boldsymbol{z} - \boldsymbol{H}\boldsymbol{x}$ is commonly referred to as the residual or innovation. The subscripts $k - 1$ and k refer to the previous and current time step, respectively. In a similar fashion, the superscript "$-$" denotes that the value has been obtained during the *a priori* estimate. Kalman proved these equations result in minimizing the mean of the squared error in the state estimation [4, 5].

Kalman's original paper remains the ultimate guide for the KF and its proofs, but it already assumes that the reader is familiar with advanced statistics and control theory terminology. There are, however, many great introductory resources to the KF and optimal control theory. For example, Welch and Bishop (2006) provide a high-level overview of the KF, its probabilistic background, and a simple but "tangible" illustrative problem that requires only limited mathematical knowledge [5]. Labbe's "Kalman and Bayesian Filters in Python" is an excellent source for implementing a KF in machine-readable code [6]. Another highly relevant work in the field of controls is "*Applied Optimal Estimation*," written by

Gelb et al. (1974) [8]. A more modern book about controls and filtering is presented by Stengel in "*Optical Control and Estimation*" (1994) [9].

Since Stengel's book in 1994, and as interest in automated driving has grown, publications focused on the software implications of tracking and filtering techniques have become more prevalent. Bar-Shalom et al. (2001) published "*Estimation with Applications to Tracking and Navigation"* which provides an extensive overview on the theory and computational algorithms for estimation. Bar Shalom et al. (2001) particularly discusses the design and evaluation of state estimation algorithms that operate in a stochastic environment [10]. These algorithms form the backbone of information extraction systems for the remote sensing of moving objects, which are highly useful for automated driving. More recently, Challa et al. (2011) have discussed tracking solutions in their book "*Fundamentals of Object Tracking*" [7]. Challa et al. (2011) particularly provide an excellent source of knowledge on radar cluster tracking as many iterations of pseudo-code are provided. Due to their comprehensive discussion of approachable but thorough techniques for tracking and filtering, both works from Challa et al. (2011) and Bar-Shalom et al. (2001) are widely used by industry experts today.

Radar trackers used in industry rely heavily on the "base" KF. However, there are unique nuances in radar tracking, particularly in the automotive environment, that require additional elaboration on the KF method. Thus, there are two important additional facets of Kalman filtering for automotive radars: the extended Kalman filter (EKF) variation and the data association problem.

The extended Kalman filter variation arises from the origin of the KF – while Kalman originally designed the KF to track *linear* processes, purely linear applications are rarely observed in nature. Vehicles, airplanes, pedestrians, and other objects of interest can easily accelerate in two or three dimensions and linear models are often inadequate to effectively track their movement. This required a solution for non-linear tracking with the KF, which became the extended Kalman filter. Based on the popular technique to linearize any non-linearities in the model by using the first few terms in a Taylor Series expansion, the EKF uses partial derivatives of the process and measurement relationships with respect to the state vector to predict the system state [5]. Systems governed by non-linear equations are accompanied by continuously changing values for the sensor and process covariance matrices (**R** and **Q**, respectively), and the mapping matrix (**H**). To combat this, at each time step, the Jacobian of those matrices is computed and applied to the covariance matrices. Additionally, the nonlinear functions for the time projection (*f*) and mapping *(h)* can be defined for each time step to take into account any non-linear movement in the state or non-linear mappings of the state space to the measurement space. Welch and Bishop (2006) provide a good overview of this process and the variation of the five KF equations required, which are presented in Equations 6 to 10 [5, 11].

Predict:

$$(6) \qquad \boldsymbol{x}_k^- = \boldsymbol{f}(\boldsymbol{x}_{k-1}, \boldsymbol{u}_{k-1})$$

$$(7) \qquad \boldsymbol{P}_k^- = \boldsymbol{F}\boldsymbol{P}_{k-1}\boldsymbol{F}^{\boldsymbol{T}} + \boldsymbol{W}_k\boldsymbol{Q}_{k-1}\boldsymbol{W}_k^{\boldsymbol{T}}$$

Update:

$$(8) \qquad \boldsymbol{K}_k = \boldsymbol{P}_k^-\boldsymbol{H}_k^{\boldsymbol{T}}\left(\boldsymbol{H}_k\boldsymbol{P}_k^-\boldsymbol{H}_k^{\boldsymbol{T}} + \boldsymbol{V}_k\boldsymbol{R}_k\boldsymbol{V}_k^{\boldsymbol{T}}\right)^{-1}$$

$$(9) \qquad \boldsymbol{x}_k = \boldsymbol{x}_k^- + \boldsymbol{K}_k(\boldsymbol{z}_k - h(\boldsymbol{x}_k^-))$$

$$(10) \qquad \boldsymbol{P}_k = \boldsymbol{P}_k^-(\boldsymbol{I} - \boldsymbol{K}_k\boldsymbol{H}_k)$$

The terms of $\mathbf{W}_k$, $\mathbf{V}_k$, and $\mathbf{H}_k$ have been added to represent the Jacobian at time step *k* of the process covariance matrix, the sensor noise covariance matrix, and the mapping function, respectively. The most important step in the EKF process relies on linearizing the mapping function, **H**, as it relates non-linear system measurements to linear estimates, *h(),* that fit within the linear stochastic model of the KF. Each of the three measurement update equations (Eqns. 8, 9, 10) rely on the linearization of the mapping function [6]. Systems that attempt to model the changing velocity of tracked objects need to expand this step from the regular KF to the EKF. All books referenced earlier (i.e., Welch and Bishop, Gelb et al., Stengel, Bar-Shalom et al., and Challa et al.) dedicate extensive discussion to the EKF because of its wide range of applications and importance.

Although the EKF can be applied to many non-linear tracking problems, Bizup et al. (2003) have argued that complete linearization in the mapping function, **H**, results in an "over-extended" Kalman filter that may actually introduce errors over time [11]. Bizup et al. (2003) propose that, for tracking systems that measure range, angle, and – most importantly for radars – range rate, it is more accurate to "alternatively" linearize the mapping matrix so that the range rate is *only* related to the velocity estimates. Originally, the linearization of the mapping function results in position *and* velocity estimates that are functionally related to the range rate, causing unnecessary convolution. Bizup et al. (2003) simplify this linearization into the "aEKF" (alternative EKF) and show it results in quicker convergence for filters that incorporate range rate measurements. This approach has been adopted by some industry-developed automotive radar trackers.

The second required extension of the KF for automotive applications relates to the data association problem. Given that many perception sensors return multiple values per cycle (e.g., radar), these data returns need to be associated with objects in the environment before they can be passed into a Kalman filter. If there are multiple objects within the sensing area, the data from one object should not be conflated with the data return from another object, since this would clearly result in erroneous and unusable tracking solutions from the KF. In fact, out of all the factors influencing the KF, correct implementation of data association techniques can have the most influence on filter accuracy [7]. As a result, several different models have been developed to implement data association techniques.

The first step in successful data association is to create multi-track capability within the software program tracking the data measurements. In this manner, a set number of environmental objects can be observed and tracked over time, which is extremely imperative for automotive or robotic uses in uncontrolled environments. Multi-track KFs require the addition of an object list – each running their own KF – and some version of a data association technique to match the data returns to specific objects (or create new ones where necessary). A basic association technique is the nearest neighbor filter (NNF). In simplified tracking environments where an object only returns a single data return to the sensor, the NNF first filters all the data returns to a statistically relevant area around the tracked object (a process called gating) and then selects the closest measurement to the predicted state of the tracked object. All other data returns are considered extraneous and the result of sensor noise and unwanted clutter inherent in the environment [7]. Because the state covariance matrix includes standard deviation information, the point-by-point statistical comparison to find, first, the gating thresholds, and then, the closest data point is relatively straightforward, and the closest point can be easily selected. As described, the NNF limits its state update equations to a single data point, which, in actual tracking applications may not be as useful considering multiple data points can originate from the same object of interest. The simplified NNF therefore discards many of these useful data points.

The probabilistic data association filter (PDA) and its variations, on the other hand, use all the gated data returns to update the state prediction and are generally accepted as more accurate than the NNF in complex tracking environments. The PDA filter, however, requires two assumptions: 1) in the simplified tracking environment, the object of interest only results in one true data return to the sensor, and 2) the extraneous data returns are uniformly distributed in the perception space [7]. Following these assumptions for the PDA, the true measurement of the object lies somewhere within the gated threshold values but cannot be exactly determined by selecting only one of the gated measurements. Instead, the PDA filter proposes to use all gated measurements after they are statistically weighted, and their probabilities normalized [10]. In this manner, data points that more closely resemble the predicted state account for more in the measurement update step, but other returns within statistically relevant positions in the environment still influence the *a posteriori* state estimate.

One particular adaption of the PDA is the joint probabilistic data association (JPDA) filter. This extends the underlying principles of the PDA filters to work well when multiple tracks cross within close proximity – a scenario where the accuracy of the NNF and basic PDA filters often suffers due to their core assumptions, specifically the PDA assumption of uniform distribution of extraneous data returns outlined above. When track validation gates overlap, measurements from sensors can fall within both gates (Fig. 1). For example, it is not immediately clear which track the measurement M_3 belongs to. The NNF will choose the closest points to the center of the tracks, assuming all others to be possible new tracks; the PDA filters will weigh all measurements in the validation gate based on statistical proximity and expected noise densities in the viewing area. For PDA filters, this can cause errors in measurement probability weightings when those measurements actually originate from another track and are not sensor noise, and, possibly, the tracker could diverge [50]. Fortmann et al. (including Bar-Shalom) recognized this limitation of PDA filters and proposed their solution: the JPDA.

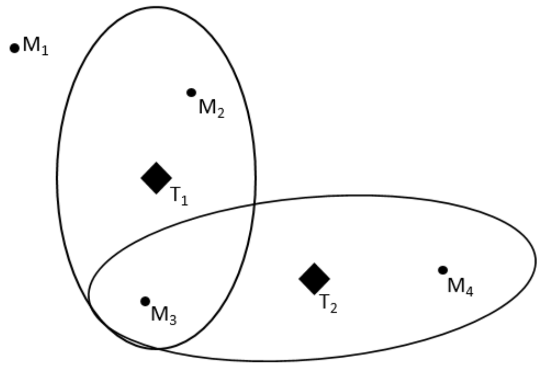

Figure 1: Typical data association problem with 2 tracks and 4 measurements and associated validation gates

To overcome this issue, Fortmann et al. (1983) modify the way probabilistic weightings were calculated using what they called “feasible joint events.” This time, the JPDA can probabilistically weigh the shared measurements of validation gates as possibly coming from both tracks and not as strictly noise like the PDA does. For every instance that track validation gates overlap, a cluster is extracted and a binary validation matrix is created (Fig. 2). This matrix outlines the measurement and track possible pairings: each row is a measurement, and each column is a track assignment with the first column representing clutter. Values of “1” signal a possible pairing and values of “0” indicate non-possible pairings based on the validation gates. Of course, measurements outside the gates are not included. From here, “feasible joint events” – possible measurement and track pairing combinations – are created and commonly labeled Ω_i [50]. Feasible events are created by looping through the validation matrix and selecting one measurement per row and one track per column. This ensures that the measurement could only come from one source, and each track is associated with only on measurement (the noise column can have any number of measurements because the JPDA needs to be able to model the situation where all measurements were the result of clutter) [50]. The validation matrix and collection of feasible events for the instance in Fig. 1 is shown in Fig. 2.

Feasible Events

	Noise	T = 1	T = 2
M = 2	1	1	0
M = 3	1	1	1
M = 4	1	0	1

Validation Matrices

$$\Omega = 1 \begin{bmatrix} 1 & 0 & 0 \\ 1 & 0 & 0 \\ 1 & 0 & 0 \end{bmatrix} \Omega = 2 \begin{bmatrix} 0 & 1 & 0 \\ 1 & 0 & 0 \\ 1 & 0 & 0 \end{bmatrix} \Omega = 3 \begin{bmatrix} 1 & 0 & 0 \\ 0 & 1 & 0 \\ 1 & 0 & 0 \end{bmatrix}$$

$$\Omega = 4 \begin{bmatrix} 1 & 0 & 0 \\ 0 & 0 & 1 \\ 1 & 0 & 0 \end{bmatrix} \Omega = 5 \begin{bmatrix} 0 & 1 & 0 \\ 0 & 0 & 1 \\ 1 & 0 & 0 \end{bmatrix} \Omega = 6 \begin{bmatrix} 1 & 0 & 0 \\ 1 & 0 & 0 \\ 0 & 0 & 1 \end{bmatrix}$$

$$\Omega = 7 \begin{bmatrix} 0 & 1 & 0 \\ 1 & 0 & 0 \\ 0 & 0 & 1 \end{bmatrix} \Omega = 8 \begin{bmatrix} 1 & 0 & 0 \\ 0 & 1 & 0 \\ 0 & 0 & 1 \end{bmatrix}$$

Figure 2: Validation and feasible event matrices for the configuration in Fig. 1 [51]

The feasible joint event matrices allow the JPDA to calculate the correct association probabilities denoted β_m^t , where *t* is the track number and *m* is the measurement number. Calculating β_m^t is analogous to calculating the probability that the measurement, *m*, belongs to the track, *t* [50]. Using the expected probability of detection for the track, whether the measurement was assigned to a track or clutter, the probability density for each measurement and track pair, and a normal distribution scaled by the innovation, probabilities for each element of the feasible event matrices are calculated. Then, the probabilities for each measurement and track pair in the validation matrix can be summed by the corresponding entries in Ω_i and normalized to arrive at β_m^t, the correct weighting factors for the JPDA [51]. The probabilities β_m^t influence the overall innovation matrix for the measurements in this timestamp and, in the immediate steps, the Kalman gain factor.

Fortmann et al. (1983) successfully demonstrated the JPDA's superiority over the regular PDA and the NNF when tracking crossing targets in the presence of clutter using their technique. However, the JPDA can suffer from long run times based on the sheer number of feasible event matrices needed and high volume of probability calculations for each of those matrices. The example in Fig. 1 only contained 3 measurement points and 2 overlapping tracks, but those instances where more tracks overlap or there are more measurements (possibly from multiple sensors) can result in millions of feasible event matrices [51]. Important contributions have been made to improve calculation times while maintaining accuracy. Fisher and Casasent (1989) propose using vector inner products and a modified analog validation matrix to reduce the number of calculations, although it requires a specialized optical processor [51]. Efficient depth-first searches have also been proposed to populate measurement and target pairs, thus speeding up probability coefficient calculations [52]. Quick approximation methods for the β_m^t values have also been shown to greatly improve calculation times when only 3 or less track validation gates overlap at any given time [52]. Musicki and Evans (2002) implement an integrated JPDA that focuses on track existence probabilities, paving the way for the trackers to tentatively create new tracks, confirm tentative tracks, and delete old tracks all based on track existence and the data associations made by the JPDA [53]. All modern JPDA trackers implement the original JPDA proposed by Fortmann et al. (1983) with some form of improvements in approximation made by the likes of [51, 52, 53]. The work in this project will draw heavily from implementations of both the NNF and JPDA.

In addition to [51, 52, 53], both Challa et al. (2011) and Bar-Shalom et al. (2001) describe the probabilistic mathematics that underlie such algorithms.

2.2 LiDAR and Point Cloud Filtering

LiDAR is a time of flight sensor technique that uses projected infrared lasers (~900 nm wavelength) to map the surrounding environment. Originally used for geographic mapping, the approach has been adapted to automotive use, particularly as autonomous driving systems have increased. Given that a single return pulse from one of these lasers can provide a distance value for one object, modern LiDAR systems typically incorporate multiple fast pulsing lasers in a mechanically spinning sensor to achieve a full 360° horizontal FOV. The different lasers, often called channels, are differentially angled to ensure complete coverage of a defined vertical FOV, often 30° or more. As the sensor spins, the lasers continually pulse at nearly 1000 Hz to collect data returns. With cycle times as high as 20 Hz, modern LiDAR systems can report hundreds of thousands and even millions of data points per second depending on how many channels they feature (the maximum number of channels available in a production LiDAR system is currently 128). Four characteristics can be derived from a single data return: distance values in the longitudinal (x), lateral (y), and vertical (z) directions, and an intensity value of the return. While both radars and LiDARs can detect obstacle position, LiDARs lack the ability to determine the range rate of an object in its FOV. However, a tradeoff between the volume of data and range rate reporting exists between the two sensors: although the radar can report radial velocity for each return, the LiDAR sensor is able to sense the world at a higher resolution.

In this investigation, a 16 channel Velodyne PUCK LiDAR will be used to support the sensor fusion task. This LiDAR unit, which is currently the more cost-effective sensor offered by Velodyne, features a 360° horizontal FOV, 16 laser channels, a range up 100 meters, +/- 3 cm accuracy, 30° vertical FOV, horizontal angle resolution of 0.1° – 0.4°, operating speed of 5 – 20 Hz, 905 nm operating wavelength, microsecond data timestamping, and a collection rate of up to 300,000 points per second [12]. The full data sheet for the PUCK LiDAR is available in Appendix E.

The most basic way to visualize LiDAR data points is in a point cloud. The x, y, and z components of each data return can be easily visualized at each frame, and the sheer volume of points reported by the sensor allows the presentation of an intuitive map of the surrounding area to the human viewer. A typical point cloud visualization is shown in Figure 3. The color of each dot is directly related to the intensity of the return – red denotes strong returns, while yellow and green points denote progressively weaker returns. Each point cloud often contains one complete rotation of the sensor and all the data points contained therein. Therefore, the sensor essentially builds a snapshot of the environment from the perspective of the sensor itself.

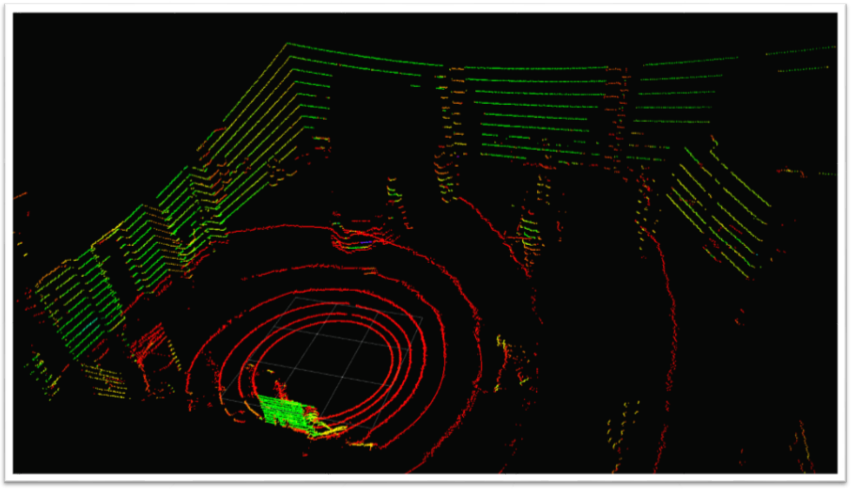

Figure 3: LiDAR point cloud

With hundreds of thousands of incoming points per second, efficient ways to store and process LiDAR data are essential. Many software solutions have been proposed for specialized projects, but currently one popular option is the open source point cloud library (pcl). Supported by corporations such as Google, Intel, Toyota, Velodyne, Nvidia, and Willow Garage; and many academic institutions, pcl is a cross-platform framework written and implemented in C++ that offers software solutions for the storage and processing of point cloud data from a variety of sensors, including camera and LiDAR [13]. The libraries in the framework incorporate many of the modern point cloud filtering and processing techniques that will be discussed later in this review and, with pcl's in depth tutorials, can be implemented into a wide range of solutions. Pcl attempts to provide a mainstream framework and code repository for industry partners and researchers alike, allowing for the easier implementation and understanding of developed point cloud filtering solutions. This aim makes it popular for use in robotic prototyping and autonomous driving systems, which has resulted in the development of a pcl plug-in for the prominent Robot Operating System (ROS) framework.

LiDARs are excellent at delivering high-spatial resolution data of the world that surrounds the sensor, but significant point cloud processing and filtering is needed to convert those data into useful information. A large body of research has been devoted to the development of these algorithms, particularly since the birth of autonomous driving systems in the early 2000s. For autonomous driving systems using LiDARs to work, embedded hardware and software – either in the LiDAR or in the vehicle – must be able to perform at least a subset of several critical tasks with the incoming point cloud data. These include estimating the drivable road area, identifying traffic objects (e.g., pedestrians, cyclists, other vehicles), classifying other environmental objects (e.g., buildings, fences, guardrails, lane lines, stop signs, trees), and performing object tracking. The correct classification of areas within the point cloud allows the vehicle to build a real-time map, localize, and path plan as the vehicle navigates the road. Therefore, the need for efficient data association techniques for automotive-grade LiDARs is evident.

Currently, no single algorithm can provide end-to-end filtering and classification capabilities in the automotive domain. Effective LiDAR systems incorporate multiple techniques to process a single point cloud. An overview of a typical automotive LiDAR system includes algorithms designed to:

1) Down-sample the original point cloud into clusters, voxels [48], occupancy grids, or octrees [16] to reduce computational processing time;
2) Estimate the drivable area using RANSAC (i.e., random sample and consensus [19]) or another ground plane estimator;
3) Convert clusters to objects and systematically assign data points to those objects, using a density or nearest neighbor approach;
4) Track objects over time using Kalman filter or other similar technique to identify dynamic and static obstacle tracks; and
5) Classify an object based on pre-specified parameters relative to the application and environment.

Research in this field was originally focused on the development of each of these individual steps, but more recent efforts have focused on the efficient implementations of these algorithms for the system as a whole to achieve near real-time sensing. Additional discussion on each of these steps is provided in subsequent subsections.

2.2.1 Down Sample Process

For a LiDAR system to achieve near real-time system requirements, the hundreds of thousands of points present in a point cloud need to be greatly reduced. One way to achieve this is to down-sample the relatively high-density data returns into fewer points through either clusters, voxels, octrees, and/or occupancy grid.

Clustering methods are ubiquitous and come in many different implementations, but in general they rely either on Euclidean or statistical distance to determine if one return is part of the same object or cluster as another return in the point cloud [14]. Many of the statistical techniques presented in Challa et al. (2011) and Bar-Shalom et al. (2001) are also useful for determining whether the data points in one area of the point cloud are dense enough to constitute a cluster. This process usually results in the grouping of 100 clusters or less per data frame. The centroids for those clusters can be stored and tracked more efficiently than thousands of individual data points. Often, a certain defined threshold is set or dynamically maintained to cap the number of clusters, gate the number of points per cluster, and constrain the spacing between adjacent clusters.

The ***voxel approach*** segments the three-dimensional space of the point cloud into small cubic elements. All points that lie within that volume of area are grouped and the average position or the point closest to the average position is often returned as the single data point for that voxel [15]. The data within the point cloud is then reduced to the number of voxels, which are often several orders of magnitude less than the original number of points.

The ***octree*** is an extension of the voxel approach. As the name suggests, octrees are hierarchical tree data structures where each node has eight leaves. The root of the tree stores the averaged data centroid for that voxel space, where each child level divides the space into eight octants and keeps track of any averaged centroids that were computed [16]. In this way each octree root node can average information from a high number of clustered points, depending on the size of the voxels. Each level of the octree increases the resolution – 64 smaller voxels can be stored with an octree height of 4, including the root node. More resolutions are available at the price of computational time. Fig. 4 shows a common octree visualization from free space to hierarchical data tree [54].

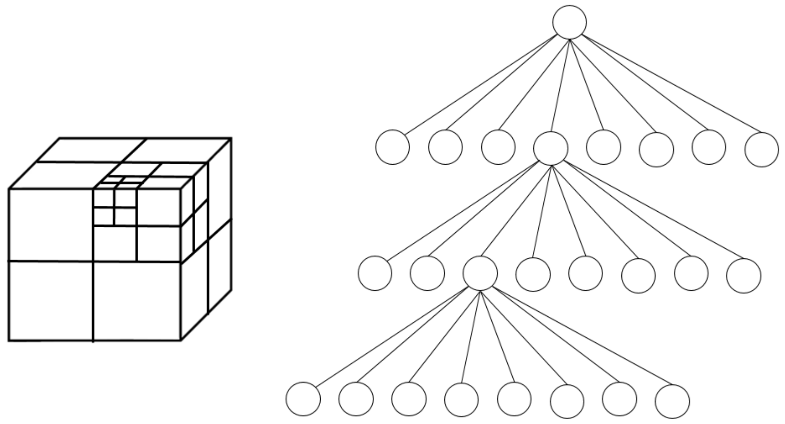
Figure 4: The breakdown of volumetric space into an octree [54]

Occupancy grids project the three-dimensional point cloud into a two-dimensional grid where points are commonly stored in lists based on their height (z-coordinate) in the point cloud space [17]. Clustering based on height or proximity can then be done for each grid block, reducing complexity. For algorithms that utilize occupancy grids, height maps are frequently involved. Clustering is often done after the down-sampling process is complete for computational efficiency.

2.2.2 Ground Plane Estimation

Because automotive LiDARs are deployed in areas where driving is possible, a large percentage of the data points within the point cloud originate from the road surface. Algorithms that can detect the road surface within point cloud data fall under the general category of plane estimators. The correct identification of this "ground" plane benefits the system in two major ways. First, the data points that constitute the ground plane can be removed from the point cloud once identified. There is no need to pass this data to any clustering methods since the road pavement itself is not, in most applications, considered an object that the system should avoid. The resultant reduction in data points increases computational efficiency. Second, the height of the ground plane can be used as a gate to identify other environmental objects. All road objects such as curbs, other vehicles, pedestrians, and cyclists should have data returns that originate with z-values and centroids that are located above the road. Similarly, suspended objects such as bridges, traffic lights, and overhanging signs should have heights substantially above the road surface level. A direct comparison between the height of the estimated ground plane and the height of a cluster can therefore be used to determine certain classification levels for an object [18].

There are many ground plane estimation techniques that range from simple (e.g., linear regression, height cut-offs) to highly complex (e.g., Markov models). The simplest method involves cutting off all points below a certain height value, usually informed by the placement of the sensor itself. For example, if the LiDAR sensor is mounted above the car at approximately seven feet off the pavement, it is sometimes a reasonable alternative to eliminate all data points in the cloud that are reported to be very close to seven feet below the sensor. This is not, however, a dynamic approach – and only works when the road plane is relatively flat. In real world applications, more robust estimators are needed to account for changing road plane angles.

An increasingly complex option is to perform a least squares regression on a relevant subset of data points to estimate the angle of the road. However, there will be an unknown quantity of data points that belong to the road in any given point cloud frame and a least squares regression may erroneously include data points from other nearby objects, skewing the plane estimate. The RANSAC approach offers a solution to this problem. Widely used and efficient, the RANSAC approach is to:

- Randomly sample the minimum number of points needed to estimate the model of interest. For example, to estimate a line, two points are needed; for a plane, three points are needed, and so on.
- Based on the resultant model estimate, determine the errors associated with fitting the current model to the rest of the data points
- Count how many of those data points lie within a given error threshold value
- Repeat the process *N* times for other randomly sampled starting points
- Choose the configuration with the best number of fitting data points [19]

Each random sample generates inliers and outliers for the model based on the error threshold value. The goal is to generate a model that identifies the noisy data as outliers and the "true" values as inliers, thus ignoring any skewed data returns in the parameter calculation. Fig. 5 shows the different solutions RANSAC and regression could produce, given the same data set [55]. Usually the RANSAC algorithm will terminate before performing *N* random samples if a certain proportion threshold of inliers is detected for the current model. RANSAC can also be used to detect multiple planes, a useful tool when a vehicle encounters a hill or speed bump where the road plane changes at a certain distance.

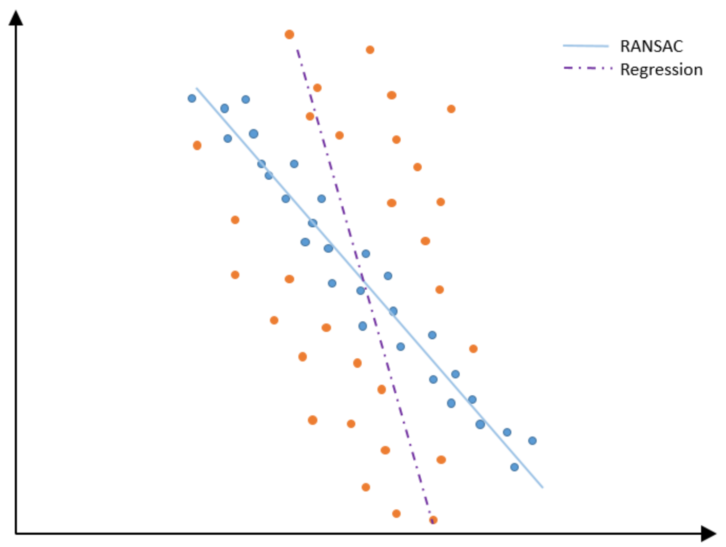

Figure 5: Line estimation with RANSAC showing inliers and outliers and possible regression line for the data set [55]

2.2.3 Converting Clusters to Objects

The identification and removal of the ground plane combined with the down-sampling of the point cloud into clusters allows the identification of static and dynamic road objects that will support obstacle detection and identification. While radars inherently sense radial velocity for each data return to aid in this process, LiDAR systems natively lack this data element. Typically, cluster movement over time is used instead to provide measurable velocity components of objects within a series of consecutive point clouds. Based on their position, clusters resulting from earlier processing steps, which are often reported as a centroid with associated density characteristics, are used to mark areas within the vehicle's local occupancy grid as occupied or empty. Once the next successive point cloud frame is available, the process is repeated to update the vehicle's surrounding occupancy grid. Over the course of several cloud frames and occupancy grid formulations, there can only be four progressions: 1) certain areas remain occupied, 2) remain unoccupied, 3) switch from unoccupied to occupied, or 4) switch from occupied to unoccupied. Discernible object tracks are then identifiable as additional frames are captured. For a stationary sensor, those areas that stay occupied can be considered static obstacles. Dynamic obstacles progress to adjacent occupancy grid locations over time in accordance with a certain path. To aid this, arbitrary object IDs and age since initial detection are often catalogued within occupancy grid tracks to help identify new objects as they come into observation (with relatively lower confidence of existence) and continue to follow older object tracks (observed over time with higher confidence of existence). An object's last observed age can also help determine when it is dropped from the tracking list, for example, if it leaves the observable area and remains untracked for a certain period of time.

2.2.4 Object Tracking

As previously noted within the discussion pertaining radar, object tracking using time discrete sensors is an optimal estimation and data association problem where object existence, object state, and sensor data are all commonly modeled as Gaussian distributions within the state space. Many of the same principles and solutions applicable to radars apply to LiDAR sensor systems as well. Like radar sensors, LiDAR sensor systems often incorporate KFs to accurately track objects within the sensing environment. The process and equations are the same, except that these KFs do not initially track velocity components of clusters as they first become visible. However, with the multi-frame fusion approach previously outlined, KFs can derive an object's velocity over time as they move within the structured occupancy grid.

As was the case for radar, data association techniques are required for multi-track functionality using LiDAR. The algorithms presented in Challa et al. (2011) and Bar-Shalom et al. (2001), such as the density and probabilistic filters, are also useful here, as well as others based on Euclidean distance and the global nearest neighbor (NN) procedure. Data association is usually performed after RANSAC processes, in either the clustering or occupancy grid formulation step. As new data points become available from the down-sampled point clouds, one option is to assign each formulated return to the NN using Euclidean distance for single object tracking, or global nearest neighbor (GNN) for multi-object tracking. Here, GNN uses statistical distance thresholds to assign incoming measurements to a list of *N* tracks using an "association cost" matrix. The cost matrix allows the association problem to be transformed into a linear assignment problem where the minimal cost solution can be solved for using known algorithms, such as the Hungarian method [20]. Other filters use Euclidean distances or density comparisons to determine whether data measurements should be associated with current object tracks or new ones created. The aforementioned JPDA technique or its modifications could also be applied in this context.

2.2.5 Object Classification

Given a myriad of different objects of interest within the driving area, it is useful to classify object tracks within the point cloud into a few general categories, including vehicle, pedestrian, cyclist, and environmental objects (e.g., trees, signs, buildings, fences, guardrails). Such object identification allows the use of more accurate object-specific models to predict its movement. For example, vehicles tend to stay in the usable road area and continue in their original directions, while cyclists and pedestrians can turn somewhat unexpectedly. There are a multitude of options employed for LiDAR object classification, including trained neural networks, support vector machines (SVM) classifiers, and box models. Current research is often focused on developing quicker and more accurate classifiers.

Each of the five processes described in the previous sections, in the context of a LiDAR-applicable object tracking system, has been subject to extensive research, particularly since the turn of the century when laser scanners were seen as promising technologies for ADAS and automated driving functionalities. For some processes, foundational research was conducted decades before it found use in LiDAR systems. The original paper outlining RANSAC was published in 1981 by Fischler and Bolles [19], while an early paper discussing the advantages of the nearest neighbor data association filter that GNN adapts was published in 1967 by Covert and Hart [20]. And, of course, the optimal tracking paper that is highly utilized in both LiDAR and radar object tracking was published by Kalman in 1960. Even the process of point cloud down-sampling is part of the wider field of data clustering. Within that field, Xu and Tian's (2015) *"A Comprehensive Survey of Clustering Algorithms"* is a useful summary of modern and traditional clustering algorithms [14]. In their discussion, it is obvious that many LiDAR clustering algorithms employed today are adapted from data structures and techniques originally developed from the graph theory, statistical, and digital electronics fields in the late 1980s and 1990s.

Early research in LiDAR object tracking considered two-dimensional laser scanners. For example, Mendes et al. (2004) utilized recursive line fitting to identify object clusters within a multi-target detection scheme [21]. Pattern recognition was then used to differentiate between pedestrians and other obstacles such as walls; all objects were tracked using a KF. This approach is only applicable to a single laser scan sensor, far from the three-dimensional LiDAR sensors currently available. As variations of tracking models continued to be researched for two-dimensional laser scanners, the next progression was to merge the measurements from multiple such scanners. Mertz et al. (2012) presented that type of sensor fusion approach applied to four laser scanners placed at varying angles around the vehicle [22]. Multiple laser scans allowed the system to detect objects at multiple heights, similar to a LiDAR with four channels. Each individual sensor contributed to a global point scan that is merged into a composite occupancy grid with associated height maps. Clusters were determined based on the distance between points. Mertz et al. (2012) also devised a custom ground plane removal scheme that involves calculating the average and standard deviation of each cell in the height map and then removing returns that are one standard deviation below the average height. KFs are used for object tracking.

With the implementation of multi-channel LiDARs in the early 2010s, more comprehensive and computationally efficient algorithms were needed. Azim and Aycard (2012) proposed a tracking algorithm for a 64-channel Velodyne LiDAR [23]. Here, the point cloud is down sampled into an octree that feeds into a three-dimensional occupancy grid. Clusters were determined by Euclidian distances in a region growing fashion – those data points close enough to an adjacent cluster were added to the original cluster; those that are farther away started a new cluster. Their novel approach involved tracking occupancy grid cells that change from occupied to unoccupied and vice versa over multiple scans to hypothesize where dynamic obstacles could be, a process akin to background subtraction from computer vision. Kalman filters and GNN were used to track and data associate, respectively. This method represented a major advance in modern filtering techniques but does run into extended computational times in highly cluttered urban areas. An alternative generative clustering approach was proposed by Kaestner et al. (2012) [24]. Instead of discriminating between a list of predetermined object classes, their approach detected a wide range of objects and grouped them together based on spatial proximity. Both dynamic and static obstacle detection and grouping were achieved for objects as small as a single pedestrian and as big as a tram without prior knowledge of object parameters. However, at the time this approach could only process a point cloud every two seconds which makes inapplicable for real time applications. Zhou et al. (2012), in turn, proposed an alternative object clustering technique they name "super segments" [25]. The authors first employed RANSAC to identify ground plane points and then grew clusters from all remaining points. If a point was within a certain distance threshold of an already determined cluster, it was added to that cluster. However, clusters were limited to a maximum number of points to ensure adequate sampling. RANSAC was run again on each cluster to obtain cluster plane normal vectors. All adjacent clusters with similar normal vectors were merged into super-segments. The authors claimed that these super segments better represent the planar surfaces in the driving area (e.g., houses, fences, guardrails) and other individual and smaller objects. General object classifications can be made based on the characteristics of these super segments. The proposed method is accurate but, at the time, took anywhere between 5-10 seconds to process a frame, limiting its applicability for a real-time system. A modified approach is presented in Asvadi et al. (2016), who proposed splitting the point cloud into multiple ground planes using RANSAC, each one further from the vehicle [26]. The remaining points that lay above these ground planes were considered possible road objects and down sampled into voxels. The novel aspect was that the incoming point cloud is merged with the five previous frames based on vehicle odometry measurements, allowing the detection of static and dynamic voxel grid cells. However, due to the large computational times to merge point clouds, the approach requires between 3 and 4 seconds to process a single frame.

In general, while all of these implementations represent accurate and reliable solutions to LiDAR point cloud filtering and object tracking, they did not meet real-time system needs given the available processing power in a typical LiDAR unit. Real-time tracking performance for automotive applications was not achieved until the second half of the 2010 decade. As computing platform capabilities and data transfer rates increased, researchers were able to implement and improve filtering algorithms for point clouds. Most works that achieve real-time capability recognize the need to pre-process point clouds into more effective data structures, although the overall approach generally remains consistent with earlier investigations.

One real-time solution is proposed by Wang et al. (2018) through an approach that utilized the height map of a two-dimensional grid created with a 64-channel LiDAR sensor [18]. Incoming points in the point cloud were immediately put into an occupancy grid and sorted by height. The authors then sorted the occupancy grid points to obtain different plane blocks for the whole frame. These planes included data characteristics such as maximum height, minimum height, and intensity values. Pre-determined height thresholds were then used to discern plane blocks that are lower and constitute the road layer and plane blocks that contain objects, whether they be on the road surface or overhanging. In ambiguous cases, where objects may have a small height value or may be part of a slanted road, the variance in intensity returns over that plane block can aid its classification as a pavement layer or an object. LiDAR data intensity return values from pavement, for example, tend to show much smaller variances than those from pedestrians or other vehicles. From here, Wang et al. (2018) clustered the grid into objects using a spatially varying threshold. Due to the geometry of the laser planes in the sensor, objects that are further away in the point cloud have a larger grouping radius threshold value than objects that are closer to the sensor. The multi-frame fusion approach was used to improve the motion state of tracked objects. An SVM was used to classify vehicles, pedestrians, and bicycles. The entire process only took 10 ms per frame, substantially faster than previous solutions. The faster run time is particularly achieved because Wang et al. (2018) reduced the clustering problem to $O(g)$ time complexity, where g is the number of grid elements and O is the time complexity of the algorithm, a measure of efficiency

Another real-time solution built around obstacle grids and multi-frame fusion was proposed by Xie et al (2019) [27]. In their approach, once road segmentation was complete, the point cloud area was reduced into a 200 x 200 obstacle grid with uniform grid size (~ 40 cm x 40 cm, given the sensor's FOV). A novel algorithm, called eight-neighbor cells clustering, clustered groups of adjacent obstacle cells within the grid. Multi-frame static and dynamic obstacle detection was then carried out by tracking a subset of points in each obstacle grid over six subsequent frames. A similarity value between each object based on lateral and longitudinal position was used for data association between frames. Once associated, objects were tracked using a KF and a novel dynamic tracking point box model. Static obstacle detection, dynamic object tracking, road segmentation, and clustering were performed with an average run time of 96 ms per frame. Xie et al. attained near real-time performance because of their custom clustering algorithm and the decision to only track moving objects judged to be in the drivable area, thereby minimizing overhead calculations.

Both aforementioned approaches achieved near real-time processing when tracking objects with a LiDAR sensor in complicated driving environments. Both implemented fast road segmentation algorithms and focused on reducing the computational time needed to data associate and track objects. Although both approaches relied on the reduced resolution of occupancy grids, which can contain thousands of points themselves, the approaches leveraged the tradeoff between processing the entire point cloud for absolute accuracy and down-sampled the point cloud for faster computation. Future LiDAR tracking algorithms will need to make the same tradeoffs, implementing novel versions of occupancy grid formulation based on different forms of clustering.

Implementation of these approaches into practitioner tools is currently a very dynamic environment. At this time, pcl offers some implementations of these approaches, including modules for point cloud transformations between frames for moving sensors; plane estimation and segmentation using RANSAC; down-sampling point clouds using voxels, octrees, and occupancy grids with height maps; spatial density estimators for data returns, clustering methods based on Euclidean or statistical distances; region growing methods; nearest neighbor searches; three-dimensional object detection with centroid estimators; and GPU-leveraging configurations for computing platforms [13]. The current investigation leveraged these libraries offered by pcl and the methods in some of these previous investigations to develop an effective LiDAR tracking solution in a simplified driving environment. Specifically, ground plane estimation was performed through RANSAC and point cloud filtering was based on generating voxel grids. From the voxel grids, obstacle clustering with the NN data association technique was performed. Static and dynamic object classifications was made based on the cluster's velocity in the obstacle grid. Finally, a KF implementation was developed to support obstacle tracking. Object classification was necessary in the controlled environment in which the tests will occur. Any moving object in the environment was assumed to be a vehicle and modeled as a point object. Given that the sensors remained static, there was no need for multi-frame fusion or point cloud transformations.

2.3 Sensor Fusion

Perceptual sensors, such as radar and LiDAR, are rarely used alone to provide perception information for a vehicle. Generally, these sensors are combined within the same application to provide redundancy and robustness: the strengths of one sensor can help overcome the weaknesses of another sensor. For example, LiDARs have great spatial resolution, radars natively provide radial velocity of tracked objects, cameras provide color information, and ultrasonic sensors can provide distance measurements at a short range – all of these attributes are useful, if not essential, in attaining a full environmental scan when trying to traverse roadways. Therefore, common automotive system architectures often fuse camera and LiDAR, radar and LiDAR, and camera and radar, but any combination between two or more perception sensors can exist depending on the application and resource limitations. For example, due to their lower costs, some current production vehicles combine camera and radar to provide Society of Automotive Engineers Level 2 (2018) automated driving features [49].

Leveraging a multitude of sensors to provide accurate and reliable data is critical for automated driving. Consequently, there is a substantial amount of research that has been conducted pertaining data filtering and optimization for the implementation of sensor fusion on a diverse range of systems and sensors. Given the aims of the current investigation, however, the focus of this discussion will remain on previous work to fuse LiDAR and radar data.

Sensor fusion, in the context of environmental perception, implies combining the data streams or object outputs of multiple sensors to ultimately reduce the uncertainty about the objects and their current state. If two sensors perceive the same object in the same global space, the system can be more certain of its existence and can combine the data from each sensor to better track the object. Sensor fusion particularly benefits systems that need to perform in complex situations with a variety of potential objects (e.g., driving a vehicle).

A common goal of sensor fusion in automotive applications is to support object detection and tracking tasks. There are two primary methods to achieve sensor fusion for this application: decentralized and centralized fusion. ***De-centralized fusion*** focuses on the individual sensors themselves. Each sensor within the system architecture captures and pre-processes its own data. The tracks from all sensors are used for input into a fusion module that combines them. Often, a second layer of tracking is applied to fused tracks to support global object tracking. The process is often referred to as track-to-track fusion (a.k.a., high level fusion, object list level fusion). Track-to-track fusion offers a straight-forward and intuitive process to combine sensor readings and outputs that doesn't require any modifications to sensor-specific software. Other benefits include low bandwidth requirements and ease of implementation. The only extra modules needed are those to combine tracks after sensor processing, which often utilize commonplace data association techniques to manage the global list of object tracks – tracks from two sensors may converge into one when they track the same object, diverge into two tracks when two close objects begin to split apart, or be disassociated when one sensor tracks an object not perceived by the other sensor. Statistical probabilities and model parameters can help determine the occurrence of each case. Drawbacks of track-to-track fusion generally stem from unsynchronized sensors.

In contrast, ***centralized fusion*** uses all sensor data as input before any object detection and tracking is performed. Incorporating all data from the sensors before running detection and tracking algorithms ensures that the system has as much data as possible to make decisions. A small amount of pre-processing is usually done for some sensors (e.g., ground plane removal and general clustering for LiDARs) leaving only the most important features of each sensor's measurement frame. These features conform the input from which a central tracking algorithm can associate and develop tracks. As a result, centralized fusion is often referred to as low level or feature level fusion. Centralized fusion builds object identification from the ground up, resulting in a more accurate that is harder to implement than de-centralized fusion. Large system communication bandwidth is required, as a substantial amount of data can be available in at any given time, and significant software modifications are generally required for any unique combination of sensors. The process hinges on initial pre-processing for each sensor to identify useful data returns. A similar state space then must be established between sensors to support object mapping, with complexity of this task being dependent on the sensor combination. For example, equating the RGB color frame from camera vision to the x-y-z coordinates of a LiDAR point cloud is very difficult, but finding congruent state spaces between LiDAR and radar is much easier. Finally, object identification, tracking, and data association are carried out in the state space based on modified versions of the previously discussed approaches. Centralized fusion is much easier to implement with sensors that have similar output structures, such as radar and LiDAR.

Hybrid approaches have also been developed. For example, one sensor may initially identify and track objects on its own and low-level data from another sensor is combined after that process is complete. Usually, this allows the system to detect regions of interest (ROI) that the other sensor will augment, achieving efficiencies in computational time and better tracking within the ROIs. This approach is particularly useful for systems that use camera vision as a sensor, where tracking is typically done both at the sensor and fusion levels to produce global tracks.

Much of the earlier sensor fusion work related to automated driving research focuses on systems that included camera sensors. Kaempchen et al. (2004), for example, used laser scanners to detect possible objects and regions of interest for a forward-facing camera in order to achieve better adaptive cruise control features [28]. A hybrid approach is used that employs object tracking at two levels: only with the laser scanner data, and with camera data added to the laser scanner data. Based on the ROIs identified from the laser scanner module, the camera uses machine vision techniques to identify a bounding box around the vehicle ahead of it and performs tracking at the fusion level. Similarly, Aufrere et al. (2003) focus on camera and laser scanner fusion for short range sensing in urban environments, an area they saw as particularly important for automated driving functions [29]. Their proposed system implements high level fusion with feedback loops between the global object list and the sensors own tracking algorithms. Laser scanners detected objects around the vehicle while the camera tracked the roadside curb. Each obstacle list is fused into a global map that can be associated with future measurements.

As sensors progressed, laser scanners were replaced by multi-channel LiDARs, although camera sensors were retained. A low-level fusion approach between these sensors was presented by Mahlisch et al. (2006) [30]. A forward-mounted LiDAR identified relevant features from the environment and provides ROIs for the camera to detect vehicles. Distance to the vehicle was estimated directly from the observed height and the width of the vehicle was estimated from the camera frame. These combined data measures were provided as inputs to the tracking phase. This method achieved object tracking and classification with an AdaBoost classifier in about 20 ms per frame under normal highway conditions. A similar low-level approach was presented by Monteiro et al. (2006) for slow-moving vehicle applications [31]. A feature extraction module within the laser scanner informed the camera of ROIs in the forward driving area. The camera performed a search in the identified sub-window, and a coordinate transformation put the objects identified in the image plane into common coordinates with the LiDAR. Object tracking and classification were then executed. Wei et al. (2018) described another low-level fusion method for industrial vehicles [32]. Their approach used a 16-channel LiDAR to detect vertical "beacons" that mark off-limit zones for the vehicle. The point cloud was first filtered to remove the ground plane and then all remaining clusters were run through an SVM for beacon identification. At the same time, a camera module used neural networks to identify and calculate beacon locations within the camera frames. The detections were finally fed into a fusion model where object tracking and final confidence values calculated. The system runs at 5 Hz, which was considered acceptable for slow-moving vehicle needs. In all three of these examples, LiDAR is a useful tool for low-level feature extraction that can inform other sensors of specific regions of interest with high spatial accuracy.

Radar has also been paired with cameras to provide greater positional accuracy. Andersson (2017), for example, developed a high-level fusion method between radar and camera sensors [33]. The non-real-time approach centered on a module for radar Kalman filtering and *pre-calculated* positions of objects from the camera. The combination of the two tracks in the fusion module made use of data association and model predictive techniques to perform better than standard tracking software. Ekstrom and Risberg (2018) presented a similar high-level fusion approach, but with simulated stereo vision tracks [34]. The approach used a vehicle box model and an EKF to track forward vehicles with radar. These tracks were then combined with the simulated stereo vision tracks in the fusion model in two ways: combining the tracks to produce global object paths, and feeding these global object detections back into the radar for better data association. Both of these approaches demonstrated increases in tracking accuracy with sensor fusion although they relied on simulated data and non-real-time calculations.

A substantial body of research has examined fusion between the two sensor of interest in this investigation, radar and LiDAR. An early high-level fusion approach between these sensors was presented by Blanc et al. (2004) for vehicle detection on the forward roadway [35]. The process tracked vehicles with the radar, using a KF, and the LiDAR, matching data clusters with a vehicle model. The output tracks were then supplied to a fusion module that combined the tracks and added another layer of Kalman filtering to improve accuracy. The addition of LiDAR assisted in differentiating the lane positions of vehicles at greater distances and providing more accurate velocities than only using radar. Radar and LiDAR sensors, however, have immensely progressed over the last decade in the amount and resolution of data they generate, and modern fusion algorithms have to account for this.

In that vein, Gohring et al. (2011) presented a hybrid low-level fusion algorithm between a front facing radar and an Ibeo LiDAR in a highway vehicle following scenario [36]. The fusion module offered better tracking of the front vehicle than attained with a single sensor and provided a maintained global object list for the vehicle dynamics controller. The radars used directly reported an object list – raw data returns for each cycle were not available. Distance-based clustering was performed with the LiDAR point cloud to extract features, with object detection left to the fusion module. As asynchronous sensor data was obtained, the fusion module attempted to data associate it with an already identified track using the NN technique. KFs were used at the fusion level to track objects and confidence levels, which were passed to the sensor layer to help with feature extraction. The fusion technique leveraged the advantages of both sensors during the on-road tests: velocity positions were slightly better than using only the radar, and positional estimates were better than using only the LiDAR.

A fully implemented high-level fusion method like Gohring et al.'s was proposed by Hajri and Rahal (2018) for forward vehicle tracking on highways and highly curved roads [37]. Focus is on the fusion side of the problem, with object list outputs of the sensors used as direct inputs to the fusion model. As asynchronous data was obtained from the sensors, the fusion model considered the movement of the vehicle since the last recorded measurement and attempted to data associate each object to previously defined obstacle tracks using the GNN method. The fusion model maintained tracks with a constant velocity KF and determined when certain sensor measurements required the addition of a new object track and when an object could no longer be tracked. Building off Gohring et al.'s testing methods, forward vehicle position and velocity estimates were conducted using just the radar, just the LiDAR, and with the fusion method. More robust tracking was achieved with the fusion method.

In contrast, Na et al. (2014) offered a more general-purpose hybrid fusion approach between radar and LiDAR [38]. Radar reported objects automatically, but the point cloud coming from the Ibeo LiDAR was processed by the researchers. First, the point cloud was condensed from three to two dimensions regardless of return height. Then, based on the density of the returns in neighboring cells within the two-dimensional space, different objects were partitioned. The fusion module took as inputs the object list from the radar and the object list from the LiDAR and performed KF tracking. Probabilistic data filters assigned object measurements to tracks. Un-associated measurements were placed in new tracks and a track manager deleted tracks if they were not associated with an incoming measurement over a certain number of frames. Multiple tracks could claim a single incoming measurement based on its probabilistic weight. Due to the large amount of down-sampling in the point cloud, the approach could process a single urban-environment frame in under 10 ms.

Cho et al. (2014) extended these fusion methods from forward vehicle detection to detection of objects at any position around the vehicle [39]. The research-level sensor suite paired six radars with six four-channel LiDARs to provide a 360° FOV. The feature-level fusion approach tasked the sensors to preprocess raw data and extract useful features: radars reported cluster points and LiDARs removed the ground plane, clustered the point cloud, and identified vehicles based on “L” shaped corners. Features from this process were asynchronously fed into the fusion module which data associated each feature to a track using the NN approach and sensor-specific modeling parameters. Objects further away were modeled as a point; closer objects were modeled with a three-dimensional bounding box to estimate volume. An EKF was used for the prediction and update steps of the object tracker. Rear- and forward-facing cameras were included to aid object classification (e.g., vehicle, pedestrian, cyclist) and consequently in determining the best dynamic model for each object. Results showed computational times of 100-200 ms for the multi-sensor fusion; somewhat slower than the needs of current real time systems.

Table 2 provides a brief summary for those works mentioned above.

Table 2: Sensor fusion past work summary

	RADAR	LIDAR/LASER SCANNER	CAMERA	YEAR	DISTINGUISHING FEATURES
KAEMPCHEN ET AL.		X	X	2004	Hybrid approach with ROI identification with laser scanner and then bounding box defined with camera.
AUFRERE ET AL		X	X	2003	High level fusion with camera tracking the roadside curb and a laser scanner detecting close objects.
MAHLISCH ET AL.		X	X	2006	Low-level fusion with ROIs identified with LiDAR and then camera vision estimates vehicle size.
MONTEIRO ET AL.		X	X	2006	Low-level fusion with ROIs identified by the LiDAR and then combined with camera vision data at low speeds. Classification performed after this.
WEI ET AL.		X	X	2018	Low-level fusion at low speeds that identifies beacons with the LiDAR and

					then combined with object tracking from camera vision.
ANDERSSON	X		X	2017	High-level, offline fusion technique that combined radar KF tracks with camera vison object positions.
EKSTROM AND RISBERG	X		X	2018	High-level fusion approach between radar objects and simulated stereo vision objects with track information feedback option for the radar.
BLANC ET AL.		X	X	2004	High-level fusion approach with radar tracks and simplified LiDAR detection. Obtained better lane position estimates at larger distances.
GOHRING ET AL.		X	X	2011	Hybrid approach that combined radar objects and LiDAR clusters. Fusion module performed object classification.
HAJRI AND RAHAL		X	X	2018	High-level fusion that combines the tracks of the radar and LiDAR to track forward objects more accurately than just using a single sensor.
NA ET AL.		X	X	2014	Hybrid approach that combines radar tracks and LiDAR clusters in urban driving scenarios.
CHO ET AL.		X	X	2014	Low-level approach that uses radar clusters and feature extraction from the LiDAR to provide object tracking in a 360° FOV.

Regardless of the fusion approach, these previous efforts indicate the need for extensive filtering of the LiDAR point cloud to extract features of interest and to, when feasible, directly use the radar's object list. Objects are generally associated with previous tracks using a KF and common association techniques. Use of the global object list to inform low-level sensor filtering seems to be useful. Essentially, however, all fusion methods for radar and LiDAR are built at some level off the basic, single sensor tracking methods presented earlier, with choices made in terms of the stage(s) at which object tracking occurs and which KF version is applied (and at which stage(s)). In this investigation, a track-to-track fusion technique was used. Sensor object tracks were conducted at radar and LiDAR sensor level as an intermediate step, with a central track fuser combining sensor tracks as a final step. The high positional accuracy of the LiDAR helped to improve track accuracy when combined with those of the radar.

2.4 Scaled Test Beds

For a full-sized vehicle, the methods presented in the previous two sections offer enough background to initiate advanced development of a fusion system in support of autonomous driving systems. However, the current investigation intends to implement a fusion solution for a small-scaled vehicle in a small-scaled environment. This scaled testbed (STB) vehicle and its scaled environment present novel challenges for fusion methods, especially those involving radars.

STBs collectively refer to any small-scaled vehicle that resembles the sensor suite and the functionality of full-sized vehicles. STBs allow for initial testing of certain vehicle systems on the small-scale vehicle with subsequent deployment on their full-size counterpart. Test usefulness is a direct function of the resemblance between the STB and its full-sized counterpart. Fully-featured STBs allow testing of vehicle control inputs, dynamic characteristics during the driving tasks, and as of late, ADAS functions with specific sensors and data filtering algorithms.

Equipping STBs with the same sensors and controls as full-sized vehicles is the first step to achieve vehicle similitude. Most small-scaled vehicles adapt Remote Control car platforms at either the 1/4th, 1/5th, or 1/10th of the actual size because powertrain components at that scale are readily available. Required sensors and computer hardware are then added to the existing platform. STBs generally feature inertial measurement units, accelerometers, gyroscopes, a central electric motor with differential or individual motors for each wheel, wheel speed sensors, steering servo motors, on-board central processing units (CPUs) for motor and steering control, and ethernet or wifi connection ports. Some sophisticated STBs may also feature additional ADAS sensors such as laser scanners, LiDAR, stereo vision hardware, cameras, ultrasound sensors, GPS modules, and the additional microcontrollers and connection ports required to deploy these sensors. Capable on-board CPUs along with careful system design is required, particularly as additional sensors are introduced.

In general, STBs offer several advantages for engineers and developers. First, ***expense*** – STBs are less expensive to create than a full-sized prototype vehicle. Second, ***time*** – STBs require less time to build; tests using STBs are easier and faster to conduct than those on full-sized vehicles. Third, ***risk*** – STBs reduce the physical risk for all people involved in the testing which ultimately reduces business risk. Fourth, ***reality*** – STBs can more easily expose a vehicle's physical limitations and more intuitively demonstrate vehicle functionality than software simulations. Overall, STBs are one tool in a large toolchain available for systems development engineers and efficiently bridge virtual testing and full-scale implementation. When used in combination with other approaches, STBs can accelerate the development of driving functions, especially when used for physical "smoke" tests of certain ADAS aspects.

The use of STBs for automotive research is not novel. Early models aimed at ADAS function testing began to be developed in the late 1990s. As automated driving progressed, STBs adapted to incorporate many of the required sensors. Early on, STBs were used to test vehicle dynamics and software controllers. One of the first modern systems was proposed by Brennan and Alleyne (2001) [40]. This STB used a 1/5 scale vehicle with various configurations, including two-wheel and four-wheel drive with direct current motors and two- and four-wheel steering. The STB vehicle ran on a moving beltway and was hardwired to a computer via ethernet. Extensive dynamic similitude testing and control designs for speed and steering motors were conducted with the STB, with results extrapolated to a full-sized vehicle. Longoria et al. (2004) presented another STB vehicle implementation used to test anti-lock braking dynamics [41]. The 1/5 scale STB vehicle was outfitted with front disk brakes, drive shaft encoders, and control units to measure braking profiles when ABS was activated after a hill descent. Dynamics between the STB vehicle and a full-sized vehicle were compared. Electronic stability control tests were performed with an STB by Katzourakis and Katzourakis (2008) [42]. Using gyroscopes, accelerometers, potentiometers, wheel encoders, and other microcontrollers, the research focused on control inputs for vehicle dynamics for different turning radii.

As automated driving has progressed, STBs have followed suit to allow testing of the wide range of sensor applications needed for advanced driving systems. Xu et al. (2017) developed the PaTAVTT STB [43]. The STB vehicles for Xu et al. (2017) incorporated the basic motors and sensors needed for dynamic control but augmented with cameras, ultrasound sensors, and an indoor positioning system. Cameras are used to detect lane lines, ultrasound sensors detect forward objects, and the positioning system measures vehicle dynamics and trajectory following. Specific tests were conducted to assess traffic flow questions and U-turn dynamics. More recently, an open source and highly adaptive 1/10th scale STB is presented by O'Kelly et al. (2019) [44]. F1/10, as the STB was coined, utilizes IMUs, LiDAR, video camera, on-board computing, and ROS packages to test a multitude of automated driving functions, such as simultaneous localization and mapping (SLAM), forward collision warning, trajectory planning and following, camera vision applications, lane keeping, and vehicle-to-vehicle communications. The STB included a system for a driver to teleoperate the vehicle with a steering wheel and pedals. Many of the algorithms tested at small scale were implemented later in a full-sized vehicle.

Some commercial outfits have offered highly capable and adaptable STBs aimed at removing the start-up barriers for automated driving research, especially research focused AI applications. Qcar, Quansar's self-driving research STB, commercially available, is a 1/10th scale vehicle that mimics the automated driving systems of current automated vehicles. The vehicle includes open source code pre-installed and accommodates other open source plugins like TensorFlow. Navigation algorithms, mapping, V2V communication, object detection, camera vision, and other common ADAS functions run off the sensory and compute systems platform, which includes on-board computing, dynamic controls, a laser scanner, four cameras, stereo-vision, and wifi connectivity [45]. Similarly, Clear Path Robotics Inc. offers the Jackal Unmanned Ground Vehicle. An entry-level robotics research platform, the Jackal is a small but rugged four-wheel vehicle with plug-ins for different robotics or automated driving needs. Equipped with a powerful on-board CPU and other advanced sensors such as differential GPS, cameras, and stereo vision, the Jackal can serve as a tool for quick and precise research for autonomous navigation. Applications such as machine vision, AI, and path following are supported [46]. Both the Jackal and Qcar can aid researchers in quickly developing automated driving functions at small scale with many industry-standard sensors and computing platforms. The platforms feature easily expandable input/output interfaces and plugins for software tools such as MATLAB, Simulink, python, and TensorFlow.

Despite the impressive configurations of the Jackal, Qcar, and those that came before them, no STB was discovered that incorporated automotive grade radar into its functionality, as is required by the current investigation. Because interpreting radar data at small scale is not currently a straightforward process, radar is either completely left out or an ultrasound sensor is used in its place. Consequently, although these STBs are highly adept at modeling the ADAS of some full-sized vehicles, any systems that require radar cannot be directly tested without workarounds or simulated data. Thus, all currently-available STBs lag in useful functionality when it comes to radar. This represents a sizeable problem because many ADASs and other highly-automated driving systems rely heavily on radar object detection. Without including radar, STBs cannot be fully utilized by engineers and developers of automated driving algorithms.

The solution proposed in the current investigation directly addressed this gap in functionality for STBs. The fusion method between LiDAR and radar used the high spatial resolution of the former sensor to inform the latter sensor about potential object locations that the radar cannot reliably detect at small scale. This fusion process, thus, allowed an STB to fully implement a production radar for general purpose vehicle tracking within a scaled environment.

2.5 CONCLUSION

There are certain key processes in object detection and tracking for autonomous driving systems that employ radar and LiDAR – two sensors found in many ADAS and automated vehicle implementations. The processes include Kalman filtering and EKFs, point cloud clustering, ground plane detection, and data association. Depending on the application, sensor fusion approaches may also be necessary. Indeed, these fusion approaches are essential when working directly with STBs, which are the principal tool to be leveraged in this investigation. The resources described in this review are not all-encompassing. Instead, the intention in each summary was to portray key work and associated general research trends.

The STB implemented in this investigation will operate in a simplified environment with minimal clutter in order to focus on the underlying functionality of the system. No advanced tools such as neural networks, machine vision, or adaptable object classifiers was required, and data clustering was used to resolve raw data into a small number of objects of interest. In doing so, the techniques presented in this literature review proved useful in developing the required filtering and tracking algorithm frameworks. The fusion module in this investigation was in turn built off the implementations and resources previously mentioned to develop a simple but effective real-time object detection and tracking system that allowed STBs to use automotive grade radars in combination with LiDAR to track a vehicle in a scaled environment.

2.6 RESEARCH QUESTIONS

The gaps identified via the literature review suggest a number of important research areas related to the effectiveness of radar sensors in scaled environments and the ability of other sensors (e.g., LiDAR) to supplement any shortcomings in radar performance. Based on these gaps, this investigation intends to answer the following questions regarding scaled vehicle tracking and sensor fusion:

1. Compared to full-scale radar tracking, how much does the positional accuracy of a Radar Tracking System (RTS) diminish when tracking objects in a 1/5th scaled environment?
2. Can the RTS tracking accuracy in a 1/5th scaled environment be quantified using standard error metrics?
3. Using a LiDAR sensor and a custom track-to-track sensor fusion technique, can the tracking accuracy in a 1/5th scaled environment be improved?
    a. If present, can the accuracy improvement in the 1/5th scaled environment match the accuracy obtained from the radar at full scale?
4. Can the custom fusion software and LiDAR clustering algorithms operate in real time using current consumer-grade hardware?

CHAPTER 3 – METHODS

To answer the questions outlined in Chapter 2.6, five elements needed to be implemented. The first was the radar and associated tracking software; the second, LiDAR clustering of point cloud data; the third, a software fusion technique; the fourth, a ground truth measurement; and the fifth, a data recording system with sensor implementation for vehicle trial runs. In this work, radar and LiDAR object tracks were independently formulated with data from each sensor and an implemented EKF with the JPDA technique. A central tracker was then developed and used to fuse and combine tracks from each of the sensors. Finally, location and size accuracy metrics were calculated and compared between differential GPS (DGPS) ground truth values and the RTS performance on a full-scaled vehicle, the RTS performance on the 1/5th scaled vehicle, and the fusion technique performance on the 1/5th scaled vehicle. The following sections provide additional detail for each of these elements of the overall process.

3.1 SENSOR IMPLEMENTATIONS AND TRIAL RUNS

The first step in developing tracking filters was to implement a data collection system in ROS to capture radar data returns, LiDAR point clouds, and DGPS ground truth values for each vehicle under surveillance (VUS).

ROS can inherently record and time stamp all messages passed within the system, so the only input information required were the sensor configurations. Using a developed ROS driver for the Continental ARS430 series radar running at 14 Hz, the provided Velodyne ROS driver for the Velodyne PUCK LiDAR set to run at 10 Hz, and custom DGPS ROS drivers, an NVIDIA Nano CPU running Linux was tasked with collecting data for the trial runs. The radar and LiDAR were statically mounted 10 and 20cm, respectively, off the ground, similar to their height when mounted on a small-scale vehicle. Fig. 6 shows sensor FOVs for both radar and LiDAR.

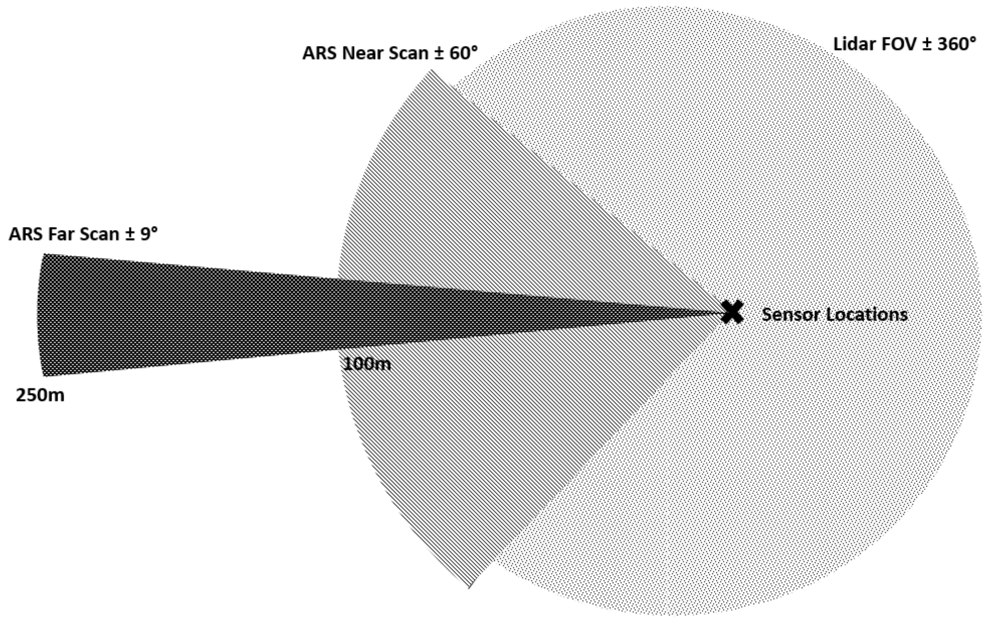

Figure 6: Sensor FOV configurations

Each trial run included a single VUS running through vehicle maneuvers within the radar and LiDAR's FOV in a cluttered, but mostly static environment. Curbs, light posts, fences, and other stationary vehicles were present, but the VUS was the only moving object within the FOV. There were three main types of vehicle maneuvers: driving directly toward or away from the radar sensor, driving diagonally across the radar's FOV, and performing S-turns within the radar's FOV (Fig 7). The first two sets of vehicle maneuvers represented normal driving conditions that the perception sensors and their trackers should easily be able to handle, while the third type of vehicle maneuvers, the S-turns, should challenge the trackers because of the large non-linear movement. The "S-turns" trials were intended to represent driving conditions that would be less apparent within the FOV of the radar or LiDAR sensors than the "Diagonal" and "Straight" trials, particularly if these sensors were installed on a vehicle driving in real world conditions. More extreme vehicle maneuvers, like "figure 8's" or circles, were not considered because these maneuvers would rarely be present in real world driving conditions.

All maneuvers were repeated for the small-scale and full-scale vehicles. The full-sized vehicle traveled at speeds between 10-15 mph (4.5 – 6.7 m/s) while the small-scaled vehicle traveled at speeds between 2-4.5 mph (0.89 – 2 m/s). Speeds were limited in each case by the vehicle scaling. A low speed shuttle is modeled by the small scaled vehicle at 1/5th the size, and, therefore, traveled at 1/5th the speed. Typical low speed shuttles operate at 10 mph or slightly faster, so the full-sized vehicle attempted to maintain similar speeds while the small scaled vehicle was driven at approximately 1/5th those speeds for comparison. Popularity in low speed shuttles with advanced driving systems has increased in the past decade, with many automotive manufacturers and suppliers, such as Continental Automotive, becoming interested in developing advanced driving solutions for these vehicles [60]. Thus, the small scale vehicle used in this investigation was modeled from a low speed shuttle (Fig. 8). The small scale vehicle's wheel base was approximately 1/5th that of a full scale low speed shuttle and, like the full scale vehicle, included both front and rear steering capability. The small scale vehicle featured a top shelf that was located on top of the motor and steering servos and provided a platform for other sensors, such as the DGPS board (not pictured in Fig. 8). The vehicle was driven manually using a remote control device during all the trials.

To accurately scale the small vehicle maneuvers, particularly during the "S-turns" trials, tape was placed at roadway locations where the vehicle should start to change its direction from left-to-right or right-to-left. However, exact positional scaling was not possible due to the use of a manual driving approach – thus, the small scale "S-turn" trials extend to positions slightly outside than the full scale "S-turns" trial when accounting for scale.

All tests were completed during the day with partly cloudy weather conditions and no rain or water on the ground. No effects of sunlight or other environmental conditions were seen in the collected data from any sensor. Each run typically lasted for 20 – 30 seconds. Tests of this duration usually generated 280 – 430 radar frames and 200 – 300 LiDAR point clouds.

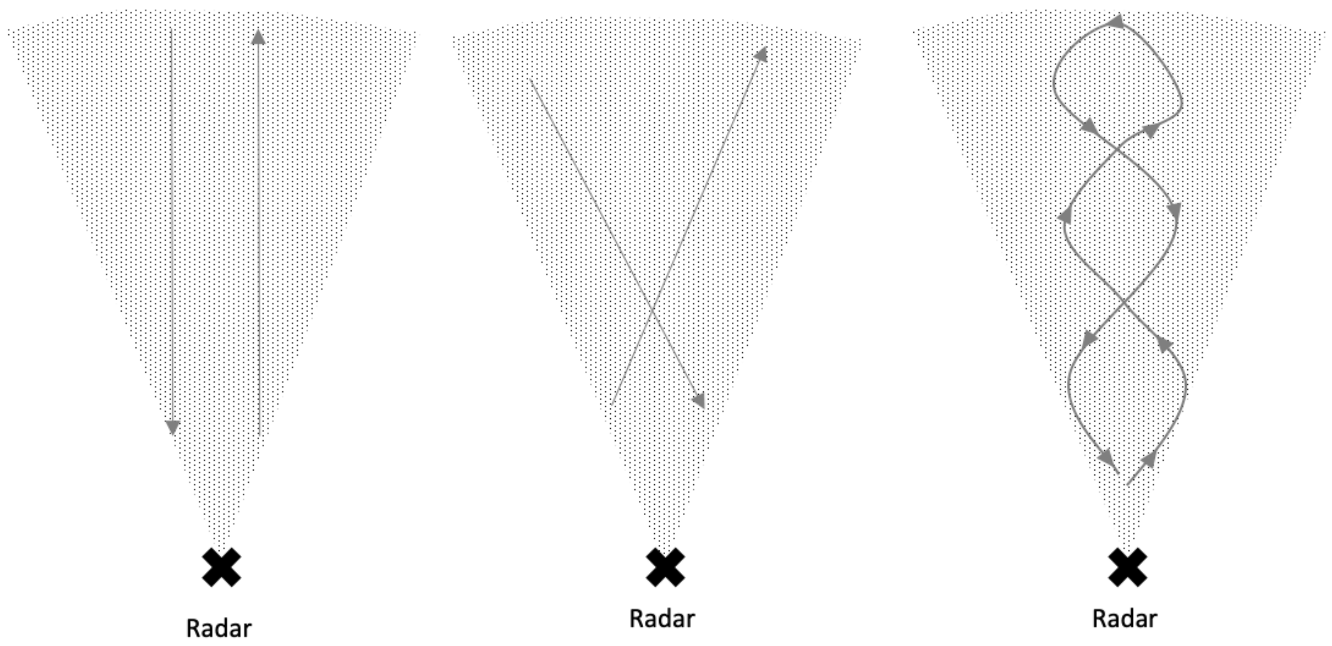

Figure 7: Possible vehicle maneuvers

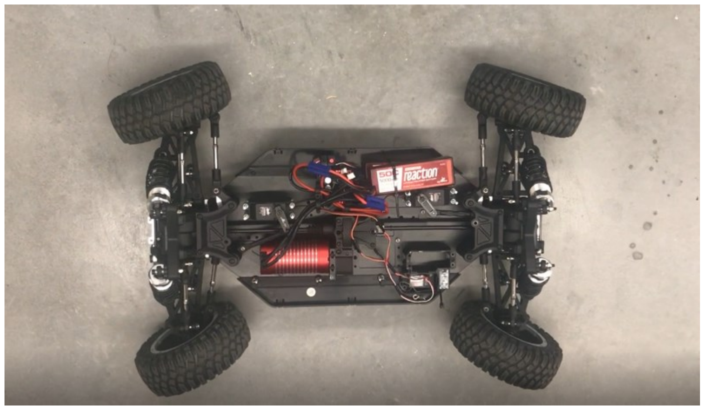

Figure 8: 1/5th scaled vehicle

ArduSimple DGPS boards provided ground truth values for each trial run. One of the boards, configured as a DGPS base station through a multi-hour survey, sends GPS timing corrections to the other board, configured as a rover and installed on the VUS. The ArduSimple system was able to calculate highly accurate position system with error measurements no larger than 12cm any given time, based on recorded pilot data being compared to known positions. Latitude and longitude coordinates were transformed to local sensor coordinates by the DGPS ROS parser.

For each trial run, ROS recordings for all the sensors were timestamped and stored in .bag files for easy playback.

3.2 Radar Tracking Software

Radar tracking software was developed and implemented in the MATLAB environment as part of this investigation. The RTS centered on the Extended Kalman filter (EKF) and the principles previously summarized as part of the literature review. In general, the RTS needed to obtain the radar data returns, filter those returns based on the sensor speed to identify moving objects, cluster returns from the same object, perform object tracking, and save the resultant track information for the duration of each trial. A JPDA point tracker was selected for tracking maneuvering objects within MATLAB as pilot testing suggested that it was the most consistent and tunable tracker out of the alternatives considered[1]. The JPDA displayed the least amount of track switches, lowest false positives in track confirmations, and best ability to ignore clutter during trial runs.

Raw radar measurements were recorded in the radar sensor coordinate frame. Range (ρ), angle (ϴ), and range-rate ($\dot{r}$, along a radial axis from the radar sensor itself) values (Eqn. 11) with timestamped data and other information like radar cross-section (RCS), probability of false detection, signal to noise ratio (SNR), and variance values were recorded for each raw radar data point. There were typically around 100 radar returns per cycle for the JPDA tracker to use. Measurement noise standard deviation values were assumed for each measurement state: 1 m for range values, 1° for angle values, and 0.5 m/s for range-rate values. The corresponding variance values were then calculated as the square of the standard deviations and passed on to the tracker as the measurement variance (Eqn 12). These standard deviation values were adapted from the technical specifications for the radar and generalized for the entire viewing area. Although the expected radar accuracy was higher in some situations, the assumed values produced higher accuracies over the entire FOV when incorporated into the trackers' logic as a measurement variance matrix.

With measurements recorded and being passed to the tracker, the next step was to filter points based on speed. Because the radar is statically mounted and the tracker is only interested in moving objects, any measurement that had a range-rate value of 0, or very close to 0, most likely originated from a static object in the environment and was discarded. Usually, when a radar is mounted to a moving vehicle, all data returns from a cycle need to be transformed into the vehicle frame with velocity components in the x and y directions (where they can then be similarly filtered based on ego vehicle speed). Here, that step is not needed and range-rate values were directly used with a RANSAC algorithm to identify dynamic radar returns.

The next processing step involved the JPDA. As a point tracker, the JPDA could not take in multiple data returns and assign them to one vehicle track. Therefore, an algorithm was needed to cluster measurements that were thought to come from a single object. Two clustering approaches were considered, one that uses the relative distance between points and one that considers the spatial density of certain returns. Ultimately, density-based clustering was chosen for this work because of its accuracy in pilot tests and its ability to differentiate objects in close proximity based on range rate values. To achieve clustering, measurements required a certain number of adjacent points within a given search radius to be

[1] Other trackers investigated for this work included global nearest neighbor (GNN) point trackers and extended object trackers such as the Gaussian mixture probability density filter with rectangular vehicle models. While extended object trackers offered vehicle size estimations, they were most susceptible to noisy data (which generally characterizes radar recordings).

assigned to the same cluster; the search was then free to move on to any of the points identified within the search radius. If they had the minimum number of points within their own search radius then they, too, were assigned to the cluster – if they did not, they were labeled as extraneous. The algorithm works through each point not assigned to a cluster until all were assigned to one of the clusters or labeled as noise. It is important to note that the density based clustering considered each dimension of the measurement, including the range-rate value. If a point was not within the correct range-rate value for a particular cluster, it would not be assigned to that cluster. In general, this helps differentiate objects that are traveling at different speeds within close proximity. The final step to clustering was to calculate the centroid of each cluster and the appropriate measurement noise for that centroid. Averages for each dimension were calculated from the points included in each cluster and used as the centroid for the cluster. The new measurement noise was found as the average noise of all the returns (consistent for all measurements in the case), plus the differences between the average value and measurement values in each dimension scaled by how many points were in the cluster [56]. Clusters with a larger number of points (i.e., a large number of points in space that maintain a minimum density) had a smaller measurement covariance than clusters with a fewer number of points. In essence, because constant values were assigned to measurement noise for the individual returns, the more points there were for a cluster, the more confidence that this cluster truly existed, which would be reflected by lower covariance values. However, thresholds were set for the clustering algorithm such that, if any points were clustered and assigned to a cluster, there was high confidence that the radar sensed something that was actually there. The resulting centroids were then passed on to the JPDA to start tracking.

The JPDA filter reported object tracks with an EKF in the tracking frame – *x* and *y* dimensions with velocity components (Eqn. 13) and the radar sensor at the origin facing along the *x*-axis. The EKF, itself, had a number of important attributes that needed to be defined before any tracking started: the process noise, the state transition model, and the mapping (measurement) function.

Process Noise

Process noise standard deviation values of 1 m in both the *x* and *y* directions modeled any error in the dynamic model for the VUS. A value of 1m allowed the filter to incorporate some expected non-linear motion. With tracking point filters, when the VUS is maneuvering, the cluster centroid may shift depending on the orientation of the vehicle, or just slightly from cycle to cycle. The process noise values selected helped the filter model these slight changes in a shifting tracking point. In general, the process noise was modeled as non-additive noise, meaning the variance associated with each prediction forward in time for the EKF was independent from the previous timestamp prediction.

State Transition Model

The state transition model, **F**, was determined by the constant velocity motion model chosen. This predicted our state vector forward to a specific time (dT) based on previous positioning and velocity readings (Eqn. 14). The constant velocity motion model ensured only the position estimates of the states changed while the velocity components stayed the same. Adequate noise components scaled by the time step were added to the state after propagation and based off the Jacobian of the motion model. Referred to as time-discrete white noise, ***W***, both the current and the previously assigned process noise were directly used in the prediction step of Eqn. 7 in the EKF (pg. 6). In the case of a constant velocity motion model, ***W*** is calculated by Eqn. 15. The process noise is applied to both the positional dimensions and the velocity dimensions to cover any effect of small accelerations on the state of the tracker.

$$z_k = [\rho, \theta, \dot{r}] \tag{11}$$

$$R = \begin{bmatrix} 0.25 & 0 & 0 \\ 0 & 0.25 & 0 \\ 0 & 0 & 0.25 \end{bmatrix} \tag{12}$$

$$X = [x, v_x, y, v_y] \tag{13}$$

$$F = \begin{bmatrix} 1 & dT & 0 & 0 \\ 0 & 1 & 0 & 0 \\ 0 & 0 & 1 & dT \\ 0 & 0 & 0 & 1 \end{bmatrix} \tag{14}$$

$$W = \begin{bmatrix} dT^2/2 \\ dT \end{bmatrix} \tag{15}$$

Mapping (Measurement) Function

The measurement (or mapping) function, commonly denoted ***H***, was defined to convert the state value into the spherical coordinates of measurements reported by the radar. This is particularly important in the update part of the EKF outlined in Eqns. 8, 9, 10 (pg. 6). With measurements reported in the states of Eqn. 11 and the JPDA filter outputting tracks with the states of Eqn. 13, the Jacobian of ***H***, (Eqn. 16) was used to convert those states to the measurement coordinates. Taking the alternative formulation from Bizup et al. (2003), Eqn. 17 was also defined for use.

$$H = \begin{bmatrix} \frac{-y}{x^2 + y^2} & 0 & \frac{x}{x^2 + y^2} & 0 \\ \frac{x}{\sqrt{x^2 + y^2}} & 0 & \frac{y}{\sqrt{x^2 + y^2}} & 0 \\ d\dot{r}/dx & d\dot{r}/d\dot{x} & d\dot{r}/dy & d\dot{r}/d\dot{y} \end{bmatrix} \tag{16}$$

$$H_{alt} = \begin{bmatrix} \frac{-y}{x^2+y^2} & 0 & \frac{x}{x^2+y^2} & 0 \\ \frac{x}{\sqrt{x^2+y^2}} & 0 & \frac{y}{\sqrt{x^2+y^2}} & 0 \\ 0 & d\dot{r}/d\dot{x} & 0 & d\dot{r}/d\dot{y} \end{bmatrix} \tag{17}$$

With all the EKF parameters defined for the tracker, dynamic filtering in pace, and a clustering algorithm available, the JPDA was free to start taking in radar data and begin tracking. Overall, the logic flow of the JPDA tracker followed the outline put forward in the introduction. Measurements were taken in from the radar sensor recording, tracks were predicted forward in time (if there were any), feasible joint events were created for data assignment (at first more coarsely, then with finer definition based on supplied parameters), measurement cost matrices were created for data points, measurements were assigned to tracks, and then state updates were calculated with a constant velocity EKF.

Measurement assignment and track management were the sole responsibility of the JPDA. State predictions and updates largely came from the EKF associated with each tracker. The JPDA needed the definition of several parameter thresholds to accurately assign measurements to tracks for vehicle tracking [57]. These parameters were the detection probability, the initialization threshold, the assignment threshold, the track logic, the confirmation threshold, the hit or miss threshold, and the clutter density.

Detection Probability

The detection probability helped characterize measurement association probabilities for certain tracks and was defined along the interval [0, 1]. Because the VUS in the trials should be clearly visible at all times during the tests, the value was set at 0.9, a relatively high probability of being seen for each cycle.

Initialization Threshold

This parameter, a value between [0, 1], determined when an unassigned measurement should tentatively create a new track based on its probability of belonging to any other track. The threshold was set at 0.1, a relatively low value because at low speeds, measurements that belong to a track should be seen with high probability of assignment. Also, in the physical world, vehicles and other moving objects cannot occupy the exact same space, resulting in object clusters that were adequately far enough apart that the JPDA would assign measurements outside a vehicle's track a low probability of belonging to that vehicle. So, if a measurement was seen outside the cluster, there was a significant chance that it was a new object that could warrant its own new track.

Assignment Threshold

Assignment threshold values helped the tracker determine when exact distances needed to be calculated for measurement cost matrix evaluation. The tracker always performed rough track assignments for all measurements first, before calculating exact distances to tracks for all measurements that were within a certain distance. This saved computation time by eliminating the effects of measurements that were too far away to truly belong to a track in the cost matrix. Possible values for this parameter were on the interval [1, ∞), and a value of 200 was chosen based on the outcomes of preliminary pilot tests with initial data.

Track Logic

Two types of the JPDA tracker were available to implement. One was the normal JPDA that did not take into account the track existence probability when confirming or deleting tracks. The other was the integrated JPDA that performed track maintenance based specifically on track existence probabilities. Preliminary tests favored the former option, which used track history as the primary form of track maintenance.

Confirmation Threshold

Because track maintenance was performed based on history, a confirmation threshold was needed to determine when a track could move from "tentative" to "confirmed." Preliminary tests suggested that a reasonable tradeoff between the likelihood of existence for a track and identification speed was reached when at least 6 measurements were assigned to them in the last 9 time steps before track confirmation occurred. This implied that tracks could be confirmed in as little as 0.42 seconds, since each radar cycle lasted approximately 0.07 seconds.

Similarly, if a track missed at least 10 assignments in any 14 consecutive time steps, it was deleted. Therefore, a track could be deleted in as little as 0.7 seconds.

Hit or Miss Threshold

This threshold value, defined from [0, 1], informed the tracker if a measurement was a hit or a miss for track assignment. Because the JPDA calculated assignment probabilities for each track for all measurements, if the sum of probabilities of assignment for any track did not meet this threshold, the track would be marked as 'missed' for this cycle, or it would be marked as a "hit" if the threshold was met. The JPDA tracker used in this work used a hit or miss value of 0.2.

Clutter Density

The final parameter the JPDA needed was the clutter density. Expressed as the number of false positives for a given unit volume anywhere within the FOV, the clutter density value was helpful for modeling random clutter. A value was chosen at 0.1, higher than might be expected, because there were often radar reflections when vehicles crossed within 10m of the radar.

These parameters were defined during the creation of the JPDA tracking object in the MATLAB software. As the data was pulled in for each time step, the JPDA continued the process of predicting tracks, making data associations, and then creating or culling tracks. The changing state values and covariances at each step in time were saved for later analysis where direct track error metrics could be calculated. The RTS with these characteristics did not need to be changed between recording data for the small scale and full scale tests.

3.3 LIDAR CLUSTERING

Like tracking for radar measurements, important objects needed to be identified in the LiDAR point clouds. It was chosen in this work to only cluster the data on the ROS side and not attempt tracking. This made it easier to implement compatible MATLAB trackers between the radar and LiDAR. The PCL library offers several routines aimed at, first, down sampling the point cloud, and then extracting clusters with their centroids at each time stamp.

Down Sampling

Because the Velodyne PUCK was able to output nearly 300,000 points per second (and some LiDARs are capable of 1,000,000 points per second), the point clouds needed to be down sampled to reduce the computational time to process them. As outlined in the introduction section, one possibility was to use voxels that separate the 3-D space into discreet volumes with specified dimensions. All LiDAR points, measured in x-y-z with an intensity value, that lie within that space are captured by a single representative point for the voxel. Voxels were typically defined as cubes with sides of 3-5cm. The Velodyne software drivers automatically down sampled the point clouds before passing them on to a clustering algorithm.

Ground Plane Removal

To further reduce areas of the point cloud that need to be processed, the ground plane was removed. The ground plane is almost always present in vehicle-implemented LiDARs, but often does not contain any useful data for tracking objects and is often removed or segmented out for other parts of the sensing system. This approach was implemented for this work using RANSAC and height value cut-offs.

Clustering

The voxels remaining after ground plane removal progressed to the object clustering algorithm. The clustering algorithm followed a similar process to the approach described for the radar data. Here, however, relative distance was used to calculate clusters. Points that were within 10cm from each other were considered part of the same cluster. Further requirements for each cluster were put into place, such as minimum and maximum number of points allowed. Once the entire point cloud was looped through and clusters obtained, centroids were calculated by taking the average position of all the points in each clustered object. Measurement noise was calculated in a similar fashion to the clusters in the RTS, except in this implementation the individual points of the cluster had measurement standard deviation errors of 0.03m in each spatial dimension (rather than the individual positional errors of the radar shown previously as 1m for range, 1° for angle, and 0.5 m/s for range rate). This resulted in cluster measurement variance matrices with covariance values around 1 for each dimension in the LiDAR while radar cluster measurement covariance values were often an order of magnitude larger between some dimensions. With both the centroids and associated points identified, tracking was performed downstream on the LiDAR clusters. This required a separate JPDA filter for the LiDAR clusters to generate tracks similar to the RTS. Implementation of JPDA for the LiDAR data required only a few parameter changes to take into account the state space of LiDAR point clouds and their accuracy. With tracks available for both sensors, the next step was to fuse those track outputs.

3.4 Fusion Software

Up to this point, the RTS was able to output tracks from a JPDA tracker and the LiDAR software was able to report clusters for each time step that were converted to tracks by a second JPDA tracker. To complete the sensor fusion, a fusion technique needed to be implemented between the radar and the LiDAR. High-level, or track-to-track, fusion was selected to accomplish this goal (Fig. 9).

MATLAB offers several routines and classes to aid in fusion, including the 'trackFuser' object [58]. Given multiple trackers outputting confirmed object tracks at similar or varying time-stamps, the track fuser maintained a list of central tracks based off the states and covariances of the sensor tracks. The track fuser largely behaved like its own tracking filter, predicting central tracks forward with a process model, assigning measurements to tracks (here the measurements were the sensor tracks), and updating covariances. Data assignment functions, process noise values, confirmation and deletion thresholds, and state transition functions were all supplied to the track fuser similar to the previous JPDA EKF filters, although the track fuser uses a simpler GNN for data association.

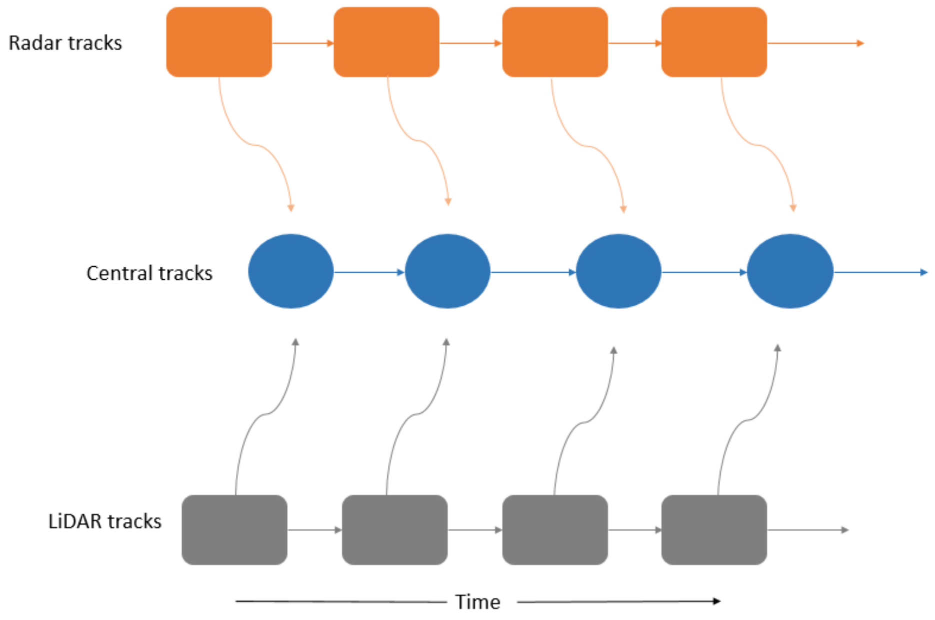

Figure 9: Track fuser example. The radar and LiDAR provide their own tracks for that feed into the central tracker

The only difference in tracking logic between the sensor trackers and the track fuser came from calculating combined state covariances for fused tracks. Covariances for the central tracker could not be calculated in the same way they were in the EKFs because they violate two main assumptions of the Kalman filter that lead to co-dependence between sensor tracks [59].

1) The process noise from measurement or track inputs need to be independent. Cross correlated process noise is a problem for track-to-track fusion because sensor level tracks often track the same object over time with

similar dynamic process models. As the object under surveillance moves over time, the sensor track inputs to the central fuser will incorporate similar, and therefore co-dependent process errors into their state estimates and pass them along to the track fuser. This scenario would result in less accurate state estimates and needs to be taken into account, even when the correlation is unknown.

2) Measurements need to be independent over time and not correlated. In this case, the measurement inputs to the central tracker were other sensor tracks, and these 'measurements' were highly correlated with themselves over time. In the usual case, a radar data return or LiDAR point would have no association to any points in the previous time step and could take on any value, but with tracks calculated through an EKF, each state update is correlated with the state values from the previous time stamps.

Thus, the typical posterior covariance calculations (Eqn. 10) could not be used. An alternative formulation was required.

One common solution for this problem, which was ultimately implemented, was to use the 'intersection' covariance. This technique proposes a weighted optimization problem whose solution conservatively estimates the intersecting Gaussian curves of the track covariances in the face of unknown correlation [59]. The new estimated covariance is the smallest Gaussian curve that contains the intersection of both the input covariances and is generally the most conservative estimate in the presence of unknown correlation (Fig. 10). Given two Gaussian curves with covariance values, P_1 and P_1, and their means, x_1 and x_2, a typical covariance intersection algorithm will follow the equations in Eqns. 18 and 19. Here, w_1 and w_2 are the mixing coefficients that weigh each state covariance matrix [58].

$$P_f^{-1} = w_1 P_1^{-1} + w_2 P_2^{-1} \tag{18}$$

$$x_f = P_f(w_1 P_1^{-1} x_1 + w_2 P_2^{-1} x_2) \tag{19}$$

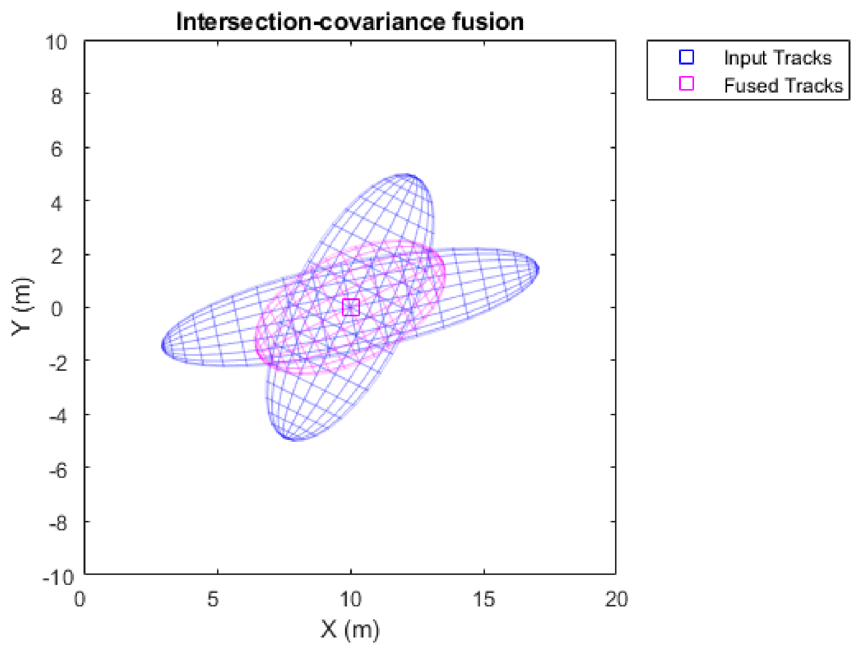

Figure 10: Calculated intersection covariance from two input tracks [58]

The output of the track fuser, along with the independent outputs of tracks from both the radar and LiDAR sensors, could then be directly compared to each other and to the DGPS ground truth values obtained during the data recordings. System time analytics built into MATLAB provided overall runtimes for the LiDAR clustering and JPDA tracking calls.

3.5 Error Metrics

Several error metrics were used to compare accuracy between the ground truth and sensor/fusion tracks. These metrics included the mean squared error (MSE), the root-mean squared error (RMSE), the mean absolute error (MAE), linear correlations, the squared error (SE) at a given time step, and the estimation error squared (EES) at a given time step. Interpolated ground truth values from the DGPS points were used to compare the track positions at each of these time steps and calculate the specified error metric.

Mean Squared Error

The MSE measured the average squared difference between the track values and the ground truth values at each time step the track was present in $meters^2$ (Eqn. 20). Given a vector of track positions, $x_{track,i}$, a vector of ground truth values, $p_{truth,i}$, and the number of time steps, N, the MSE was calculated as:

$$MSE = \frac{1}{N}\sum_{i=1}^{N}(\Delta x)^2, \quad \Delta x = x_{track,i} - x_{truth,i} \tag{20}$$

The MSE was calculated in both the x and y directions to independently analyze longitudinal and lateral track accuracy. For simplicity, only the calculation for the x direction is shown in the previous and subsequent equations. Calculations for the lateral (i.e., y) direction would simply have the x coordinates in each equation replaced by y coordinates.

Root Mean Squared Error

Similarly, the RMSE was calculated through Eqn. 20 with the additional step of taking the square root. The resultant value was in meters. Given an MSE, the RMSE can be calculated as:

$$RMSE = \sqrt{\frac{1}{N}\sum_{i=1}^{N}(\Delta x)^2}, \quad \Delta x = x_{track,i} - x_{truth,i} \tag{21}$$

As before, the RMSE was calculated independently for the x and y directions.

Mean Absolute Error

The MAE was also calculated to compare track accuracy for x and y directions separately and had units in meters. Given a Δx and N as before, the MAE is:

$$MAE = \frac{1}{N}\sum_{i=1}^{N} |\Delta x|, \quad \Delta x = x_{track,i} - x_{truth,i} \tag{22}$$

Lower MAE, MSE, or RMSE values corresponded to higher track accuracy over time.

Linear Correlations

The linear correlation between the track positions and the ground truth vectors was also used as an error metric. More specifically, the Pearson linear correlation coefficient was calculated for this comparison [61]. Given two column vectors, one containing the track values, x_{track}, the other containing ground truth values, x_{truth}, and their means, $\bar{x}_{track}$ and $\bar{x}_{truth}$, the linear correlation was found for both the x and y dimensions using:

$$rho(a,b) = \frac{\sum_{i=1}^{N}(x_{track} - \overline{x}_{track})(x_{truth} - \overline{x}_{truth})}{\sqrt{\sum_{i=1}^{N}(x_{track} - \overline{x}_{track})^2 (x_{truth} - \overline{x}_{truth})^2}} \tag{23}$$

Pearson coefficient values closer to 1 (or -1) indicated strong direct (or inverse) correlation between the track positions and ground truth values.

Estimation Error Squared

The EES characterized track accuracy using covariance values with positional errors for each time step and has sometimes been used to compare multi-object trackers [63]. Given the position errors vector, Δp_i at a given timestamp, i, and the covariance matrix from the sensor track at that timestamp, C_i, the EES for a given track was calculated as:

$$EES = \Delta {p_i}^T {C_i}^{-1} \Delta p_i \tag{24}$$

Larger EES values at a given time step equated to larger covariances and less certainty for a track's position.

Squared Error

The SE was simply the square of the error value for a given time step in the x or y directions. Unlike the MAE, RMSE, and MSE, the SE was calculated at each time step to show the progression in positional error based on the sensor track.

The MAE, RMSE, MSE, AEES, SE, and linear correlation coefficients all characterized a sensor tracking accuracy over time. Moreover, these values were calculated for the full-scale radar trial runs, and then compared to the same metrics calculated for the radar sensor in the 1/5th environment to measure the tracking degradation. Comparisons across experimental conditions leveraged “increase factors,” which are simply the final accuracy (i.e., after an experimental manipulation) divided by the original accuracy (i.e., before an experimental manipulation). The resultant value from the ratio reveals by what factor the value has increased. For example, if the RMSE of a track increased from 0.2 in a full scale test to 0.6 in a small scale test, the RMSE has increased by 3 times, and the increase factor is 3.

These metrics were also calculated across track fusion method to quantify the tracking accuracy increase compared to using only the radar or only using the LiDAR sensor. Percent change between the error metrics of the two input tracks and the error metrics of the fusion tracks was also calculated to show the tracking accuracy increase of using fusion. Similarly, the final fusion track metrics were compared to the original full scale radar track metrics to quantify the track fusion method’s usefulness at small scale.

Finally, there are two important caveats related to this analysis. First, the ArduSimple board self-configured for this project provides accurate global positioning but does not provide any speed data. Therefore, all comparison metrics could only be calculated from positions, not velocities. Second, the small-scale environment tracking had to be directly compared to full scale tracking measurements. Therefore, for compatibility, the track errors in the 1/5th environment were scaled by a factor of 5 before any of the error metrics calculated. Thus, for example, errors of 1 m in the 1/5th environment would be equated to 5 m at full-scale.

Chapter 4 – Results and Discussion

With data from the trial runs recorded and sensor tracking and fusion software developed, error metrics were calculated for each trial run. The full scale trial runs featured radar tracks compared to DGPS ground truth values for all three vehicle maneuvers. The small scale trials featured radar tracks, LiDAR tracks, and fusion tracks for similar vehicle maneuvers, also compared to DGPS ground truth values. Recall that, represented in the 1/5th environment, vehicle size, vehicle speed, and driving distance were all scaled to values at approximately 1/5th the magnitude of their full sized counterparts.

Each full scale and small scale trial produced video recordings of the sensor data and tracks plotted against the DGPS ground truth values at each time step for visual reference. For the sensor track data, there were three plots generated: an overall x vs y graph, an x vs. time graph, and a y vs. time graph[2]. The 4 error metrics (MSE, RMSE, MAE, linear correlation) were also calculated for each trial run, for both the x and y values of the track. Additionally, graphs depicting the EES and SE as a function of time were generated.

4.1 Full Scale Tests

Straight

In the first full scale vehicle trial, the VUS drove straight away from the sensor, turned around, and drove straight back toward the sensor. Fig. 11 shows the track position, track y-values, and track x-values graphed against the DGPS ground truth for this trial, as well as the resulting EES. Fig 12 shows the SE curves for both the x and y dimensions, while Table 3 shows the error metrics for the generated radar tracks.

Diagonal

In the second full scale vehicle trial, the VUS drove diagonally away from the radar sensor, turned around, and the drove diagonally across the radar's FOV on the way back. Fig. 13 shows the track position, track Y-values, and track X-values graphed against the DGPS ground truth for this trial, as well as the resulting EES. Fig 14 shows the SE curves for both the x and y dimensions, while Table 4 shows the error metrics for the trial run's radar tracks.

S-turns

In the final scale vehicle trial, the VUS performed small s-turns while driving away from and back towards the sensor. Fig. 15 shows the track position, track Y-values, and track X-values graphed against the DGPS ground truth for this trial, as well as the resulting EES. Fig 16 shows the SE curves for both the x and y dimensions, while Table 5 shows the error metrics for the trial run's radar tracks. For convenience, red dashes have been added to the lateral movement panels in Figs. 15 and 16 to highlight the beginning of turns that the vehicle made during the S-turn maneuvers.

[2] Due to environmental noise, some tracks were recorded at x values greater than 150m but with y values close to 0. This causes them to be plotted within the limits of the y vs time graph although they may be more than 100m away from the target vehicle. These tracks were considered extraneous to this analysis.

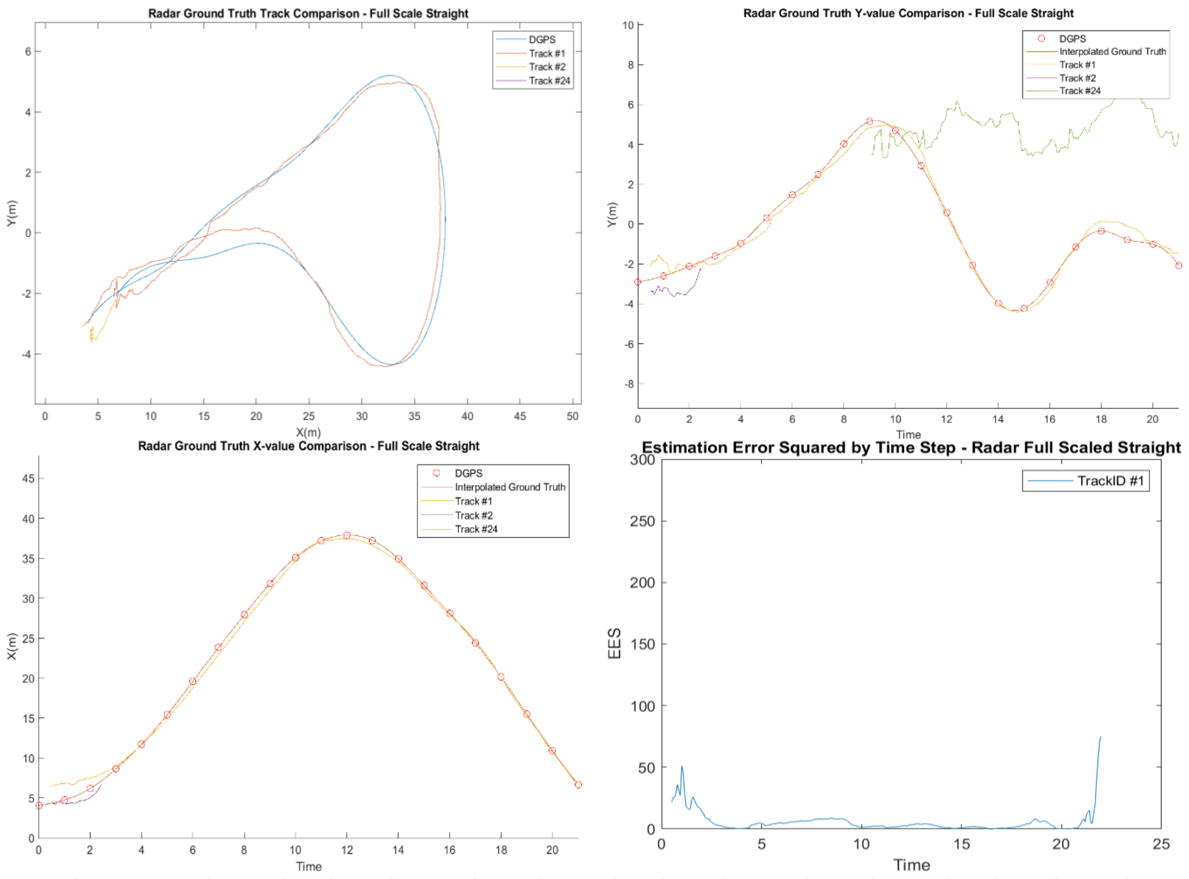

Figure 11: Track position and ground truth overlay, Y-value and ground truth overlay, X-value and ground truth overlay, and EES metric vs time. "Straight" full scale trial.

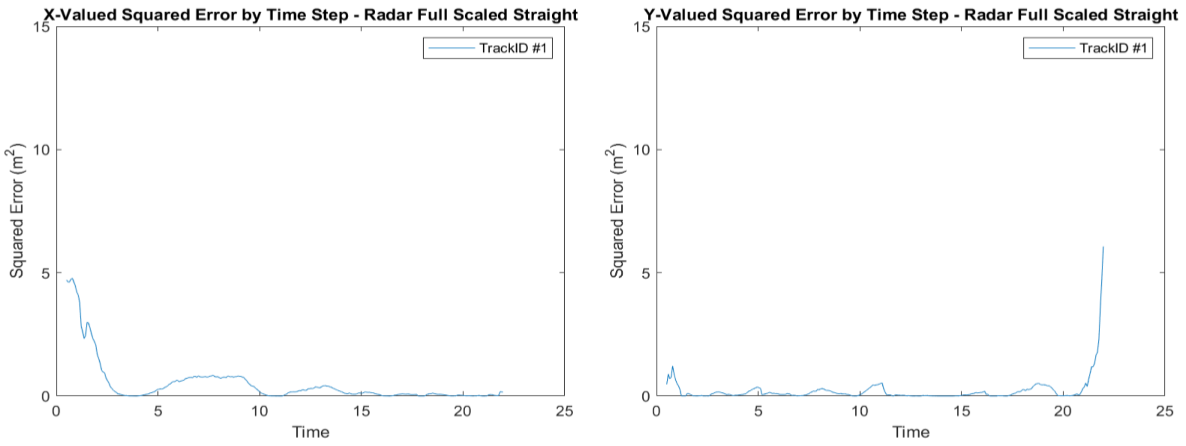

Figure 12: SE curves for the x and y dimensions vs time. "Straight" full scale trial.

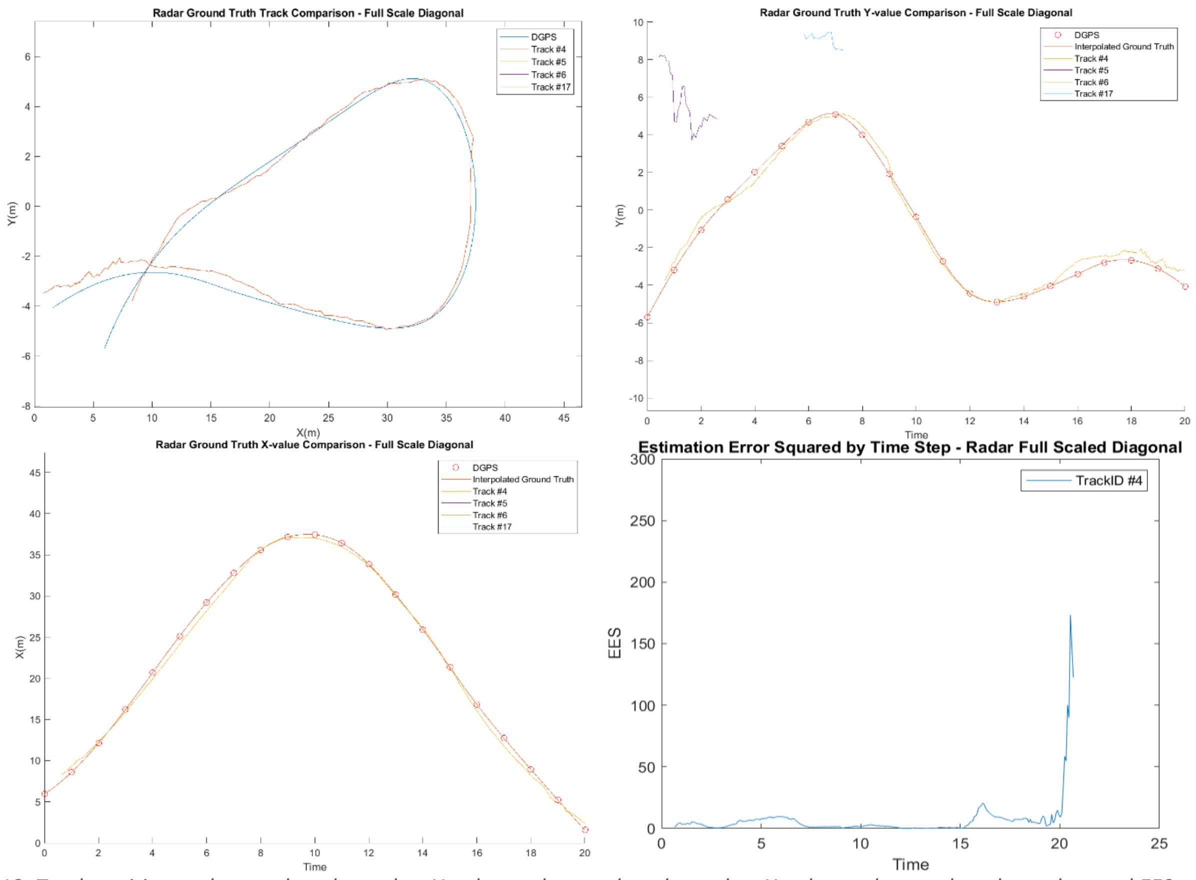

Figure 13: Track position and ground truth overlay, Y-value and ground truth overlay, X-value and ground truth overlay, and EES metric vs time. "Diagonal" full scale trial.

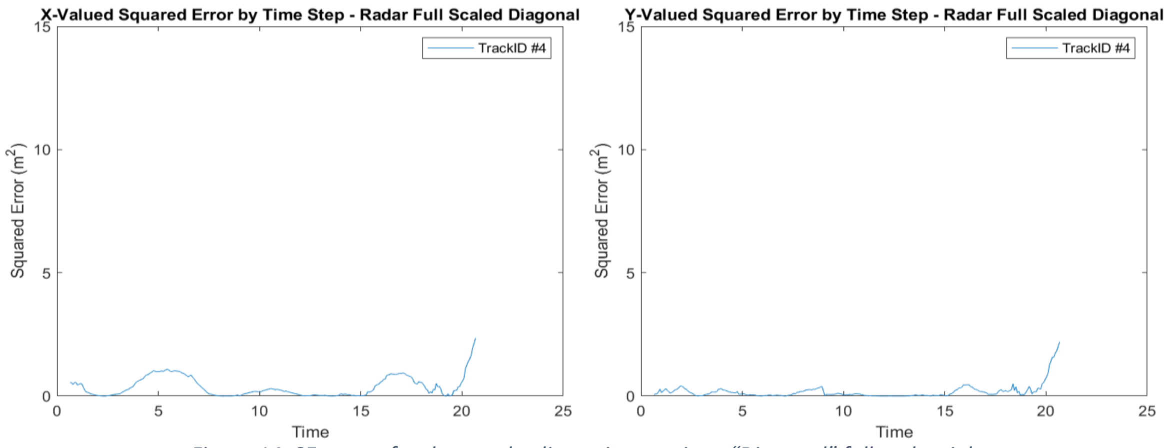

Figure 14: SE curves for the x and y dimensions vs time. "Diagonal" full scale trial.

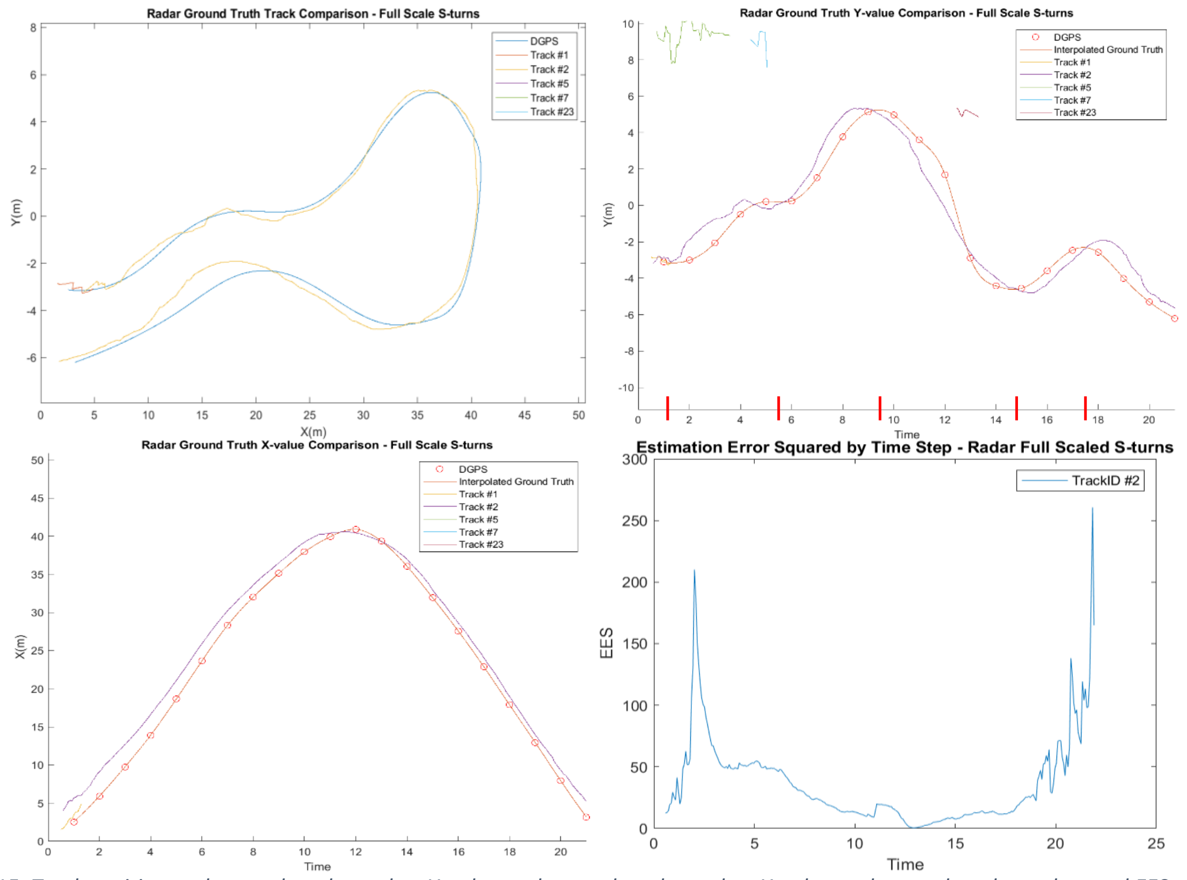

Figure 15: Track position and ground truth overlay, Y-value and ground truth overlay, X-value and ground truth overlay, and EES metric vs time. "S-turn" full scale trial.

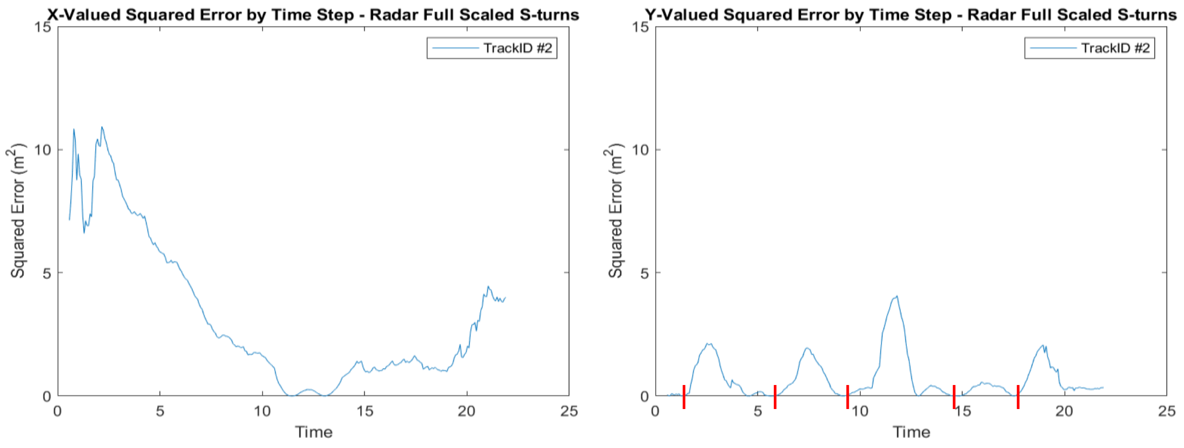

Figure 16: SE curves for the x and y dimensions vs time. "S-turn" full scale trial.

Table 3: Error metrics for full sized vehicle radar tracking, "straight" trial

Full Scale Vehicle "Straight" Trial Run	*X*	*Y*
MSE (m^2)	0.5078	0.2161
RMSE (m)	0.7126	0.4648
MAE	0.5275	0.3378
Linear Correlation	0.9987	

Table 4: Error metrics for full sized vehicle radar tracking, "diagonal" trial

Full Scale Vehicle "Diagonal" Trial Run	*X*	*Y*
MSE (m^2)	0.3726	0.1757
RMSE (m)	0.6104	0.4192
MAE	0.5051	0.3369
Linear Correlation	0.9990	

Table 5: Error metrics for full sized vehicle radar tracking, "S-turn" trial

Full Scale Vehicle "S-turn" Trial Run	*X*	*Y*
MSE (m^2)	3.2372	0.7122
RMSE (m)	1.7992	0.8439
MAE (m)	1.5917	0.6988
Linear Correlation	0.9987	

As expected, the error metrics show that the EKF with a constant velocity motion model and added noise performs best when there are limited amounts of non-linear driving. Comparing the track overlays, the radar tracks follow the DGPS ground truth closer when the vehicle is traveling in a straight line. Areas where the vehicle begins to turn or stops turning often featured larger differences in the ground truth and radar track. This is particularly evident in the "S-turns" trial (Fig. 14). Error metric values associated with the "S-turn" trial were clearly higher than those for the "Straight" and "Diagonal" (compare Tables 3 and 2 with Table 5). In general the graphs of the EES and SE for the "S-turn" are higher throughout the duration of the trial than in the first two trials. However, despite the increase in error metric values for the run, overall the EKF performed reasonably well during the challenging "S-turn" tracking scenario. For all three trials, there was some error with the radar tracks when the vehicle was within approximately 5 meters of the sensor, but accuracy seemed not to be affected at any other range in the FOV.

With high accuracy demonstrated for the "straight" and "diagonal" trials, and successful tracking shown across all three full scale trials, the data metrics for the full-scale were used as a benchmark for the small scale tests.

4.2 Small Scale Tests

In addition to the radar, the small scale tests included the LiDAR and track fuser. Only the error metrics will be shown for the remainder of this section. Associated sensor track graphs (like those that were shown for the full scale tests) are available in Appendices A, B, and C.

Straight

The first small scale trial featured the 1/5th sized vehicle driving straight away and then back towards the sensors. Appendix A shows all graphs for this small scale vehicle trial. Tables 6, 7 and 8 show the error metrics for the radar, LiDAR, and fused tracks.

Table 6: Error metrics for small scaled vehicle radar tracking, "straight" trial

Small Scale Vehicle "Straight" Trial Run, Radar	*X*	*Y*
MSE (m^2)	5.9467	0.5344
RMSE (m)	2.4386	0.7310
MAE (m)	2.2361	0.5692
Linear Correlation	0.9816	0.9426

Table 7: Error metrics for small scaled vehicle LiDAR tracking, "straight" trial

Small Scale Vehicle "Straight" Trial Run, LiDAR	*X*	*Y*
MSE (m^2)	9.2071	1.2424
RMSE (m)	3.0343	1.1146
MAE (m)	2.6984	1.0078
Linear Correlation	0.9740	0.9622

Table 8: Error metrics for small scaled vehicle fusion tracking, "straight" trial

Small Scale Vehicle "Straight" Trial Run, Fused Tracks	*X*	*Y*

MSE (m^2)	3.7869	0.3662
RMSE (m)	1.9460	0.6052
MAE (m)	1.3181	0.3845
Linear Correlation	0.9786	0.9406

Diagonal

The second small scale trial featured the 1/5th sized vehicle driving diagonal away from and then across the sensor FOVs. Appendix B shows all graphs for this small scale vehicle trial. Tables 9, 10, and 11 show the error metrics for the radar, LiDAR, and fused tracks.

Table 9: Error metrics for small scaled vehicle radar tracking, "diagonal" trial

Small Scale Vehicle "Diagonal" Trial Run, Radar	*X*	*Y*
MSE (m^2)	15.2316	11.5255
RMSE (m)	3.9028	3.3949
MAE (m)	3.2308	2.3558
Linear Correlation	0.9521	0.9704

Table 10: Error metrics for small scaled vehicle LiDAR tracking, "diagonal" trial

Small Scale Vehicle "Diagonal" Trial Run, LiDAR	*X*	*Y*
MSE (m^2)	18.3231	3.8939
RMSE (m)	4.2805	1.9733
MAE (m)	3.6328	1.5070
Linear Correlation	0.9598	0.4704

Table 11: Error metrics for small scaled vehicle fusion tracking, "diagonal" trial

Small Scale Vehicle "Diagonal" Trial Run, Fused Tracks	*X*	*Y*
MSE (m^2)	9.6805	6.7198
RMSE (m)	3.1113	2.5923

MAE (m)	1.9745	1.7689
Linear Correlation	0.9530	0.7040

S-turn

The third small scale trial featured the 1/5th sized vehicle driving diagonal away from and then across the sensor FOVs. Appendix C shows all graphs for this small scale vehicle trial. Tables 12, 13, and 14 show the error metrics for the radar, LiDAR, and fused tracks.

Table 12: Error metrics for small scaled vehicle radar tracking, "S-turn" trial

Small Scale Vehicle "S-turn" Trial Run, Radar	*X*	*Y*
MSE (m^2)	2.0691	2.0808
RMSE (m)	1.4384	1.4425
MAE (m)	1.1773	1.2066
Linear Correlation	0.9943	0.9852

Table 13: Error metrics for small scaled vehicle LiDAR tracking, "S-turn" trial

Small Scale Vehicle "S-turn" Trial Run, LiDAR	*X*	*Y*
MSE (m^2)	5.7559	9.9737
RMSE (m)	2.3991	3.1581
MAE (m)	1.9804	2.6277
Linear Correlation	0.9872	0.9317

Table 14: Error metrics for small scaled vehicle fusion tracking, "S-turn" trial

Small Scale Vehicle "S-turn" Trial Run, Fused Tracks	*X*	*Y*
MSE (m^2)	1.2485	2.7226
RMSE (m)	1.1173	1.6500
MAE (m)	0.7049	1.1224
Linear Correlation	0.9924	0.9752

Increase factors were also calculated in order to compare the radar track error metrics from the full scale and small scale trials (Table 15). The same increase factors were computed to compare the radar performance at full scale and the LiDAR performance at small scale (Table 16).

Table 15: MSE, RMSE, and MAE increase factor betwee the full scale radar tracks and small scale radar tracks

Full Scale and Small Scale Radar Comparison, Increase Factor						
	"Straight"		"Diagonal"		"S-turn"	
	X dimension	Y dimension	X dimension	Y dimension	X dimension	Y dimension
MSE (m^2)	11.2	2.5	40.9	65.6	0.6	2.9
RMSE (m)	3.4	1.8	6.4	8.8	0.8	1.7
MAE (m)	4.2	1.7	6.4	7.0	0.7	1.7

Table 16: MSE, RMSE, and MAE increase factor betwee the full scale radar tracks and small scale LiDAR tracks

Full Scale Radar Small Scale LiDAR Comparison, Increase Factor						
	"Straight"		"Diagonal"		"S-turn"	
	X dimension	Y dimension	X dimension	Y dimension	X dimension	Y dimension
MSE (m^2)	18.1	5.7	49.2	22.2	1.8	14.0
RMSE (m)	4.3	2.4	7.0	4.7	1.3	3.7
MAE (m)	5.1	3.0	7.2	4.5	1.2	3.76

Comparison between the tracking metrics of the fusion technique to the sensor tracks metrics was aided by calculation of percent change in the tracking error metrics (Table 17). The table is split into three main columns for each small scale test, and then displays the percent change in the specified error metric cell for the two dimensions assessed within the radar and LiDAR sensor tracks. A positive percent change implied that the fusion approach had that smaller error when compared to the ground truth than the sensor track by itself. A color grading has been added for emphasis and ease of interpretation.

Table 17: Percent change decrease in tracking error metric when comparing fusion tracks to sensor tracks in the x and y dimensions for the three small scale trials

	Small Scale "Straight"				Small Scale "Diagonal"				Small Scale "S-turn"			
	Radar Tracks		LiDAR Tracks		Radar Tracks		LiDAR Tracks		Radar Tracks		LiDAR Tracks	
	x	y	x	y	x	y	x	y	x	y	x	y
MSE (m^2)	36%	31%	59%	71%	36%	42%	47%	-72%	40%	-30%	95%	73%
RMSE (m)	20%	17%	36%	46%	20%	24%	27%	-31%	22%	-14%	53%	48%
MAE (m)	41%	32%	5%	62%	39%	25%	46%	-17%	60%	1%	64%	53%

The fusion track metrics were also compared to the original track errors from the full scale trials. Again, increase factors were used to compare the radar track metrics at full scale for each trial to the fusion track metrics from the paired small scale trials (Table 18). Each trial splits the table into three main columns. On the left side of that column is the error metric increase factor between the radar only small scale tracking scenario and the paired full scale radar tracking trial (see Table 15). For direct comparison, the right side of the column is the increase factor when using the track fusion metrics. Instances when the fusion technique increase track error metrics when compared to only the radar at small scale have been marked in red.

Table 18: Track metric error increase factors between the radar tracks at full scale and the small scale tracks from the radar only and fusion technique (separated between the x and y dimensions)

	"Straight"				"Diagonal"				"S-turn"			
	Small Scale Radar only		Small Scale Fusion Tracks		Small Scale Radar only		Small Scale Fusion Tracks		Small Scale Radar only		Small Scale Fusion Tracks	
	x	y	x	y	x	y	x	y	x	y	x	y
MSE (m^2)	11.2	2.5	7.6	1.7	40.9	65.6	26.3	38.2	0.6	2.9	0.4	3.8
RMSE (m)	3.4	1.8	2.7	1.3	6.4	8.8	5.1	6.2	0.8	1.7	0.6	2.0
MAE (m)	4.2	1.7	2.5	1.1	6.4	7.0	3.9	5.3	0.7	1.7	0.4	1.6

Compared to the full scale tracking, the radar tracking at small scale saw higher metrics, including the EES and SE values, across all runs except the "S-turns" trial (Table 15). There was a clear increase in track errors for the x and y dimensions in the "straight" and "diagonal" small scale trials, along with a slight increase in error in the y dimension of the “S-turn” small scale trials. This indicates that overall tracking accuracy decreased when tracking in a small scale environment using the radar sensor, even when the vehicle was performing simple maneuvers. The “Diagonal” trial posed particular problems for the radar and saw significant error increases. The x-dimension radar track correlation with ground truth was also the lowest for this trial. Compared to the LiDAR sensor at small scale, the radar better followed the vehicle during maneuvers, and even successfully followed the vehicle during the S-turns despite the high number of directional changes. On the other hand, several times the LiDAR track was lagging behind the maneuvers of the vehicle, causing errors to increase during turning events. MSE, RMSE, and MAE metrics were all higher for the LiDAR for all runs, when compared to the small scale radar tracks, except in the “Diagonal” trial, where the LiDAR was more accurate in the y dimension (Table 16).

Overall, he track fuser has the lowest error metric values when compared to the radar and LiDAR rack metrics for all the small scale trials. In all but five instances the fusion method was able to increase, often substantially, the tracking accuracy across the MSE, RMSE, and MAE metrics. When compared to the radar track alone, half the data metrics improved by 30% or more (Table 17). With the LiDAR, 13 out of the 18 conditions improved by more than 30% (Table 17). Out of 18 track metric increase factor comparisons, only twice did the fusion technique deliver overall track metrics that were worse than using only the radar to track the vehicle at small scale (Table 18).

Computational times for the track fusion software were averaged over multiple runs for the small scale trials. While the LiDAR clustering technique can pick out and calculate a cluster center in under 100ms, the JPDA tracker running on a 4 core Intel Core i7-4770 CPU at 3.4 GHz can only execute at average speeds of 1.5 times the length of the recording in the native MATLAB environment. This puts the tracker past the limits of real time requirements. However, C++ code that may be more efficient was not generated and may potentially reduce execution time to near real-time levels.

4.3 Discussion

4.3.1 Full-Scaled tests

The RTS did well when tracking the full-sized vehicle, particularly during the straight and diagonal trials. After the first few seconds of each trial, only one track was confirmed for the VUS and it stayed with the vehicle for the remainder of the trial. For both the “straight” and “diagonal” runs, the MSE and RMSE were well below a value of 1, meaning the average residual of the errors was less than 0.5 m in either the x or y dimensions (Figs. 16 and 17). Video observation of the tracking recording also showed that the radar returns, LiDAR centroids, radar tracks, and DGPS ground truth positions coincided closely during playback of these scenarios.

In contrast with the “straight” and “diagonal” trials, however, the “S-turns” trial resulted in substantially larger error metrics: up to six times higher in the x dimension and three times in the y dimension. Given the pattern of vehicle movement during this trial, it is likely that the Kalman filter used could not adapt to the non-linear movements inherent in the S-turns in order to maintain MSE, RMSE, and MAE values that were similar in magnitude to those observed for the “straight” and “diagonal” trials. To help visualize this, red dashes were added to the y direction track versus ground truth plot (Fig. 15) for the full scale “S-turns” trial and to the corresponding y direction squared error graph (Fig. 16). These red dashes mark the times when the vehicle ended one turn and initiated the next turn. The squared error increased directly after the initiation of each turn, as the vehicle begins to maneuver in the opposite direction and there is a delayed response for the Kalman filter.

It is also possible that tracking point drift may have caused some error in the "S-turns" trials. Because the vehicle was modeled as a single point, the actual projected centroid (i.e., tracking point) position of the vehicle could vary slightly at any time due to its position relative to the radar sensor. For example, when the vehicle was driving away from the radar sensor, the back end of the vehicle dominated the radar FOV. Therefore, in these situations the centroid of the radar returns will be biased toward the rear of the vehicle. Other vehicle-to-radar orientations, however, could have caused the centroid to shift towards either the front, right side, or left side of the vehicle in a similar fashion. When radar data are compared to DGPS data streams, which are not subjects to this artifact, slight errors are possible – particularly in situations where vehicle maneuvers had the potential to markedly shift the tracking point (e.g., the "S-turns" trial). However, when the positional errors in the x and y positions were examined, the observed effect of tracking point drift was relatively small. Both the "Diagonal" and "Straight" trials had periods where the vehicle turned around (resulting in potential tracking point drift). The corresponding error metric values in these conditions were consistently smaller than the "S-turns" trial throughout the entire full scale tests. This supports the assertion that most of the tracking error observed in the S-turn trials was due to the Kalman filter lagging in its adjustment to non-linear movements in the S-turns or to clustering errors and not primarily to tracking point drift. It is useful to note that some ADAS algorithms model the vehicle as a rectangular box in order to minimize the effects of tracking point error. These algorithms tend to require in-depth extended object detection algorithms and longer processing times, and thus were not used in this investigation.

In spite of the increase in the error metrics, however, the tracker still generated useful and reasonable tracks through the S-turns. For example, the MAE in the x-dimension for the S-turn trial reached a maximum of 1.5 m, which is well below the length of a normal vehicle. Other metrics, such as the EES and SE, remained low for all of the full scale trials, including the "S-turn" trial.

Clustering errors also occasionally contributed to increases in error across full scale trials. This was particularly observed near the onset of the full scale trials, where the vehicle was sometimes split into two separate tracks by the radar clustering algorithm. This artifact resulted in a spurious track that was positioned 1.5 m away from the center of the entire vehicle and contributed substantially to the overall error. Generally, however, this issue surfaced only when the full-sized vehicle was within 5 m of the radar sensor. Under these conditions, the vehicle would generate a large number radar returns over the vehicle length. Normally, at distances greater than 10m, there were less than 15 radar returns from the vehicle for any given frame. This distribution of returns was ideal for the clustering algorithm, and at these distances the density based clustering was extremely accurate at identifying the vehicle. The issue was not observed during the small scale tests due to the smaller size of the vehicle.

Other sources of error during the full scale trials included (1) radar reflections and (2) reduced data accuracy at the edge of the FOV. Radar reflections, or ghost reflections, consisted of radar returns that were primarily seen in positions directly behind the vehicle. These erroneous detections were picked up by the sensor and were particularly hard to filter out because they include non-zero range rate values similar to the moving vehicles. Therefore, they were sometimes clustered into possible objects. The reflections were mostly observed when the vehicle was close to the sensor and may have been the result of radar waves bouncing between the pillars of the vehicle and then returning to the sensor. The beginning of some full scale trials featured these ghost reflections degrading accuracy somewhat, although their presence posed more of a problem in the small scale sensor recordings. The end of each full scale trial always featured the vehicle driving out of the FOV of the radar. Because the radar is less accurate in position and range rate values at these high angles, the tracker was also less accurate during these times.

This is especially evident in the "Diagonal" full scale run where there was an increase in the y dimension error at the end of the track and an increase in EES values for timestamps close to the end of the trial.

Although both of these problems, radar reflections and reduced sensor accuracy at the edge of the FOV, were present in the collected data, the radar tracker was highly successful during the full scale tests. This was even the case with a static radar in all trials, which tends to be a more difficult tracking scenario than a dynamic radar situation, since there is a lack of range rate attributes for many returns in the radar FOV. Range rate attributes can be helpful during the clustering process.

4.3.2 Small-Scaled tests

4.3.2.1 Radar and LiDAR Error Metric Comparisons

Compared to the radar track metrics of the full size tests, there was a large increase in the scale-adjusted errors associated with the radar and LiDAR tracks in the small scale test. This effect was particularly evident in the longitudinal (x) direction, which contained most of the trial travel distance. Although the tracker was able to follow the small scale vehicle reasonable well in the "straight" and "S-turn" trials, there were substantial track switching and position errors in the "diagonal" trial. In the EES and SE graphs of the radar tracks for the "Diagonal" trial, the exact point the track switches and attempts to begin tracking the vehicle again is associated with large jumps in error values. A track switch will always be accompanied by a large increase in error metrics, indicating the tracker is struggling to maintain its track of the object. The increased errors are likely partially a result of increased incidence of radar reflections during the small-scale trials. These reflections caused the clustering algorithm to incorrectly include many of them in its cluster centroid determinations, resulting in radar centroids that were not truly there or that were erroneously shifted in position. These extraneous radar reflections tended to be more prevalent in objects that were close to the radar sensor. Because the small scale trials took place at distances that were in general much closer to the radar than the full scale trial, this issue may have contributed to the increased errors observed, especially during the "diagonal" run[3].

Although the full scale trials radar tracker had its worst error metrics during the full scale "S-turns" trial, the small scale "S-turns" trial produced error metrics comparable to the small scale "Straight" trial. Thus, a prediction of poor performance in the small scale "S-turns" trial given the full scale results was not accurate, the tracking algorithm was able to successfully track the vehicle through the small scale "S-turns." This difference in outcomes may be due to the slower speed of the small scale vehicle. Although the small vehicle was exhibiting highly non-linear motion in this trial, the slower speed may have allowed the radar tracker to adjust to the accelerations accurately. Also, because of slight errors in manual driving, the small scale "S-turns" trial featured proportionally larger S-turns than the full scale S-turns. At first glance, this would lead to theorizing that the errors would be higher in the small scale trial because of the larger S-turns, but in reality the radar tracker was able to follow the vehicle more accurately at small scale than full scale. This is most likely, again, due to the speed of the maneuvers. Thus, the small deviations from the exact proportional path did not seem to play a meaningful part in positional errors observed with the tracker. There was, however, an associated increase in the covariance values, showcased in the EES graph for the radar sensor in the "S-turns" trials.

Video and radar cluster analysis showed that the overall number of points detected by the radar from the VUS decreased greatly for the small scale vehicle. Rarely were there more than 4 points returned

[3] The radar reflections are best observed in the tracking videos that accompany this work

from the small scale vehicle; comparatively, there were often at least 10 points returned from the full scale vehicle. Density based clustering required at least two points to be present and any radar reflections seen close to the vehicle could negatively impact clustering and increase track error metrics. Both of these problems were observed in the small scale radar tests and likely contributed to errors in those trials, especially for the "Diagonal" run. Additionally, unlike the full-scale tests, the small-scale tests began and ended within the FOV of the radar (vehicle would drive out of the radar FOV at the end of the full-scale trials. Theoretically, having the small scale vehicle start within the FOV of the sensors could have increased errors as the small scale vehicle began to accelerate. In practice, however, there was no evidence to suggest the radar or LiDAR tracker had increased errors at the beginning of the trials because of the acceleration at the start of trials.

One factor that likely contributed to the surprisingly poor performance of the LiDAR during the small scale trials was the effective cluster range. Because the LiDAR only had 16 channels, small vehicles could slip through the sensor channels at distances greater than 10m, leading to inconsistent LiDAR clustering and poor tracking at these distances. Typical LiDAR clusters come from the point cloud returns of at least two channels, but many times only one channel detected the actual small scale vehicle. This often led to less accurate clustering or failure to cluster at distances closer than 10 m. If the channel in the LiDAR detected the vehicle with points separated by 3 to 4 cm, the RANSAC algorithm would often include those points in the ground plane and remove them from the point cloud, effectively eliminating them from being clustered and tracked. Stronger thresholds could be set to counteract this, but at the cost of added run time for the LiDAR down-sampling and clustering. Using multiple LiDAR sensors or a higher channel LiDAR could alleviate this problem in future similar efforts.

In addition, unlike radar return centroids, the LiDAR centroids do not inherently have associated range rate values. Therefore, the JPDA EKF used with the LiDAR data had to estimate and change the velocity on its own using only positional updates. This limitation resulted in a delayed response and higher positional errors, particularly when the vehicle motion was non-linear, like in the "S-turns" and "Diagonal" small scale trials. The y dimension track comparisons and SE plots demonstrate the LiDAR positional error due to this problem.

Although less accurate than the radar, the LiDAR was still able to track the small scale vehicle in all three tests using only basic clustering techniques. This work did not require occupancy grids like the implementations in [18] and [23] or the multiple frame analysis and dynamic voxel grid comparison of [26] and [27]. This lowers run time during execution and lowers algorithmic complexity, making it more applicable to simpler scaled test beds. Also, none of the approaches in [18, 23, 26, 27] referenced low point cloud density problems for tracked objects. Therefore, it is possible that their implementations may also break down when faced with low point cloud density. Note, however, that most LiDAR visibility problems would become evident at farther distances and with a less urgent need to track for system safety if higher channel LiDARs are used.

4.3.2.2 Fusion Track Metrics

The collected data showed that radar tracking was generally less accurate at small scale. Due to the limits in resolution of the radar and the increased extraneous radar reflections for nearby objects, this was expected. In turn, the fusion method implemented was expected to increase the accuracy of tracking at small scale using the LiDAR and radar tracks as inputs. This was indeed generally observed across trial types and sensors.

Amongst the observed improvements, the “S-turn” small scale trial run benefitted the most from the track fuser. Although the radar sensor, by itself, had relatively low errors for that trial, the fuser was still able to improve performance. The track fuser did produce higher tracker errors in two tests than either the LiDAR or the radar sensors working independently. This was likely due to the large difference in track accuracies between the LiDAR and radar for those tests (e.g., see the y-dimension data in Figs. 19 and 20). The track fuser can improve upon the individual tracks, but only if the accuracies of the individual tracks are within a certain margin. Otherwise, the fusion technique fails to improve upon either track. This is a direct result from using the “intersection” method of estimation covariance values in the track fuser [59]. The intersection method is the most conservative estimate of the covariance values, so if one track has large errors or covariances, it is likely that the fused track will do so as well. In some cases, this resulted in a fused track with an accuracy greater than one individual-sensor track but lesser than another for periods of time. The small scale “Diagonal” trial showed this phenomenon during the track switch of the radar. Because the EES value of the radar significantly increased during this time period, so did the track fuser covariance values and positional accuracy. In that trial, eventually, the track was lost and another track was detected a few time steps later.

Despite this occasional pitfall, out of 18 track metric increase factor comparisons (Table 18), only twice did the fusion technique deliver overall track metrics that were worse than using only the radar to track the vehicle at small scale. These two instances represented a 31% and 18% increase in error metric increase factors for the MSE and RMSE during the “S-turn” trials. For all other instances, the increase factor decreased when using the track fuser in the small scale environment. Just like the various implementations of track-to-track or hybrid level fusion of [36, 37, 38, 39] that noted increased tracking accuracy, this work showed the successful deployments of radar and LiDAR fusion at small scale, using only the clustered centroid of point clouds as low level inputs to a LiDAR tracker. Unlike [38, 39], no feature extraction was needed to model the vehicle in the point cloud to achieve enhanced tracking. Additionally, unlike [36] and [39], high level fusion data was not needed to be passed back down to the sensor level tracks to help with clustering, thus avoiding scenarios where there was increased correlation between track inputs to the track fuser.

However, while the increase factor did decrease for the vast majority of track metrics, in many instances it still remained quite high. The “diagonal” trial provides one such example. The track fuser decreased the increase factor for the MSE in the x dimension by 36%, but the increase factor still remained at 26.3 times the original MSE from the full scale test. This suggests a relationship between the relative accuracy pairings of the sensor tracks being fused. If two sensor tracks have widely different accuracies or covariances sustained over a period of time, the track fuser may fail to produce a track with lower errors.

Although more accurate than using the sensor tracks alone, the track fuser and individual sensor tracks did not operate in real time. The JPDA algorithms implemented by [50] and [51] were slow to data associate and update tracks with given data, even from a simplified environment. Significant time is needed to create the feasible events and then construct cost matrices for each possible measurement pairing in the JPDA trackers. In the future, the GNN trackers described in [9] and [10] could be implemented to produce run times within the constraints of real time execution. However, many scaled testbeds run compute systems with dedicated GPU and CPU systems that could theoretically run some tracking algorithms more quickly than the Intel i7 4770 CPU and MATLAB implementation that was used herein for the tracking algorithms. This remains untested, as specialized C++ code to perform the tracking function was not generated for this effort.

In general, however, this work has shown that a track fuser can increase track accuracy substantially over time when used in a challenging tracking scenario such as a 1/5th scale environment with clutter and highly non-linear vehicle maneuvers.

CHAPTER 5 – CONCLUSIONS

The aim of this work was to establish a method of including radar sensor tracking capabilities in scaled test bed (STB) vehicles. Up to this point, radars have been largely ignored among the sensor suites of these vehicles due to sensor limitations in a small-scaled environment. A sensor fusion approach between radar and LiDAR was researched an implemented to address several questions regarding this topic.

The first was to establish accurate radar tracking software at full scale as a benchmark comparison. Common extended Kalman filter implementations and data association techniques described in Section 2.1 of this work were developed to track a moving vehicle through multiple driving maneuvers at distances less than 75 m. Special attention was given to the constant velocity motion model and both the JPDA and GNN data association techniques for radar tracking. Based off the trial runs of vehicle maneuvers, it was shown that the radar tracking software was capable of overall mean absolute errors of 1.5 m or less for each trial, even in the highly non-linear "S-turn" driving scenario.

Similarly, the same tracking software was used to track a vehicle in a 1/5th scaled environment, albeit with larger errors when accounting for the change in scale. Using the same vehicle maneuvers from the full scale trials, the small scale trials quantified the reduction in accuracy that radar trackers face when operating in a scaled environment. Error metrics commonly increased by factors of 3 to 10, with some increases even as high as a factor of 49.

Attempting to restore accuracy metrics of the radar tracking software required sensor fusion between the radar and LiDAR, two typical sensors found on many highly automated vehicle architectures. Heavily studied, LiDAR point cloud filtering, feature extraction, and clustering was presented in Section 2.2 and adapted to calculate LiDAR centroids for the small scale data recordings in conjunction with the radar. RANSAC algorithms removed ground plane points from the point cloud; distance based clustering extracted clusters and centroids from each frame in under 100ms on average – no specialized feature extraction or occupancy grid was constructed for the LiDAR object detection. The centroids served as inputs to a separate tracker, that while successful at tracking the vehicle at small scale, often produced error metrics that were 4 to 7 times greater errors than associated with the full scale radar tracking.

The increase in tracking accuracy was then quantifiable with the use of a track fuser between the radar and LiDAR sensor tracks. With the high level fusion techniques described in Section 2.3, a track-to-track GNN fuser was implemented with successful results. Tracking accuracy improved by, on average, over 30% for all radar trials at small scale. The fused tracks resulted in increases of up to 70% for the small scale "S-turns" trial. However, while improved, the track errors still remained 3 to 5 times higher than the full scale radar metrics in many cases and failed to operate within the constraints of real-time execution. This suggests that the track fuser can improve upon, but not totally restore, the tracking accuracy of the full scale radar tracks. Despite this, video analysis shows the fuser's ability to maintain tracks for the duration of most driving scenarios, even those with highly non-linear maneuvers.

In lieu of real time constraints, this investigation demonstrates the ability to use radar in small scale environments with an associated track fuser, particularly during offline analysis of sensor recordings. The simplified LiDAR clustering and Kalman filter implementations make the approach accessible to many scaled test bed architectures that already implement a LiDAR sensor. To maintain radar functionality, the fused tracks can be reliably used as an input to any advanced driving assistance system that needs radar track input.

5.1 Limitations

There are a number of limitations that should be addressed when adapting this work. Many revolve around the sensor setups of the full scale and small scale trials. The radar and LiDAR sensors were statically mounted to record data. This made it easier and efficient to transform data into the local vehicle frame. Only the sensor locations from the center of the vehicle it was mounted on were needed, and the locations were constant throughout the trials. For the radar, only dynamic objects had non-zero range rate values, making it easier to pick out moving objects but harder to eliminate clutter or closely spaced objects on the basis of radial velocity. The LiDAR itself had only 16 channels, which limited the object detection to 20 m in the full scale trials and approximately 10 m in the small scale trials. The LiDAR was not used in the full scale trials because of this. Thus, no full scale comparison could be made with the LiDAR and only the statistics in the small scale trials are available for this sensor. There was also no opportunity to quantify the fusion metrics at full scale, given the lack of LiDAR's data input. In addition, LiDAR trackers often use box models to track clusters, however, in this work only centroids were used to update the LiDAR tracker. In general, box models portray more information for a track fuser to use downstream but require adequate cluster size to function.

Other sources of limitation came from the environmental set-up for the trials. The trials were simplified as much as possible with regards to natural clutter and number of objects. Only one moving object, the vehicle under surveillance, was present during the trials. In addition, the trials took place on largely open roads with no other objects in the driveable area. Busier driving conditions are normally seen in typical driving, especially in urban scenarios. This could increase clutter and execution times for clustering in general.

5.2 Future Work

Future work on this topic should focus on improving the radar tracking software, increasing the number of points from the LiDAR, and decreasing run time. One possible way to improve the radar tracking is to use a changing multiple motion model parameter for the Kalman filter. This approach would mainly be helpful when the vehicle is turning; in other situations, a constant velocity motion model could be applied. This could, in theory, improve accuracy if a vehicle begins to turn. Additionally, the sensor recording systems could be adapted to a moving vehicle source to better model real life driving scenarios.

In regard to increased point cloud resolution for accurate clustering, multiple LiDARs could be used for more sensor coverage at higher distances, or a higher channel LiDAR, such as a 32- or 64-channel sensor, could be employed.

Decreasing run time could also be achieved by switching from a JPDA tracker to a GNN tracker that simplifies the data association process greatly but may reduce accuracy. A quantifiable comparison between the tracking accuracy and run time could be performed on a cost-benefit analysis basis. C++ code could also be generated from the MATLAB functions to produce more optimized and faster code for run time comparisons. In addition, sensitivity analysis of the parameters in the GNN trackers and JPDA trackers could be performed in the future to develop optimal trackers.

REFERENCES

[1] H. Meinel, and J. Dickmann. “Automotive Radar: From Its Origin to Future Directions,” *Microwave Journal*, Vol.56. 24-40, 2013.

[2] Continental AG, “ARS 408-21 Long Range Radar Sensor 77 GHz.” Continental Engineering Services, September 2018.

[3] S. Patole, M. Torlak, D. Wang, and M. Ali. “Automotive Radars: A review of signal processing techniques,” *IEEE Signal Processing Magazine*, Vol.34. 22-35, 2017.

[4] R. E. Kalman. A new approach to linear filtering and prediction problems,” *Journal of basic Engineering,* Vol.82. 35-45, 1960.

[5] G. Welch, and G. Bishop. “An Introduction to the Kalman Filter,” UNC-Chapel Hill, TR 95-04, 2006.

[6] R. R. Labbe, “Kalman and Bayesian Filters in Python,” 2015, GitHub repository, https://github.com/rlabbe/Kalman-and-Bayesian-Filters-in-Python.

[7] S. Challa, M. R. Morelande, D. Mušicki, and R. J. Evans. “*Fundamentals of object tracking*,” Cambridge University Press. 2011.

[8] A. Gelb, J. F. Kasper, R. A. Nash, C. F. Price, and A. A. Sutherland. *“Applied Optimal Estimation,”* M.I.T. Press. 1974.

[9] R. F. Stengel. *“Optimal Control and Estimation,”* Dover Publications, Inc. 1994.

[10] Y. Bar-Shalom, X. R. Li, T. Kirubarajan. *“Estimation with Applications to Tracking and Navigation: Theory Algorithms and Software,”* John Wiley and Sons, Inc. 2001.

[11] D. F. Bizup and D. E. Brown. “The over-extended Kalman filter - don't use it!” *Proceedings of the Sixth International Conference of Information Fusion.* 1. 40- 46.

[12] Velodyne Acoustics, Inc. “Velodyne LiDAR Puck,” 63-9229 Rev-A datasheet. 2015.

[13] R. B. Rusu and S. Cousins. “3D is here: Point Cloud Library (PCL),” *IEEE International Conference on Robotics and Automation*. 2011.

[14] D. Xu and Y. Tian. “A Comprehensive Survey of Clustering Algorithms,” *Annals of Data Science.* Vol2. 10. 2015.

[15] Y. Roth-Tabak, and R. Jain. “Building an Environment Model Using Depth Information,” *Computer*. Vol22. 85 - 90. 1989.

[16] “Documentation: Point Cloud Compression – Octree Compression.” Pcl.org. Point Cloud Library. 2018.

[17] A. Elfes. “Using Occupancy Grids for Mobile Robot Perception and Navigation,” *Computer*. Vol22. 46 - 57. 1989.

[18] H. Wang, X. Lou, Y. Cai, and L. Chen. “A 64-Line Lidar-Based Road Obstacle Sensing Algorithm for Intelligent Vehicles,” *Scientific Programming.* 1-7. 2018.

[19] R. Fischler and M. Bolles. “Random Sample Consensus: A Paradigm for Model Fitting with Applications to Image Analysis and Automated Cartography,” *Communications of the ACM.* Vol24. 619-638. 1981.

[20] M. Shi, Q. Ling, Z. Yu, and J. Zhu. “Association using modified Global Nearest Neighbor in the presence of bias,” *Chinese Control Conference, CCC*. 4688-4691. 2013.

[21] A. Mendes, L. C. Bento, and U. Nunes. “Multi-target detection and tracking with a laser scanner,” *IEEE Intelligent Vehicles Symposium*. 796 - 801. 2004.

[22] C. Mertz, L. Navarro-Serment, R. Maclachlan, P. Rybski, A. Steinfeld, AQ. Suppé, C. Urmson, N. Vandapel, M. Hebert, C. Thorpe, and D. Duggins. “Moving object detection with laser scanners. J. Field Robot,” *Journal of Field Robotics*. Vol30. 17-43. 2013.

[23] A. Azim, and O. Aycard. “Detection, classification and tracking of moving objects in a 3D environment,” *IEEE Intelligent Vehicles Symposium, Proceedings*. 802-807. 2012.

[24] R. Kaestner, J. Maye, Y. Pilat, and R. Siegwart. “Generative Object Detection and Tracking in 3D Range Data,” *IEEE International Conference on Robotics and Automation, Proceedings*. 2012.

[25] Y. Zhou, Y. Yu, G. Lu, and S. Du. “Super-Segments Based Classification of 3D Urban Street Scenes,” *International Journal of Advanced Robotic Systems*. Vol9. 2012.

[26] A. Asvadi, C. Premebida, P. Peixoto, and U. Nunes. “3D Lidar-based Static and Moving Obstacle Detection in Driving Environments: an approach based on voxels and multi-region ground planes,” *Robotics and Autonomous Systems.* Vol83. 2016.

[27] D. Xie, Y. Xu, and R. Wang. “Obstacle detection and tracking method for autonomous vehicle based on three-dimensional LiDAR,” *International Journal of Advanced Robotic Systems.* Vol16. 2019.

[28] N. Kaempchen, K. Fuerstenberg, A. Skibicki, and K. Dietmayer. “Sensor Fusion for Multiple Automotive Active Safety and Comfort Applications,” *Advanced Microsystems for Automotive Applications*, 137-163. 2004.

[29] R. Aufrère, J. Gowdy, C. Mertz, C. Thorpe, C. Wang, and T. Yata. “Perception for collision avoidance and autonomous driving,” *Mechatronics*. Vol13. 1149-1161. 2003.

[30] M. Mahlisch, R. Schweiger, W. Ritter, and K. Dietmayer. “Sensor fusion Using Spatio-Temporal Aligned Video and Lidar for Improved Vehicle Detection,” *IEEE Intelligent Vehicles Symposium, Proceedings*. 424 - 429. 2006.

[31] C. Premebida, P. Peixoto, U. Nunes. “Tracking and Classification of Dynamic Obstacles using Laser Range Finder and Vision,” *IEEE Workshop on Safe Navigation in Open and Dynamic Environments*. 2006.

[32] P. Wei, L. Cagle, T. Reza, J. Ball, and J. Gafford. “LiDAR and Camera Detection Fusion in a Real Time Industrial Multi-Sensor Collision Avoidance System,” *Electronics*. Vol7. 2018.

[33] A. Andersson. “Offline Sensor Fusion for Multitarget Tracking using Radar and Camera Detections,” Master’s Thesis. KTH Royale Institute of Technology, School of Computer Science and Communication. 2017.

[34] L. Ekstrom and J. Risberg. “Sensor fusion of radar and stereo-vision for tracking moving vehicles as extended objects,” Master’s Thesis. Chalmers University of Technology, Department of Electrical Engineering. 2018.

[35] C. Blanc, L. Trassoudaine, Y. Guilloux, and R. Moreira. “Track to Track Fusion Method Applied to Road Obstacle Detection,” 2004.

[36] D. Goehring, M. Wang, M. Schnurmacher, and T. Ganjineh. “Radar/Lidar sensor fusion for car-following on highways,” *5th International Conference on Automation, Robotics and Applications*. 407-412. 2011.

[37] H. Hajri and M. Rahal, Mohamed. (2018). “Real Time Lidar and Radar High-Level Fusion for Obstacle Detection and Tracking with evaluation on a ground truth,” *International Journal of Mechanical and Mechatronics Engineering*. Vol12. No8. 2018.

[38] K. Na, J. Byun, M. Roh, and B. Seo. “Fusion of multiple 2D LiDAR and RADAR for object detection and tracking in all directions,” *International Conference on Connected Vehicles and Expo*. 2014.

[39] H. Cho, Y. Seo, B. Kumar, and R. Rajkumar. “A multi-sensor fusion system for moving object detection and tracking in urban driving environments,” *IEEE International Conference on Robotics and Automation*. 2014.

[40] S. Brennan and A. G. Alleyne. “Using a scale testbed: Controller design and evaluation,” *Control Systems*. Vol21. 15 - 26. 2001.

[41] R. Longoria, A. Al-Sharif, and C. Patil. “Scaled vehicle system dynamics and control: A case study in anti-lock braking,” *International Journal of Vehicle Autonomous Systems*. Vol2. 2004.
[42] D. Katzourakis and A. Katzourakis. “Scaled Test Bed for Automotive Experiments: Evaluation of Single Accelerometer Electronic Stability Control,” *Advanced Microsystems for Automotive Applications,* pp239-257. 2008.
[43] Z. Xu, M. Wang, F. Zhang, S. Jin, J. Zhang, and X. Zhao. “PaTAVTT: A Hardware-in-the-Loop Scaled Platform for Testing Autonomous Vehicle Trajectory Tracking,” *Journal of Advanced Transportation*. 2017.
[44] M. O'Kelly, V. Sukhil, H. Abbas, J. Harkins, C. Kao, Y. Pant, R. Mangharam, D. Agarwal, M. Behl, P. Burgio, and M. Bertogna. “F1/10: An Open-Source Autonomous Cyber-Physical Platform.” 2019.
[45] “Qcar – Sensore-Rich Autonomous Vehicle,” Quanser.com. Quanser. 2020.
[46] “Jackal Unmanned Ground Vehicle,” Clearpathrobotics.com. Clearpath Robotics Inc. 2019.
[47] Continental AG, “Technical Product Specification: ARS430 RDI,” Continental AG – Advanced Driver Assistance Systems Business Unit, October 2017.
[48] “Documentation: Downsampling a PointCloud using a VoxelGrid filter.” Pcl.org. Point Cloud Library. 2018.
[49] “Taxonomy and Definitions for Terms Related to On-Road Motor Vehicle Automated Driving Systems,” SAE International, J3016B. 2018.
[50] T. Fortmann, Y. Bar-Shalom and M. Scheffe, "Sonar tracking of multiple targets using joint probabilistic data association," in IEEE Journal of Oceanic Engineering, vol. 8, no. 3, pp. 173-184, July 1983.
[51] J. Fisher and D. Casasent, "Fast JPDA multitarget tracking algorithm," Applied Optics, Vol.28. 371-376. 1989
[52] B. Zhou and N. K. Bose, "Multitarget tracking in clutter: fast algorithms for data association," in IEEE Transactions on Aerospace and Electronic Systems, Vol.29. 352-363, April 1993.
[53] D. Musicki and R. Evans, "Joint Integrated Probabilistic Data Association - JIPDA," Proceedings of the Fifth International Conference on Information Fusion. FUSION 2002. Annapolis, MD, USA, 2002, Vol.2. 1120-1125. 2002.
[54] “Octree2.png” by Nu is licensed under CC 3.0 Attribution Share. 2006.
[55] “Fitted Line.svg” by Msm is licensed under CC 3.0 Attribution Share. 2007.
[56] Ester, M., H.-P. Kriegel, J. Sander, and X. Xiaowei. “A density-based algorithm for discovering clusters in large spatial databases with noise.” In *Proceedings of the Second International Conference on Knowledge Discovery in Databases and Data Mining*, 226-231. Portland, OR: AAAI Press, 1996.
[57] https://www.mathworks.com/help/fusion/ref/trackerjpda-system-object.html
[58] https://www.mathworks.com/help/fusion/ref/trackfuser-system-object.html
[59] Chee-Yee Chong, S. Mori, W. H. Barker and Kuo-Chu Chang, "Architectures and algorithms for track association and fusion," in IEEE Aerospace and Electronic Systems Magazine, vol. 15, no. 1, pp. 5-13, Jan. 2000.
[60] U.S. Department of Transportation (2018) “Low-Speed Automated Shuttles: State of the Practice.” Report no. FHWA-JPO-18-692. John A. Volpe National Transportation Systems Center. Cambridge, MA.
[61] Gibbons, J.D. Nonparametric Statistical Inference. 2nd ed. M. Dekker, 1985.
[63] Schuhmacher, B., B. -T. Vo, and B. -N. Vo. "A Consistent Metric for Performance Evaluation of Multi-Object Filters." IEEE Transactions on Signal Processing, Vol, 56, No, 8, pp. 3447–3457, 2008.

APPENDIX A

SMALL SCALE "STRAIGHT" TRIAL RUN GRAPHS

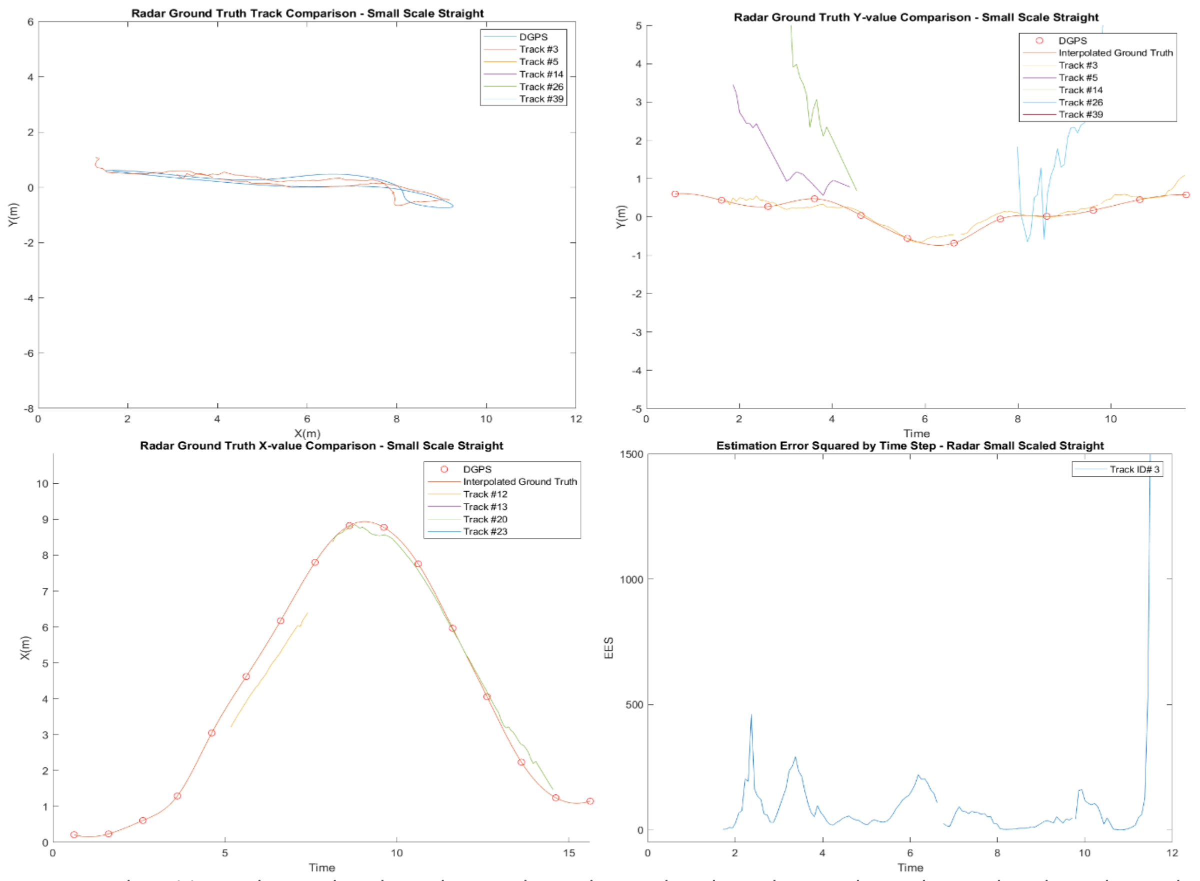

Figure 17: Track position and ground truth overlay, Y-value and ground truth overlay, X-value and ground truth overlay, and EES metric vs time. "Straight" small scale trial, radar tracks.

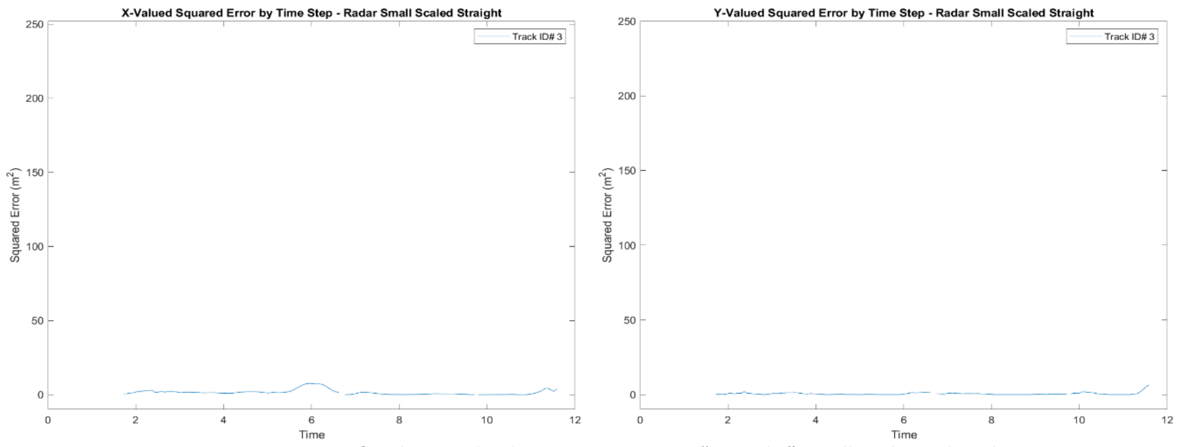

Figure 18: SE curves for the x and y dimensions vs time. "Straight" small scale trial, radar.

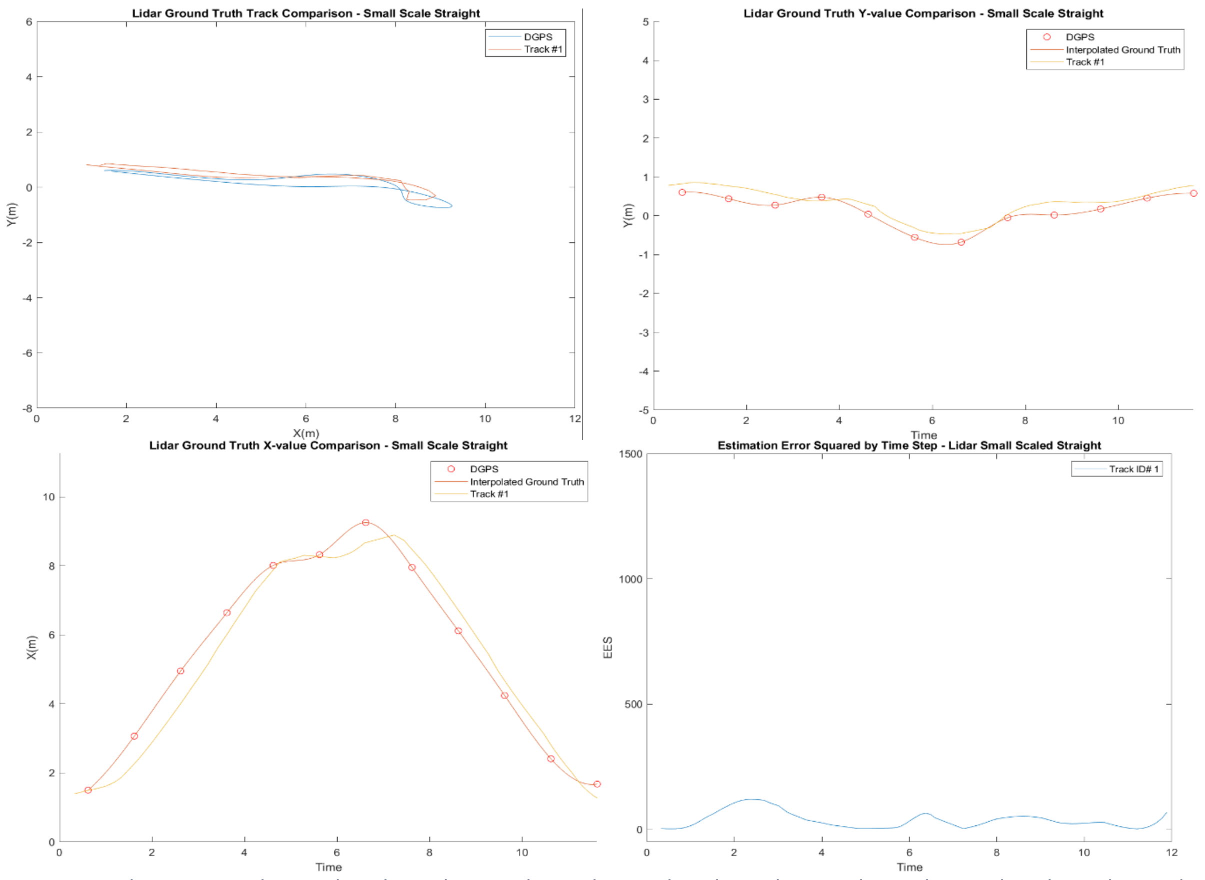

Figure 19: Track position and ground truth overlay, Y-value and ground truth overlay, X-value and ground truth overlay, and EES metric vs time. "Straight" small scale trial, LiDAR tracks.

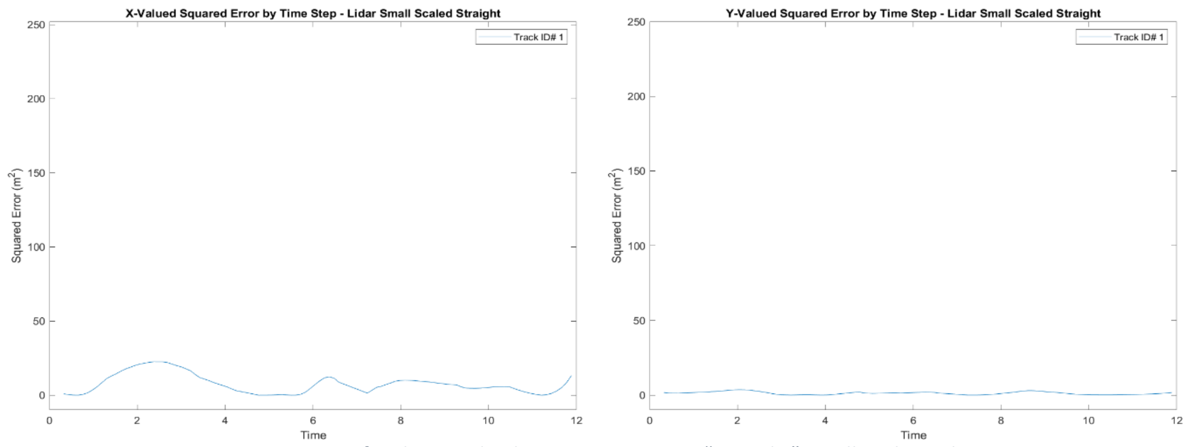

Figure 20: SE curves for the x and y dimensions vs time. "Straight" small scale trial, LiDAR.

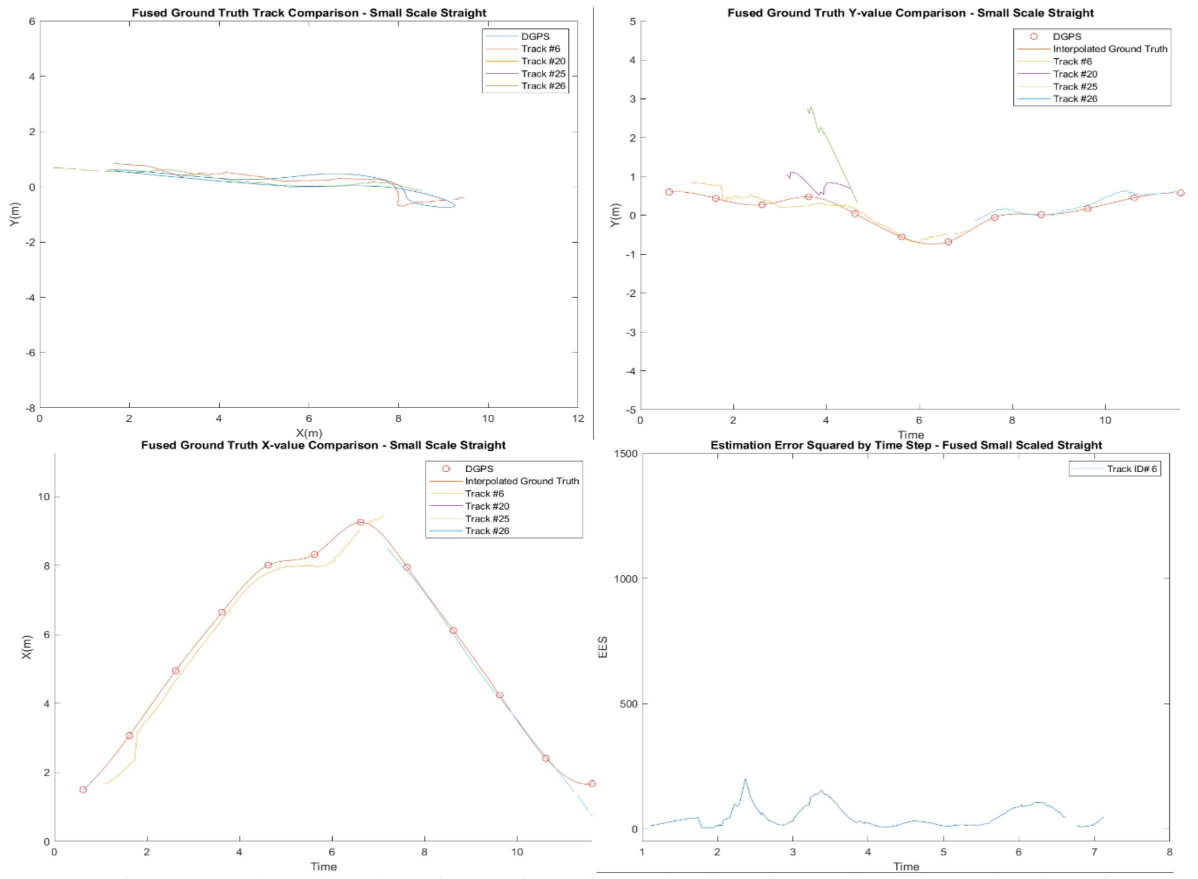

Figure 21: Track position and ground truth overlay, Y-value and ground truth overlay, X-value and ground truth overlay, and EES metric vs time. "Straight" small scale trial, fused tracks.

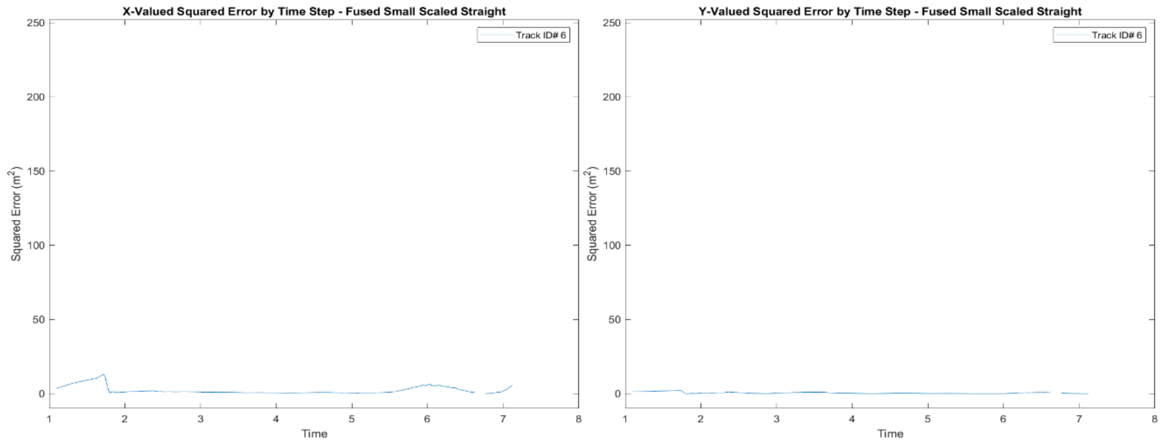

Figure 22: SE curves for the x and y dimensions vs time. "Straight" small scale trial, track fuser.

APPENDIX B

SMALL SCALE "DIAGONAL" TRIAL RUN GRAPHS

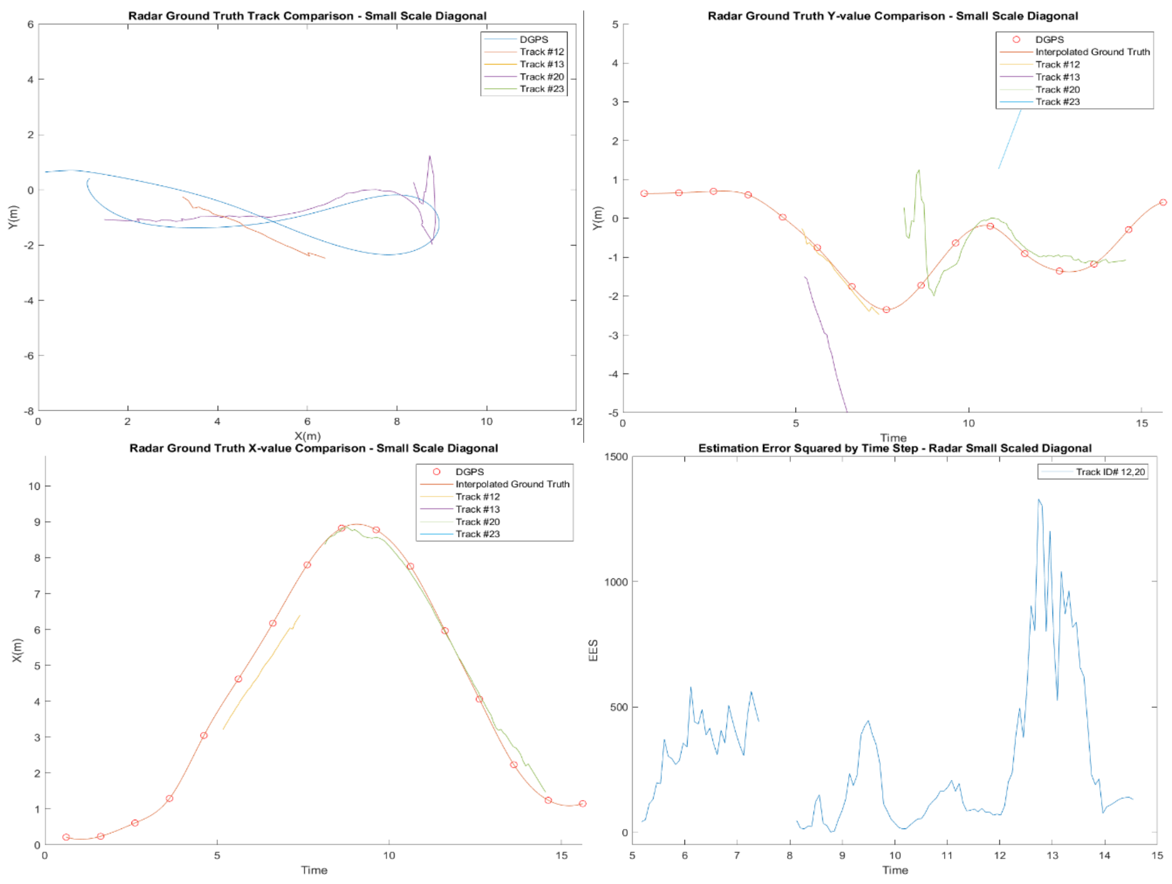

Figure 23: Track position and ground truth overlay, Y-value and ground truth overlay, X-value and ground truth overlay, and EES metric vs time. "Diagonal" small scale trial, radar tracks.

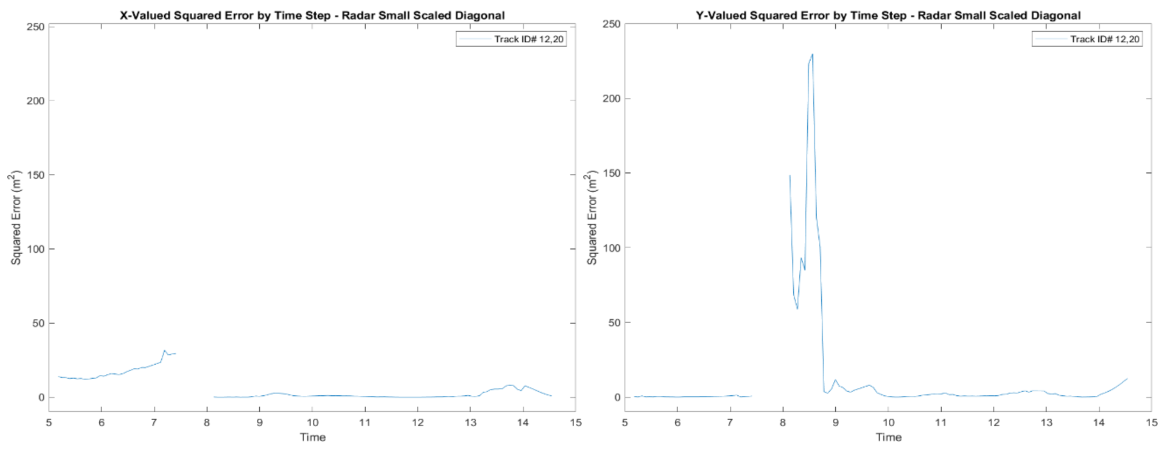

Figure 24: SE curves for the x and y dimensions vs time. "Diagonal" small scale trial, radar.

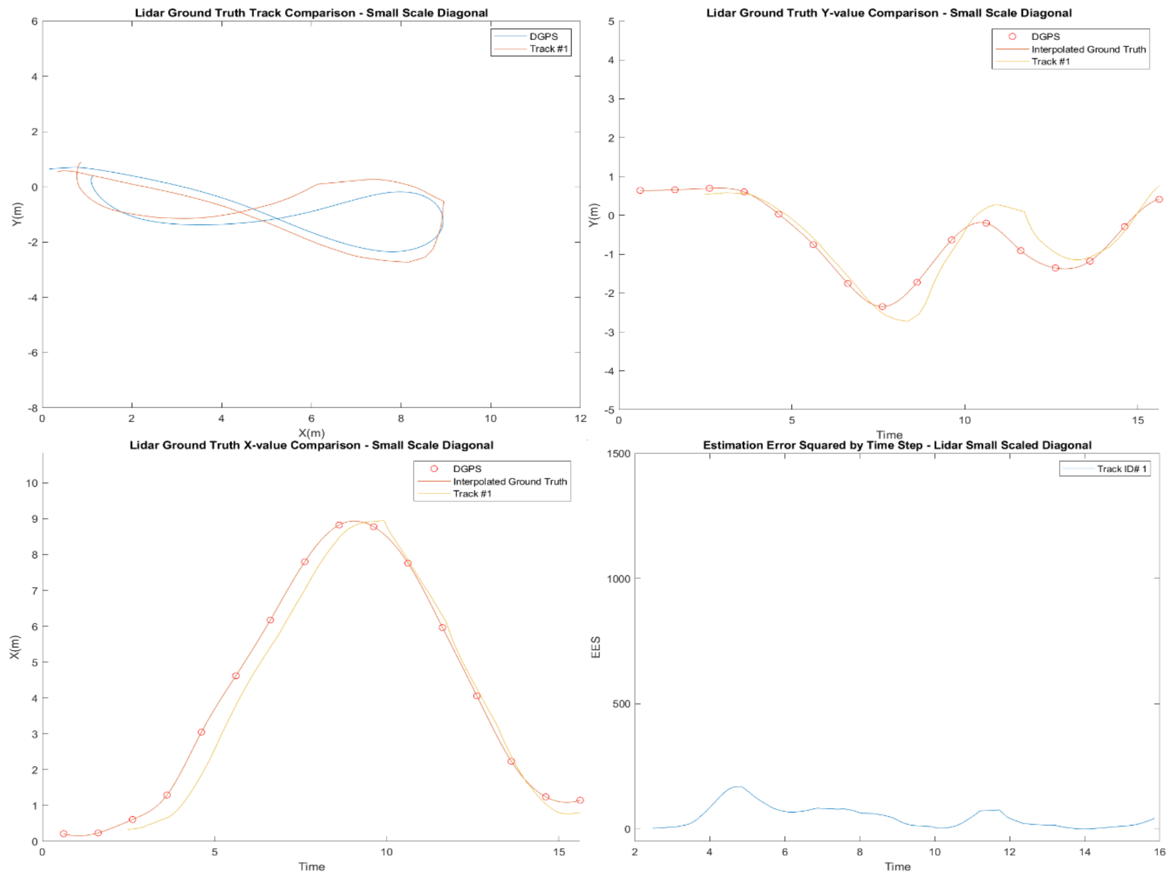

Figure 25: Track position and ground truth overlay, Y-value and ground truth overlay, X-value and ground truth overlay, and EES metric vs time. "Diagonal" small scale trial, LiDAR tracks.

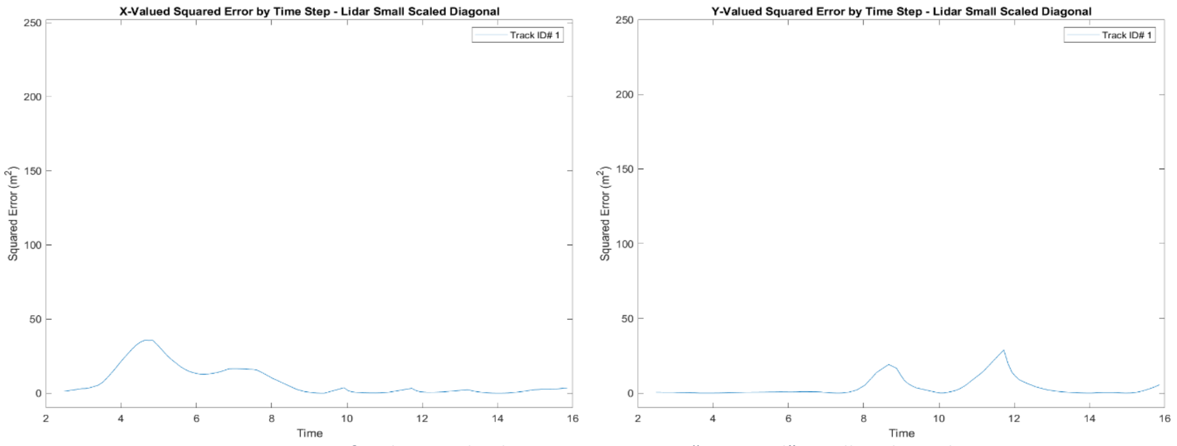

Figure 26: SE curves for the x and y dimensions vs time. "Diagonal" small scale trial, LiDAR.

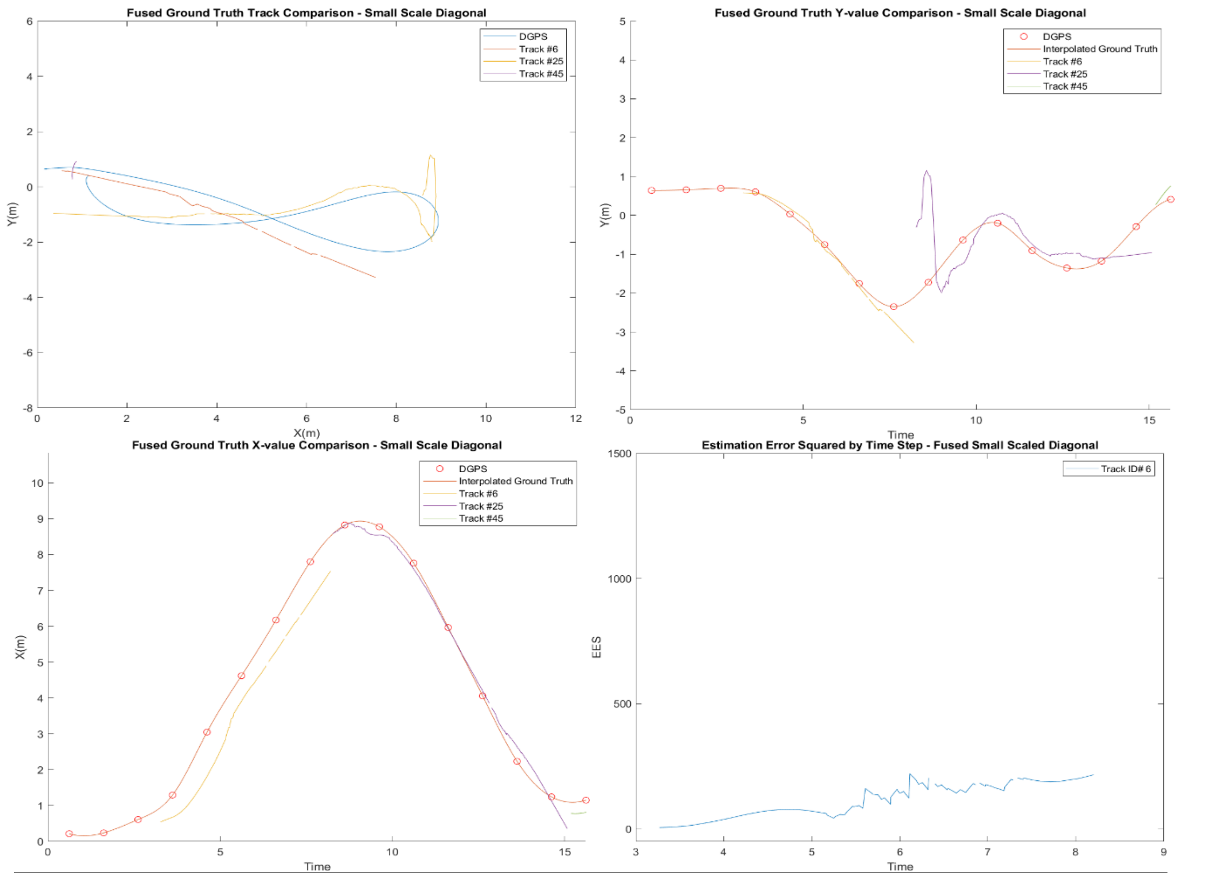

Figure 27: Track position and ground truth overlay, Y-value and ground truth overlay, X-value and ground truth overlay, and EES metric vs time. "Diagonal" small scale trial, fused tracks.

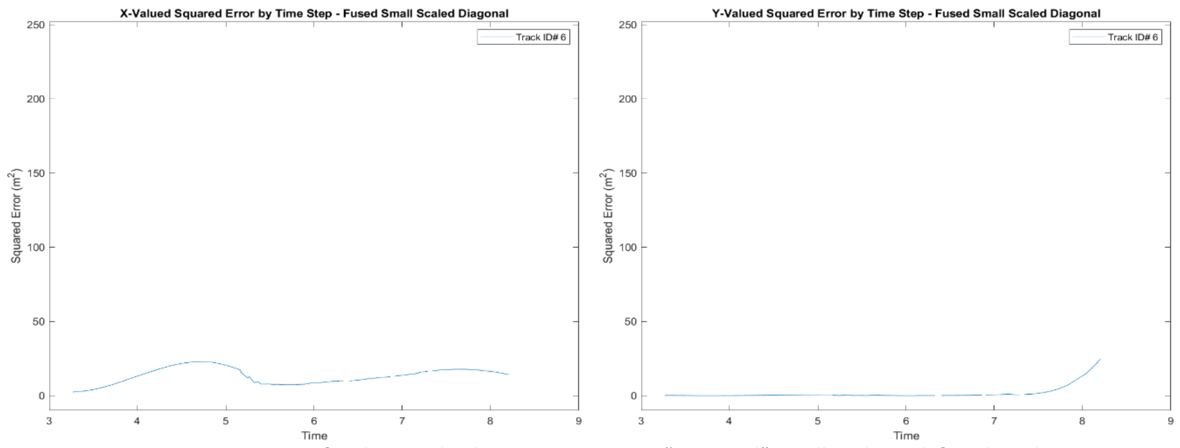

Figure 28: SE curves for the x and y dimensions vs time. "Diagonal" small scale trial, fused tracks.

APPENDIX C

SMALL SCALE "S-TURN" TRIAL RUN GRAPHS

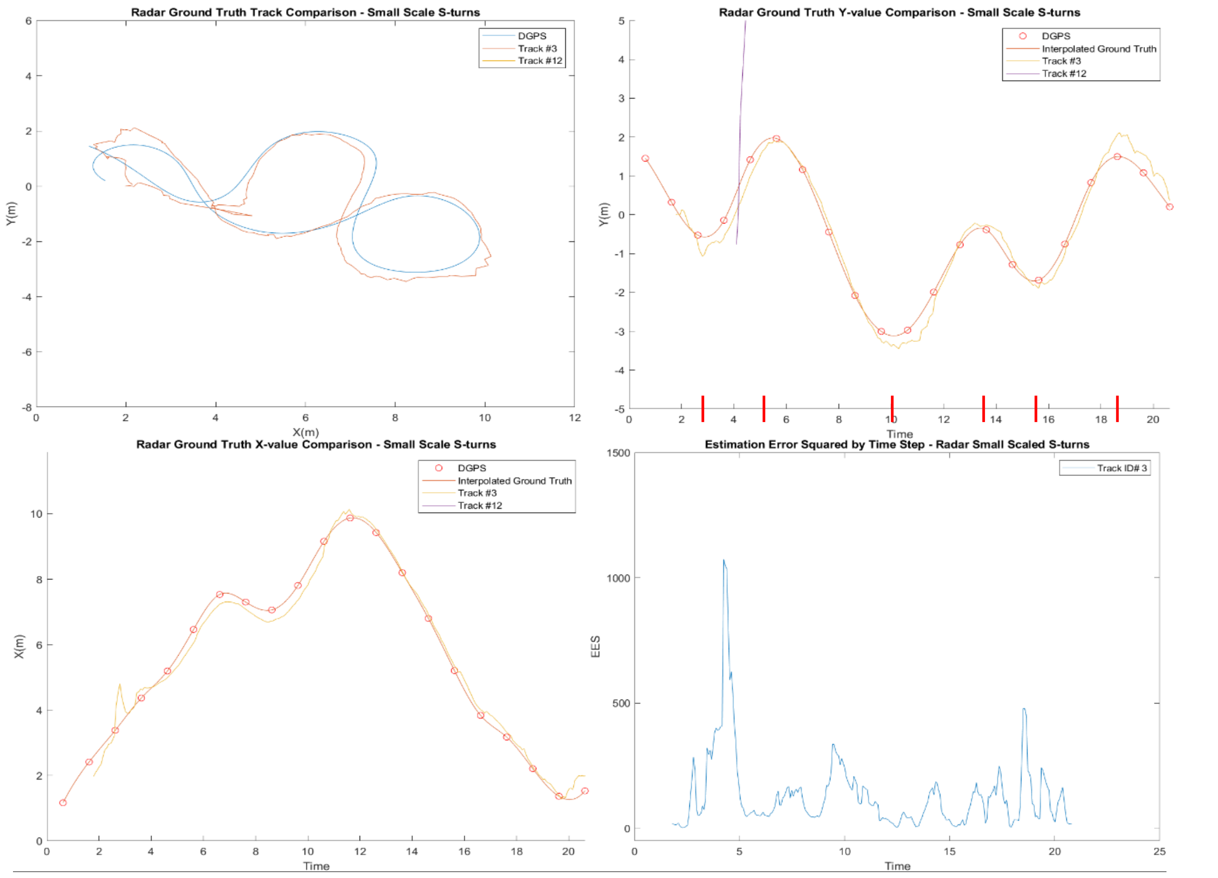

Figure 29: Track position and ground truth overlay, Y-value and ground truth overlay, X-value and ground truth overlay, and EES metric vs time. "S-turn" small scale trial, radar tracks.

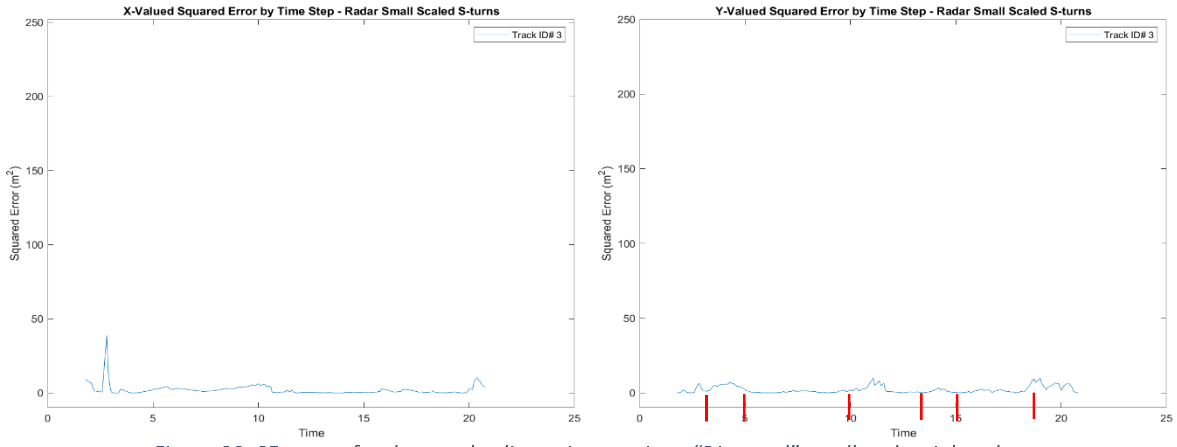

Figure 30: SE curves for the x and y dimensions vs time. "Diagonal" small scale trial, radar.

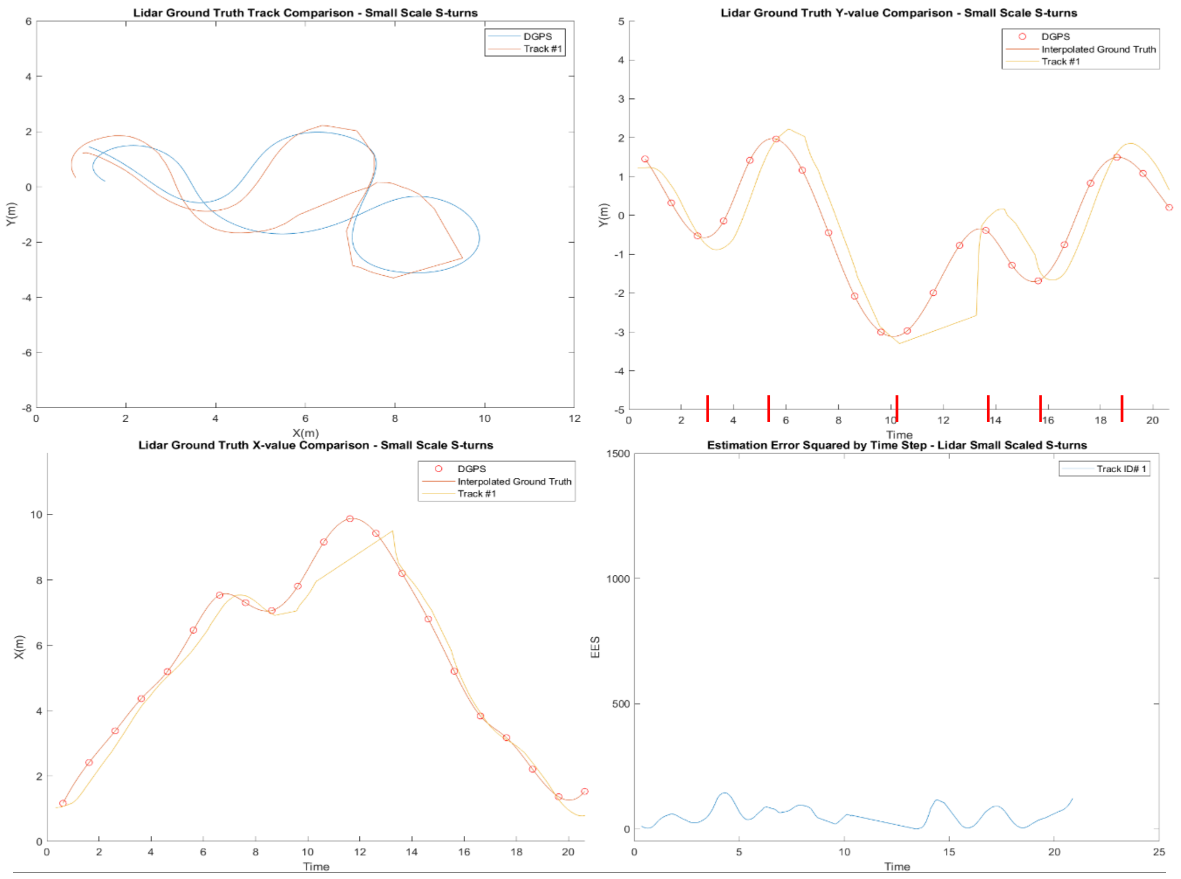

Figure 31: Track position and ground truth overlay, Y-value and ground truth overlay, X-value and ground truth overlay, and EES metric vs time. "S-turn" small scale trial, LiDAR tracks.

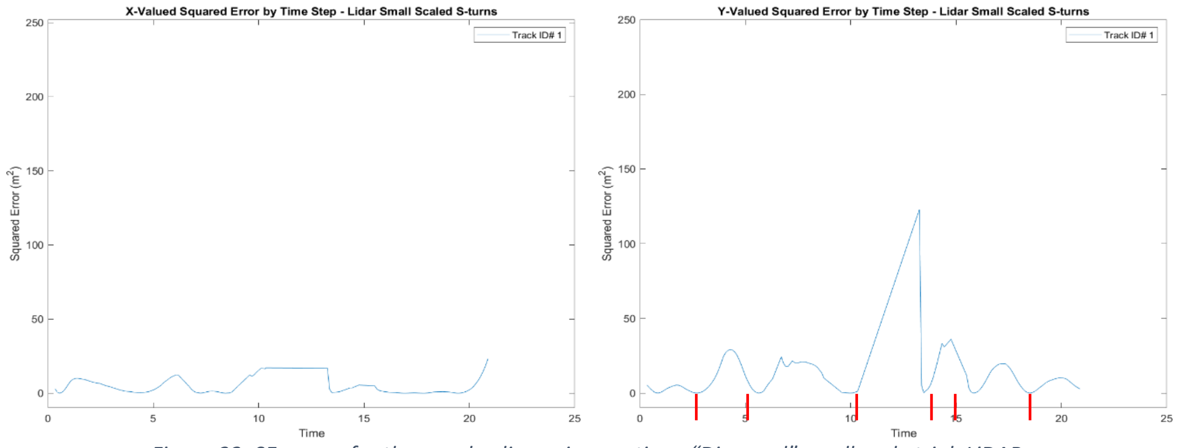

Figure 32: SE curves for the x and y dimensions vs time. "Diagonal" small scale trial, LiDAR.

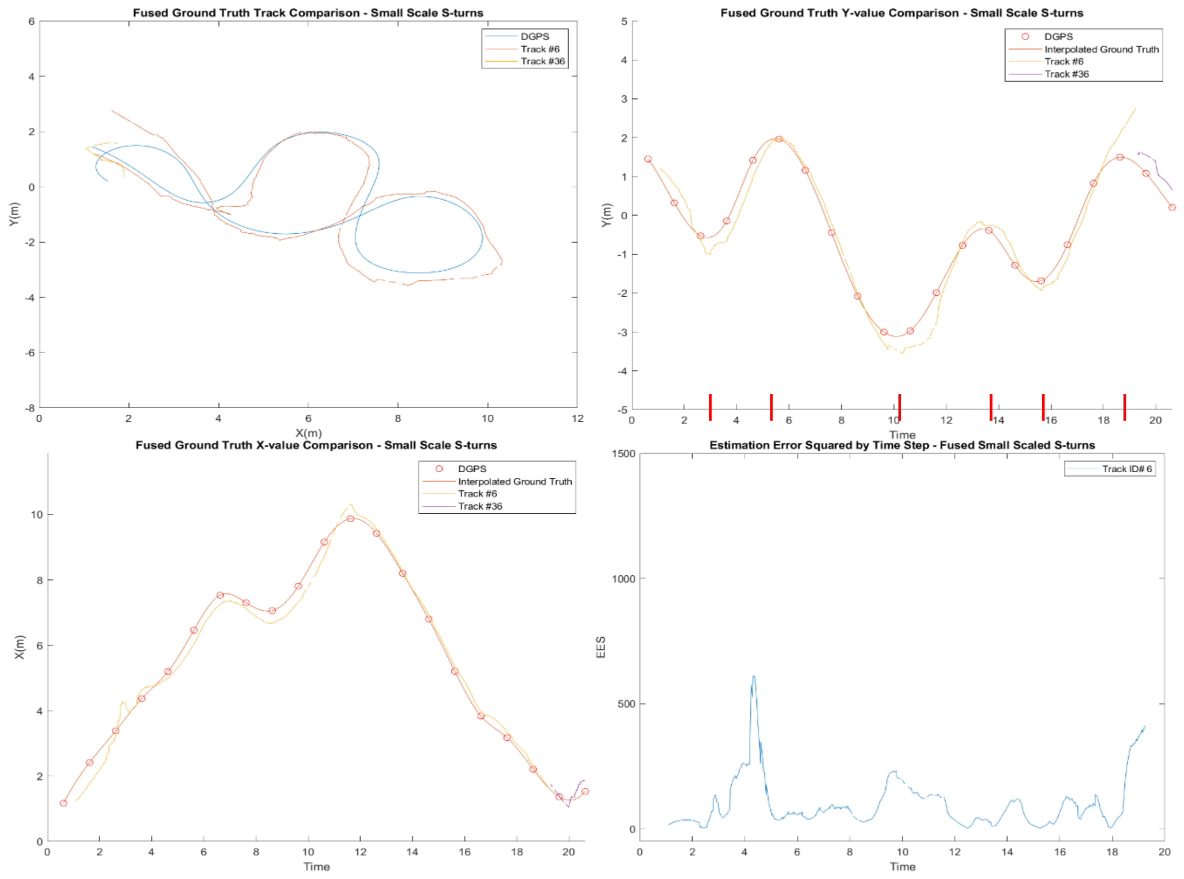

Figure 33: Track position and ground truth overlay, Y-value and ground truth overlay, X-value and ground truth overlay, and EES metric vs time. "S-turn" small scale trial, fused tracks.

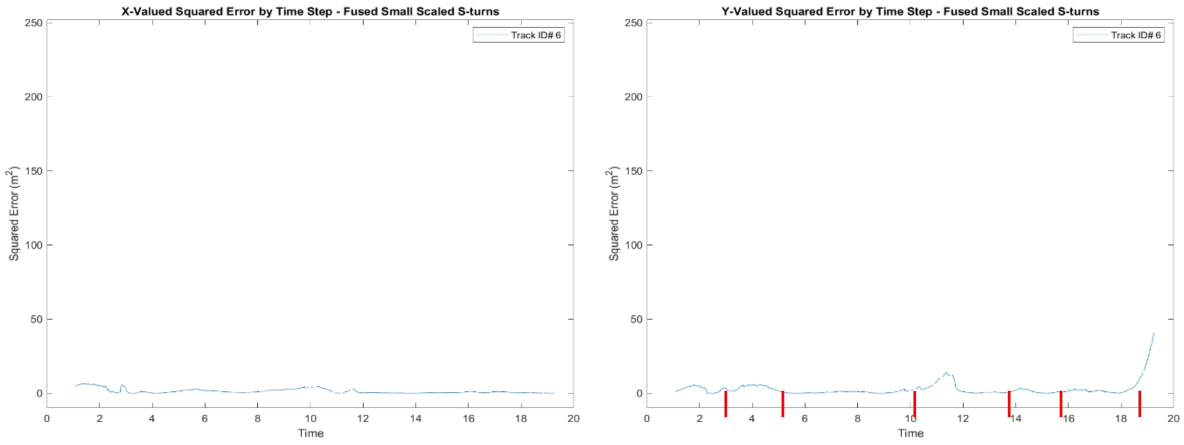

Figure 34: SE curves for the x and y dimensions vs time. "Diagonal" small scale trial, fused tracks.

APPENDIX D

CONTINENTAL AUTOMOTIVE ARS 400 SERIES RADAR DATA SHEET

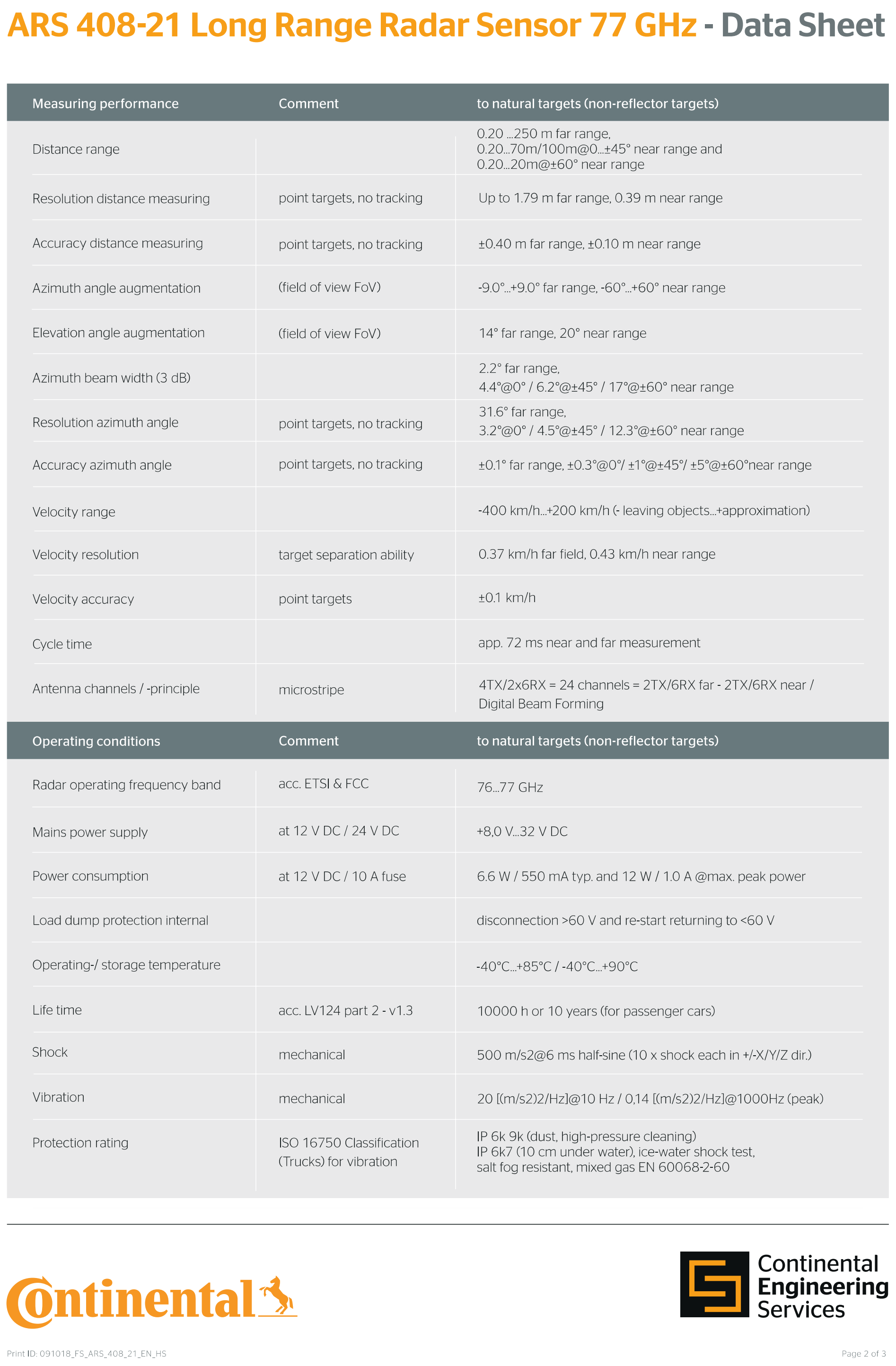

ARS 408-21 Long Range Radar Sensor 77 GHz - Data Sheet

Measuring performance	Comment	to natural targets (non-reflector targets)
Distance range		0.20 …250 m far range, 0.20…70m/100m@0…±45° near range and 0.20…20m@±60° near range
Resolution distance measuring	point targets, no tracking	Up to 1.79 m far range, 0.39 m near range
Accuracy distance measuring	point targets, no tracking	±0.40 m far range, ±0.10 m near range
Azimuth angle augmentation	(field of view FoV)	-9.0°…+9.0° far range, -60°…+60° near range
Elevation angle augmentation	(field of view FoV)	14° far range, 20° near range
Azimuth beam width (3 dB)		2.2° far range, 4.4°@0° / 6.2°@±45° / 17°@±60° near range
Resolution azimuth angle	point targets, no tracking	31.6° far range, 3.2°@0° / 4.5°@±45° / 12.3°@±60° near range
Accuracy azimuth angle	point targets, no tracking	±0.1° far range, ±0.3°@0°/ ±1°@±45°/ ±5°@±60°near range
Velocity range		-400 km/h…+200 km/h (- leaving objects…+approximation)
Velocity resolution	target separation ability	0.37 km/h far field, 0.43 km/h near range
Velocity accuracy	point targets	±0.1 km/h
Cycle time		app. 72 ms near and far measurement
Antenna channels / -principle	microstripe	4TX/2x6RX = 24 channels = 2TX/6RX far - 2TX/6RX near / Digital Beam Forming
Operating conditions	**Comment**	**to natural targets (non-reflector targets)**
Radar operating frequency band	acc. ETSI & FCC	76…77 GHz
Mains power supply	at 12 V DC / 24 V DC	+8,0 V…32 V DC
Power consumption	at 12 V DC / 10 A fuse	6.6 W / 550 mA typ. and 12 W / 1.0 A @max. peak power
Load dump protection internal		disconnection >60 V and re-start returning to <60 V
Operating-/ storage temperature		-40°C…+85°C / -40°C…+90°C
Life time	acc. LV124 part 2 - v1.3	10000 h or 10 years (for passenger cars)
Shock	mechanical	500 m/s2@6 ms half-sine (10 x shock each in +/-X/Y/Z dir.)
Vibration	mechanical	20 [(m/s2)2/Hz]@10 Hz / 0,14 [(m/s2)2/Hz]@1000Hz (peak)
Protection rating	ISO 16750 Classification (Trucks) for vibration	IP 6k 9k (dust, high-pressure cleaning) IP 6k7 (10 cm under water), ice-water shock test, salt fog resistant, mixed gas EN 60068-2-60

Continental

Continental Engineering Services

Print ID: 091018_FS_ARS_408_21_EN_HS

Page 2 of 3

ARS 408-21 Long Range Radar Sensor 77 GHz - Data Sheet

Connections	Comment	to natural targets (non-reflector targets)
Monitoring function		self monitoring (fail-safe designed)
Interface	up to 8 ID	1 x CAN - high-speed 500 kbit/s

Housing	Comment	to natural targets (non-reflector targets)
Dimensions / weight	L * W * H (mm) / (mass)	138 * 91 * 31 / app. 320 g
Material	housing front / backcover	PBT GF 30 black (BASF-Ultradur B4300G6 LS sw 15073) / AC-47100 (AlSi12Cu1(FE)) die cast aluminium or EN AW 5754 (3.535) AlMg3 pressed-formed aluminium

Miscellaneous

Measuring principle (Doppler's principle) in one measuring cycle due basis of FMCW with very fast ramps independent measurement of distance and velocity

Version **ARS 408-21**
sensor for the industry
CAN protocol for free communication

The version -21 allows to set maximum 8 ID's and maximum 8 collision avoidance regions and to change the sensitivity between low and high sensitivity by the user continuously

Interfaces: The device is fitted with one CAN bus interface. Further interfaces as converter, software adaption are possible on demand and in case of assumption of costs.

A special software version supports a measurement range up to 1200m (For objects with high RCS and a free field of view)

APPENDIX E

VELODYNE PUCK LIDAR DATA SHEET

VLP-16

Automotive Robotics Mapping UAV Security Industrial

Velodyne LiDAR PUCK™

Velodyne's Puck (VLP-16) is the smallest, cost-optimized product in Velodyne's 3D LiDAR product range. Developed with mass production in mind, the Puck is far more cost-effective than comparable sensors, and it retains the key features of Velodyne's breakthroughs in LiDAR: Real-time, 360°, 3D distance and calibrated reflectivity measurements.

Real-Time 3D LiDAR

The VLP-16 has a range of 100 m, and the sensor's low power consumption, light weight, compact footprint and dual return capability make it ideal not only for autonomous vehicles but also for robotics, terrestrial 3D mapping and many other applications.

Velodyne's LiDAR Puck supports 16 channels, ~300,000 points/second, 360° horizontal field of view and a 30° vertical field of view, with ±15° up and down. The Puck does not have visible rotating parts, and is highly resilient in challenging environments while operating over a wide temperature range.

DIMENSIONS *(Subject to change)*

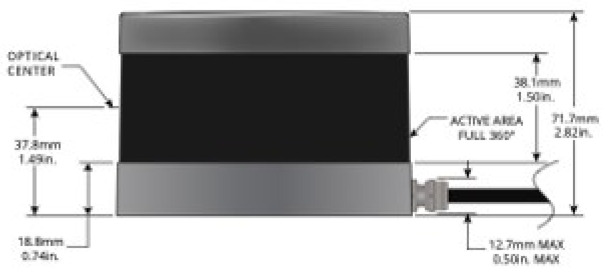

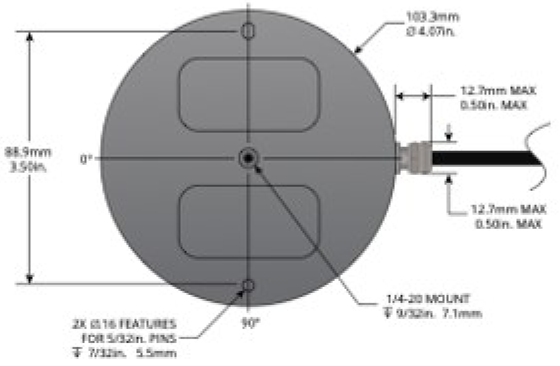

M12 CONNECTOR OPTION

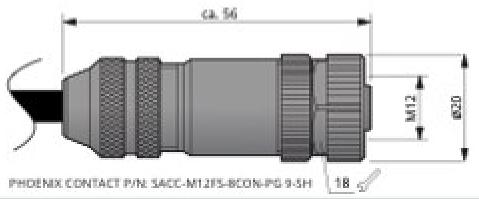

For other connector options contact
Velodyne Sales (sales@velodyne.com)

www.velodynelidar.com

VLP-16

Real-Time 3D LiDAR Sensor

The VLP-16 provides high definition 3-dimensional information about the surrounding environment.

	Specifications:
Sensor:	• 16 Channels • Measurement Range: 100 m • Range Accuracy: Up to ±3 cm (Typical)[1] • Field of View (Vertical): +15.0° to -15.0° (30°) • Angular Resolution (Vertical): 2.0° • Field of View (Horizontal): 360° • Angular Resolution (Horizontal/Azimuth): 0.1° – 0.4° • Rotation Rate: 5 Hz – 20 Hz • Integrated Web Server for Easy Monitoring and Configuration
Laser:	• Laser Product Classification: Class 1 Eye-safe per IEC 60825-1:2007 & 2014 • Wavelength: 903 nm
Mechanical/ Electrical/ Operational	• Power Consumption: 8 W (Typical)[2] • Operating Voltage: 9 V – 18 V (with Interface Box and Regulated Power Supply) • Weight: ~830 g (without Cabling and Interface Box) • Dimensions: See diagram on previous page • Environmental Protection: IP67 • Operating Temperature: -10°C to +60°C[3] • Storage Temperature: -40°C to +105°C
Output:	• 3D LiDAR Data Points Generated: - Single Return Mode: ~300,000 points per second - Dual Return Mode: ~600,000 points per second • 100 Mbps Ethernet Connection • UDP Packets Contain: - Time of Flight Distance Measurement - Calibrated Reflectivity Measurement - Rotation Angles - Synchronized Time Stamps (μs resolution) • GPS: $GPRMC and $GPGGA NMEA Sentences from GPS Receiver (GPS not included)

63-9229 Rev-H

For more details and ordering information, contact Velodyne Sales (sales@velodyne.com)

1. Typical accuracy refers to ambient wall test performance across most channels and may vary based on factors including but not limited to range, temperature and target reflectivity.
2. Operating power may be affected by factors including but not limited to range, reflectivity and environmental conditions.
3. Operating temperature may be affected by factors including but not limited to air flow and sun load.

CLASS 1 LASER PRODUCT

Velodyne LiDAR, Inc. 345 Digital Drive, Morgan Hill, CA 95037 / lidar@velodyne.com / 408.465.2800 | www.velodynelidar.com